Focusing Energy Underwater Through Optimization of a Spherical Source Array

by

Nicholas A. Stowe

A dissertation submitted in partial fulfillment
of the requirements for the degree of
Doctor of Philosophy
(Naval Architecture and Marine Engineering)
in The University of Michigan
2013

Doctoral Committee:

Professor Nickolas Vlahopoulos, Chair
Professor Steven L. Ceccio
Associate Professor Bogdan Epureanu
Assistant Professor David J. Singer

© Nicholas A. Stowe 2013
All Rights Reserved

To everyone who lingered long enough to listen to my stories, and especially to those who helped bring new ones to life

ACKNOWLEDGEMENTS

When I ventured west to seek my fortune five years ago, I had no idea how formative my years in Ann Arbor would be. Through reflection, it has become abundantly clear that I grew up in Ann Arbor - this is largely due to the individuals whose paths I have crossed and whose fingerprints are now poignant hallmarks on my life story.

First and foremost, I would like to thank my advisor, Dr. Nickolas Vlahopoulos, for his effective management across several years of research. Dr. Vlahopoulos has placed me in challenging positions just within my reach, and in doing so has accelerated my growth and breadth in a way uncommon to typical graduate study. He has given me a very long leash and has demonstrated his faith in my ability across the seasons of my PhD. Such trust and confidence resonates deeply and will be my lasting impression of our years attacking the analytical UNDEX problem together.

I am very grateful to the Office of Naval Research, specifically Maria Medeiros and Dan Tam, for their fiduciary support and oversight of this project through the University Laboratory Initiative. I will remember my spirited collaborations with my NSWC Indian Head colleagues, and I owe a large debt of gratitude to Greg Harris, Marty Marcus, and Ken Kiddy, along with the supporting cast, for bearing with me and illuminating the paths to many solutions.

Time has passed sweetly by as I have enjoyed a multitude of acquaintances in Ann Arbor, both in the NAME Department and outside of it. I will refrain from listing names for fear of omitting one that I shouldn't. You know who you are, and I hope you understand how deeply I treasure the experiences we have shared in this place.

Special thanks to Bill and Greg for the 'peer-review', however.

My family has been stalwart in their support through every hurdle I faced, and the steadfastness of their love regardless of my success or failure has been held close at heart. They also put me in a position to succeed. I would never have been able to learn so much here if I had not learned certain lessons at home. Thanks Mom and Dad (and Alex too!).

This doctoral degree has come at a significant cost; the greatest, perhaps, being the distance that has separated Aimée and I. As a result, she has patiently endured numerous explanations of engineering minutiae over the phone, and has always attempted a thoughtful response. To my love and closest friend, your words and determination have carried me through the many low times when I needed a companion the most. Thank you for your presence, affection, and encouragement throughout the past five years.

TABLE OF CONTENTS

LIST OF FIGURES

Figure

LIST OF TABLES

Table

LIST OF APPENDICES

Appendix

ABSTRACT

Focusing Energy Underwater Through Optimization of a Spherical Source Array

by

Nicholas A. Stowe

Chair: Nickolas Vlahopoulos

The concept of focusing energy from multiple underwater sources is of interest as a potential new approach for defeating underwater threats. An array of spherical shock sources arranged in a two-dimensional pattern has been suggested to achieve this aim. The goal of the present research effort is to identify optimal arrangement and detonation timing schemes for the creation of desired shock waveform characteristics at the target. First, a physics-based reduced order model has been developed for the multiple-source array. The reduced order model captures important shock phenomena including propagation speed, pressure-time histories throughout the fluid domain, and shock wave interaction phenomena. Rarefaction waves appearing in the array flow field have also been incorporated.

The development of a reduced order model was prompted by the constraints of mathematical optimization. Optimization using evolutionary algorithms, which have been chosen for the present effort, requires the evaluation of an equation, function, or model hundreds or thousands of times before converging on an optimal solution. Existing models for underwater shock phenomena are either too crude to capture complex shock interactions or too computationally expensive for optimization analy-

sis. The reduced order model developed herein is capable of modeling complex shock physics while maintaining a relatively inexpensive execution time that enables optimization analysis. An optimization framework has been constructed and is applied to the design of a rectangular grid array using the reduced order model.

CHAPTER I

Introduction

"...for there is nothing either good or bad, but thinking makes it so." -Shakespeare

The well-known Nobel prize is named after Swedish chemist, engineer, and inventor Alfred Nobel. The eponymous awards, at the beginning, were funded by the great fortune amassed through his most famous invention: dynamite. A safe and stable alternative to other explosive materials available at the time, dynamite was widely used in the mining and construction industries; the breadth of its use is underscored by the tremendous profits it generated. Construction of roads, tunnels, and other critical infrastructure was accelerated by this technology in an age when steam locomotives were propelling mankind further, faster than it had ever travelled before.

While advancing technologies beneficial to humanity, dynamite also found its place in more sinister applications. Over time, dynamite was introduced as an energetic material in devices of war. Explosive devices of all kinds, descendants of these early mechanisms, are currently threatening shipping and human safety all over the world. The duality of progress and destruction encapsulated in early applications of dynamite is reincarnated presently with the concept of a multiple-source explosive array.

This dissertation addresses the design of the multiple-source explosive array and the physics of the complex fluid flow it creates. The concept is shown in Figure 1.1 for

clarity. The dark region represents the target range. Significant nonlinear interaction of waves produced by the array make it difficult to discern the ramifications of various design decisions. Mathematical optimization is a critical tool in the decision making process, therefore, as esoteric tradeoffs can be analyzed in an intelligent and strategic manner using these methods. This dissertation presents a framework specifically tailored to analyze the multiple-source explosive array design problem.

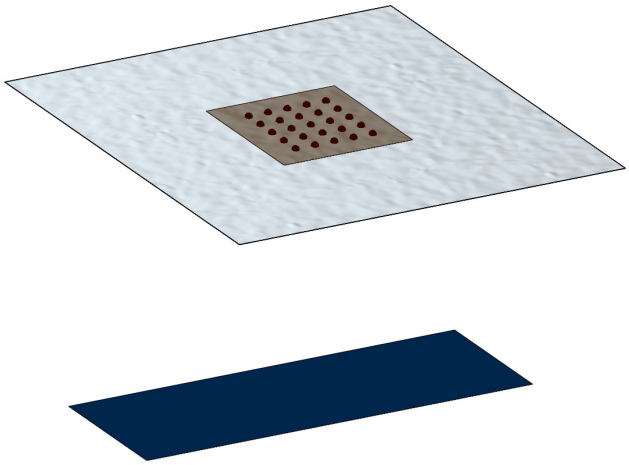

Figure 1.1: Multiple-Source Explosive Array Concept

A model for the effects and behavior of the array lies at the heart of the optimization framework. Existing methods for modeling underwater explosions fall short due to lack of sophistication or untenable computational expense. A physics-based, reduced-order model has been developed as the core element of the research presented herein in an effort to satisfy the requirements of reasonable accuracy and computational speed that are central to effective optimization analysis. This chapter introduces relevant phenomena associated with underwater explosions, the objective and scope of the presented research, and a summary of prior developments in this field which both inform the present work and illustrate the necessity of a new mathematical representation for underwater shock propagation.

1.1 Anatomy of an Underwater Explosion

1.1.1 The Shock Wave

When an explosive charge is detonated underwater, the energetic material is rapidly converted into gas of extremely high temperature and pressure. An expanding pressure wave is then propagated beyond the initial bounds of the charge as the overpressure is relieved through the outward-propagating wave. Water is compressed, and the pressure rise across the wave is considered to be discontinuous for all practical purposes (*Cole*, 1948). This phenomena is called a shock wave. Shock waves are characterized by the following notable traits:

- Shock waves propagate much faster than acoustic waves, which travel at the ambient sound speed in the fluid
- A shock wave compresses the fluid it travels through; this is the mechanism by which a discontinuous jump in fluid state is achieved
- Shock waves decay both spacially and temporally as energy is transmitted into the surrounding medium. In the case of shock waves produced by spherical explosions, the decay profile is roughly exponential in both time and space

1.1.2 The Explosive Gas Bubble

In typical underwater explosions, shock wave effects can be seen at the surface within milliseconds of detonation. Meanwhile, explosive gases are contained in a bubble that rises to the surface at a relatively slow rate, typically on the order of seconds. The explosive gas bubble expands and collapses cyclically along the way, sending subsequent pressure waves into the fluid before the bubble eventually is vented at the surface. Shock waves generated by the pulsating bubble have a magnitude that is typically 15-30% of the peak shock pressure (*Murata et al.*, 1999).

Bubble effects are highly important when targeting structures at the surface. The collapse-expansion oscillation period can be tuned so as to excite natural frequencies in these structures (*Vernon*, 1986). The threats of interest for the multiple-source array are deeply submerged, however. Added mass and damping experienced by submerged structures limit the vibrations induced by bubble collapse shocks. With this in mind, bubble oscillations have been ignored for the following reasons. Peak pressures exhibited by bubble collapse shock waves are much lower than the peak pressure typical of an explosive shock wave. Bubble collapse shock waves also occur on a much larger time scale than explosive shock waves. By the time the shock wave produced by a bubble collapse reaches the target, the explosive shock effects will have damaged the structure sufficiently. Therefore, the magnitude and incidence rate of bubble collapse shock waves renders them negligible for the multiple-source explosive array.

1.2 Problem Statement, Objectives, and Scope

There is interest in using an array of small energy sources to direct and focus pressure waves toward a remote location underwater. The aim is to induce a desired structural response in a threat located at the target. The structural responses of interest include exciting a specific natural frequency of the structure, or producing a total loading sufficient to cause damage. The application envelope is broad, as these structures may include the seabed itself. For example, an array of shaped charges has recently been used to bore a hole in the bottom of Lake Mead for the "Third Straw" construction project (*Folchi and Wallin*, 2012).

Given the loading parameters necessary to induce the structural response of interest, physics-based, reduced-order models and optimization techniques can be used to quantify the size and number of discrete energy sources needed to meet the design objectives. Ideally, the energy source should be reusable or easily reconfigured for

rapid turnaround. Methods that meet this criterion include air guns, nastic arrays, and electric spark discharge. For purposes of this analysis, the energy source consists of multiple small explosive charges, because shock waves produced by underwater explosions have been studied and are representative of the loading magnitudes necessary to satisfy the objective. The method described in this thesis can be extended to any energy source emitting spherical shock waves that can be controlled in a repeatable manner.

The overarching goal of the present work is to develop a reduced-order model for shock waves generated by a two-dimensional array of spherical explosives, and to optimize the array geometry and detonation timing scheme to achieve a desired pressure waveform at some target in the fluid below. The shock wave produced by a spherical explosive propagates with a certain speed, has a specific amplitude, and decays exponentially in both space and time. When multiple charges detonate in the vicinity of one another, shock waves interact in important ways that significantly influence the pulse at the focus point. Numerical methods exist to predict the behavior of the multiple-source array, including these interactions. However, existing numerical methods, such as computational fluid dynamics (CFD), can be computationally expensive (computations for multiple-source explosive arrays can take weeks). In the extreme case of large arrays and remote targets, the computational grid size necessary to resolve the shock waves is impossible to implement, even on high performance computing clusters.

The present work seeks to model important shock physics analytically; that is, in the absence of numerical integration of conservation equations. This objective is motivated by the highly iterative nature of optimization algorithms. Optimization requires several evaluations of an equation, function, or model as the algorithm converges to an optimal solution. Any method used to model the multiple-source array must therefore combine sufficient fidelity with rapid computational speed. Although

they are highly accurate, fluid solvers that rely on numerical integration of conservation equations are computationally expensive and thus ill-suited for optimization work.

An appropriate optimization approach for the design of the explosive array must be devised. The design problem is complicated by the presence of discrete and continuous design variables (such as the number of sources and the detonation time of each source) that influence nonlinear shock behavior. Gradient-based optimization algorithms are generally unable to accommodate discrete variables, such as the number of charges in the multiple-source array. The array design space is also highly multimodal, as a variety of detonation timing schemes have the potential to create similar results at the target point. Multimodal problems are a notorious weakness of hill-climbing methods. A genetic algorithm has been implemented for the analysis of the multiple-source array design problem, because it can incorporate discrete variables. Furthermore, as a stochastic search method, it counteracts multimodal difficulties.

1.3 Existing Shock Modeling Techniques

1.3.1 Analytical Methods

The underwater shock pressure-time profile produced by spherical explosive charges, referred to here as the shock waveform, has been studied since the early 20th century (*Cole*, 1948). The most commonly used model, the so-called 'Similitude Equations', were documented in 1946 (*Coles et al.*, 1946). Coles noted that points representing peak pressure traced a straight line when plotted on a log-log plot versus charge weight W cubed over standoff distance R $\left(\frac{W^{1/3}}{R}\right)$. A series of tests were undertaken to determine the slope of this line. Subsequently, curve fitting coefficients were calculated for pressure, momentum, energy, and decay time constant versus the scaled range.

Due to high fluid pressures and velocities present in shock waves and given the short duration of the shock pulse, experimental measurement of shock properties has always been difficult. As experimental setup and measurement technology advanced, the similitude coefficients were updated by Arons (*Arons*, 1953), Slifko and Farley (*Slifko and Farley*, 1959), and several others through Swisdak (*Swisdak*, 1978). Though they are fast and easy to use, the similitude equations do not provide a comprehensive solution for underwater shock modeling. First, the similitude equations and their associated coefficients do not predict shock propagation speed. Locating the position of each shock in space and time is critical for accurate modeling of the interactions of multiple shock waves. Second, $4.76W^{\frac{1}{3}}$ meters (with charge weight measured in kilograms) has been derived as the outer limit of the similitude equation applicability range (*Richardson et al.*, 1995). Lastly, the similitude equations provide no means for capturing complex shock interaction phenomena, instead offering simple superposition of pressure waves as a multiple shock model.

Theoretical and experimental investigation of underwater shock behavior occurred simultaneously. Early on, Lamb constructed a solution to the spherical shock problem that assumed an incompressible fluid (*Lamb*, 1923). The shock waves produced by underwater explosions do not behave acoustically in the near-field; indeed the very presence of a shock wave indicates fluid compressibility. Due to this fundamental attribute of shock waves, Lamb's approach exhibited limited accuracy. Penney later derived a method involving numerical integration of the Riemann equations and included a simple equation of state (*Penney*, 1940). The Riemann equation approach is limited to cases where dissipation can be neglected. Kirkwood and Bethe proposed a more analytical solution to the spherical shock problem that employs the second law of thermodynamics and the assumption that the change in enthalpy behind the shock front is trivial. The Kirkwood-Bethe approach continues to be used to define the shock waveform produced by an underwater explosion (*Hunter and Geers*, 2003).

Rogers noted that the Kirkwood-Bethe method, though elegant, is somewhat difficult to use because pressure and particle velocity are not used as the dependent variables and the solution is an implicit function of range (*Rogers*, 1977). As an alternative, he developed a weak shock solution for spherical shock waves produced by underwater explosions. In acoustics, a shock can be characterized as weak when the particle velocity incited by the shock wave is much less than the sound speed behind the shock wave ($u << c$). Underwater shocks generated by small sources can be described as weak, given this definition. Rogers' work has been modified and included in the analytical model developed in this dissertation.

The solutions described above concern the calculation of pressure, impulse (the integral of pressure over time), energy, and particle velocity in a fluid that has been excited by a shock wave. Shock propagation speed has been neglected in these models, yet it is a critical component of multiple-source explosive array behavior. Two propagation speed methods have been investigated toward this end. The first finds its foundation in the *energy hypothesis*, developed by mathematician T. Y. Thomas (*Thomas*, 1957). Its derivation centers on the examination of a spherical control volume surrounding the shock wave. The result is an algebraic equation that relates the change in energy across the spherical shock front to the radius of the shock sphere and the thermal energy contained in that charge. Singh combined Thomas' equation with the Rankine-Hugoniot jump equations and the Tait equation of state to determine the rate of advance of the shock front (*Singh and Bola*, 1974). In the present work, this method has been derived with the Tillotson equation of state in place of the Tait equation with a successful outcome. A second method for the prediction of shock propagation speed has been developed using weak shock principles and has been applied in the reduced-order model presented here.

1.3.2 Numerical Methods

The analytical model developed herein is evaluated using a sophisticated numerical solver that has been designed to model underwater explosions (*Wardlaw et al.*, 2010). The CFD code solves the inviscid Euler equations using a second-order Godunov scheme, an approach proven to be highly accurate for modeling shock propagation (*Landsberg et al.*, 2003). The CFD solver is capable of modeling multiple explosions and the interactions of multiple shock waves, while capturing pressure, density, particle velocity, and internal energy in the fluid at user-specified points for the time duration of the simulation. All CFD results that have been plotted for comparison with the analytical model have been calculated for the explosion of spherical TNT charges in an infinite medium without gravity. The ambient pressure and density of the fluid is set to conditions on the surface of a body of fresh water ($100,000\ Pa$ and $1000\ kg/m^3$ respectively).

The motivation to develop the reduced-order model is found in the nature of optimization analysis. Most optimization algorithms are highly iterative. The model or equation being optimized is evaluated hundreds or thousands of times before a converged solution is found. Although the CFD solver described above has been widely validated and offers a high degree of accuracy, it is computationally expensive. The present model has been assembled using analytical, physics-based methods in an attempt to capture the problem as accurately as possible while restricting execution times to be on the order of minutes.

The reader will note that the bulk of the prior research used as a starting point for the present model was published before 1980. Analytical shock hydrodynamics, as a field of study, was somewhat abandoned as the underwater shock community moved on to numerical methods when computational power increased in the 1980's and onward. The necessity for a computationally inexpensive multiple-charge model has not appeared in the literature until now. As a result, the study of the interac-

tion of spherical shock waves is relatively unexplored field, with the nuances of this phenomena examined experimentally only recently (*Kandula and Freeman*, 2008).

1.4 Research Contributions

In order to summarize this chapter and to succinctly detail the technical contributions brought forward as part of this research, a list describing the novel developments included in this dissertation is compiled below.

1. Improve upon current shock decay profile modeling methods, including the magnitude of the shock tail

2. Reevaluate shock propagation speed models, suggesting a new nonlinearity parameter for water and account for shock interactions when determining shock speed

3. Study and represent rarefaction waves produced by the multiple-source explosive array, including an identification of key drivers of cumulative interaction effects

4. Present a comprehensive physics based reduced-order model for the explosive array, incorporating shock interaction and coalescence

5. Develop an optimization framework to assist in the design of the explosive array, utilizing the analytical model that has been created

CHAPTER II

Spherical Shock Waves

The pressure pulse generated by single spherical charges of TNT, which comprise the building blocks of the multiple-source explosive array, must be understood in order to model the behavior of the comprehensive system. Shock waves emitted by these charges are characterized by propagation speed, peak shock amplitude, and temporal and spatial decay. As the array design is optimized, propagation speed of each wave informs detonation timing scheme selection. In order to quantify the minimum number of sources necessary to achieve the objective, the pressure contribution from a single source must be calculated. Furthermore, as the shocks produced by individual explosives do not travel to the target in a vacuum, single-wave behavior must be sufficiently characterized so that wave interaction effects can be calculated.

This chapter will explore existing methods for modeling shock waves produced by spherical explosive sources, including additions and modifications to these methods that have been developed as part of this research effort. Theoretical developments presented here have been integrated into the physics-based, reduced-order model for the array that is used for the eventual design optimization analysis. To begin, two separate methods for predicting the propagation speed of a single shock wave will be introduced, along with the effects and nuances of the equations of state for water that are used in propagation speed predictions. CFD results will be used to validate both

approaches. A technique for characterizing the shape and magnitude of the pressure and particle velocity waves created by spherical explosions will also be discussed, including a critical pitfall of the existing method regarding modeling of the shock tail. A new modification will be implemented, and pressure, impulse, and particle velocities using the adapted approach will be compared with CFD results for these quantities.

2.1 Shock Propagation Speed

A central component of the multiple-source explosive array is the independent detonation of each shock source. In the optimal case, explosions are triggered across the array in a sequence that best achieves the desired pulse magnitude and duration at the target point. The propagation speed of each shock en route to the target must be understood before ideal detonation timing schemes can be identified. Two methods for predicting shock speed are explored below.

2.1.1 The Thomas Energy Hypothesis

Shocks produced by spherical explosive charges initially travel at speeds much higher than the speed of sound in the fluid. Each shock wave gradually decelerates as the radius from the source, or standoff, increases. Specific energy decreases as the radius of the shock sphere increases. Peak velocity and deceleration are functions of initial shock properties at the source and the properties of the water into which the shock propagates. Fluid properties are modeled by an 'equation of state'. An equation of state is so called because relationships between selected state variables, such as pressure, density, and internal energy are quantified in order to define fluid properties and behavior under various conditions. The Tillotson equation of state for water is implemented in the numerical solver used to validate the reduced-order

model. The Tillotson equation is formulated below:

$$p_2 = p_1 + \omega\rho_2 \left(e_2 - e_1\right) + A\left(\frac{\rho_2}{\rho_1} - 1\right) + B\left(\frac{\rho_2}{\rho_1} - 1\right)^2 + C\left(\frac{\rho_2}{\rho_1} - 1\right)^3 \tag{2.1}$$

with $\omega = 0.28\frac{kg^2}{m \cdot s^2}$, $A = 2.2 \times 10^9$ Pa, $B = 9.54 \times 10^9$ Pa, and $C = 1.457 \times 10^{10}$ Pa. The variable p represents pressure, ρ represents density, and e represents internal energy. When used in the calculation of shock propagation speed, state 1 refers to the local fluid state immediately before the shock arrives, while state 2 refers to the fluid state at the instant after the shock peak passes.

The Tait equation of state for water is ubiquitous in underwater shock literature due to its simple algebraic form, and was originally used in the propagation speed method described in this section. The Tait equation is given by (*Singh and Bola*, 1974):

$$p = A\left[\left(\frac{\rho}{\rho_1}\right)^N - \frac{B}{A}\right] \tag{2.2}$$

where ρ_1 is the density at a pressure of $1{\times}10^5$ Pa. Singh provides values for the coefficients of the Tait equation of state, giving $A = 2.941{\times}10^7$ Pa, $B = 2.94{\times}10^7$ Pa, and $N = 7.25$. Equations of state are useful for modeling both shock waves and simple waves when combined with conservation equations. Each equation of state defines a Hugoniot curve (or surface, depending on whether two or three state variables are related) which illustrates the relationship between state variables. Results from early efforts to quantify these relationships are shown in Figure 2.1, with pressure on the ordinate and specific volume ($1/\rho$) on the abscissa.

The Rankine-Hugoniot equations describe the conservation of mass, momentum, and energy across a discontinuous jump in an inviscid fluid. The jump conditions, as they are also known, can be derived using the one-dimensional Euler equations. The Euler equations for conservation of mass, momentum, and energy are, in respec-

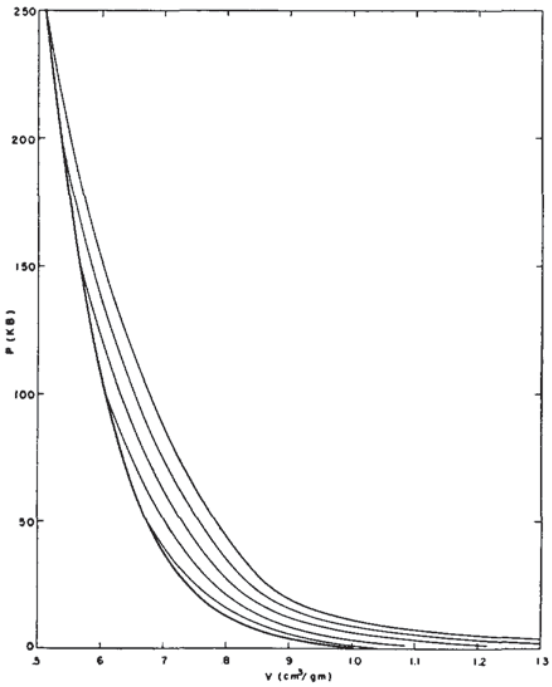

FIG. 2. Pressure-volume relations for the Hugoniot and five adiabats.

Figure 2.1: Early Hugoniot Experimental Results (*Rice and Walsh*, 1956)

tive order:

$$\frac{\partial \rho}{\partial t} = -\frac{\partial}{\partial x}(\rho u), \tag{2.3a}$$

$$\frac{\partial \rho u}{\partial t} = -\frac{\partial}{\partial x}\left(\rho u^2 + p\right), \tag{2.3b}$$

$$\frac{\partial \rho E}{\partial t} = -\frac{\partial}{\partial x}\left[\rho u\left(e + \frac{1}{2}u^2 + p/\rho\right)\right] \tag{2.3c}$$

where E is total energy and u is particle velocity. This system of equations is hyperbolic, and when integrated across a discontinuity using the hyperbolic conservation law, the following equations result:

$$U\left(\rho_2 - \rho_1\right) = \rho_2 u_2 - \rho_1 u_1, \tag{2.4a}$$

$$U\left(\rho_2 u_2 - \rho_1 u_1\right) = \rho_2 u_2^2 + p_2 - \left(\rho_1 u_1^2 + p_1\right), \tag{2.4b}$$

$$U(\rho_2 E_2 - \rho_1 E_1) = \rho_2 u_2 (E_2 + p_2/\rho_2) - \rho_1 u_1 (E_1 + p_1/\rho_1) \tag{2.4c}$$

where U is the rate of advance of the discontinuity, otherwise know as shock front propagation speed. This set of equations are known as the Rankine-Hugoniot jump conditions. The initial state, state 1, is assumed to be still water at 100 kPa with density 1000 kg/m^3 in the single shock propagation speed analysis below. Given a known initial state, the Rankine-Hugoniot jump conditions contain five unknown variables. Two more equations, therefore, must be identified to solve the system for shock front propagation velocity U. An equation of state provides a fourth equation. The Thomas Energy Hypothesis is used to close the system (*Thomas*, 1957).

Thomas proposed that the change in energy across a discontinuity is proportional to the total energy Q that is released in the explosion and inversely related to the radius of the shock sphere R. Given these relations, Thomas described the change in energy across a spherical shock wave using the following equation:

$$E_2 - E_1 = \frac{3\alpha Q}{4\pi R^3 (\rho_2 - \rho_1)} \tag{2.5}$$

where α is a constant describing the explosive material and Q is the thermal energy contained in the solid explosive sphere prior to detonation. The constant α describes properties of the explosive detonation wave. Singh set $\alpha = 1.7465$ for TNT in the initial application of the Thomas Energy Hypothesis to the shock propagation speed problem for the shock wave created by an underwater explosion (*Singh and Bola*, 1974).

The combination of the Rankine-Hugoniot jump conditions with the Thomas En-

ergy Hypothesis was adapted for underwater explosions by Singh and has been followed to this point. In his derivation, Singh employed the Tait equation of state for water. The Tillotson equation of state has been found to be more accurate than the Tait equation for underwater explosion analysis, however, and is implemented in the numerical tool used to validate the reduced-order model. Singh's approach has been derived anew using this Tillotson equation of state. The resulting system of equations can be condensed to the single equation below:

$$\begin{aligned} &\frac{-3\alpha Q}{4\pi R^3 \rho_2} + p_1(v_1 - v_2) \\ &+\omega\rho_2 \left(\frac{-3\alpha Q}{4\pi R^3 \rho_2} - \frac{1}{2}\left(\frac{-3\alpha Q}{4\pi R^3 \rho_2} - p_1 \left(v_1 - v_2\right) \right) \right) + \\ &A(v_1 - v_2)\left(\frac{v_1}{v_2} - 1\right) + \\ &B(v_1 - v_2)\left(\frac{v_1}{v_2} - 1\right)^2 + C(v_1 - v_2)\left(\frac{v_1}{v_2} - 1\right)^3 = 0 \end{aligned} \tag{2.6}$$

where v is equivalent to $1/\rho$. The only unknown in Equation 2.6 is ρ_2 (and, hence, v_2). Equation 2.6 can be solved iteratively for v_2, and the solution is used to solve the original Rankine-Hugoniot jump conditions for shock propagation speed U. CFD simulations have been employed to evaluate the result, along with Singh's original derivation. Shock speed predictions are further compared to a wave traveling at the acoustic sound speed. Setting shock propagation speed equal to the acoustic sound speed in water is an assumption that has commonly accompanied implementation of the similitude equations (*Shin*, 2004). The similitude equations are the most widely used analytical model for spherical underwater explosions to date, so the assumption that shock waves travel at the sound speed of the fluid is common.

The detonation of a single 1 g spherical charge of TNT in an infinite, undisturbed fluid has been simulated using the CFD solver with a 0.01 cm, one-dimensional computational grid extending 30 m out from the charge center. Shock arrival time was

monitored at 1 m increments. The arrival times predicted by each method were subtracted from the CFD arrival times at each spatial increment for comparison of the speed predicted by each method. Percent error was not used as a means of comparison because the percent error of arrival time becomes very small as arrival time increases at large distances. The maximum arrival time disparity from the CFD-predicted arrival time throughout the entire 30 m range, in seconds, has been tabulated for each method in Table 2.1 for 1 g and 100 g charges.

Method	1 g charge [s]	100 g charge [s]
Tillotson	1.26e-5	5.57e-5
Acoustic	2.89e-5	1.13e-4
Tait	1.40e-3	1.27e-3

Table 2.1: Maximum Arrival Time Discrepancies from CFD: 0-30 m

The speed generated using Singh's original method, which incorporated the Tait equation, correlates poorly with numerical results. The failure is partially due to the high sound speed it predicts (1538 m/s compared with 1483 m/s by the Tillotson equation). All CFD simulations were conducted using the Tillotson equation, somewhat dooming the potential of any method incorporating the Tait equation from the start. It is only appropriate to use the Tillotson equation to generate numerical data because it has been shown to be more accurate than the Tait equation. The Tillotson equation of state has also been used in the original validation cases for the CFD code. The constant speed assumption is respectably close to the CFD prediction for the 1 g charge. This can be attributed to the fact that small charges propagate linearly everywhere except very close to the charge. Simulations of larger charges were conducted to demonstrate the weakness of the constant speed assumption, with the results appearing in Table 2.1. It is evident that the Tillotson method corresponds to the CFD simulation best for this range of charge sizes. Because of its superiority over the existing means of shock propagation speed prediction, the Thomas Energy

Hypothesis combined with the Tillotson equation of state for water and the Rankine-Hugoniot jump conditions has been identified as a valuable new development in the prediction of spherical shock propagation speed.

2.1.2 Equation of State Failure

Combination of the Rankine-Hugoniot jump conditions, the Thomas Energy Hypothesis, and the Tillotson equation of state has has been found to accurately describe the propagation speed of spherical shock waves in undisturbed fluid (*Stowe and Vlahopoulos*, 2012). However, this approach, which has been described above, fails to accurately determine shock propagation speed in a disturbed fluid. When the shock wave travels into fluid that is pre-shocked (pressure and density are increased above ambient values) the propagation speed prediction falls below the sound speed in the pre-shocked fluid. By definition, shock waves never travel slower than the sound speed in the fluid. The model, therefore, has failed in this instance.

Figure 2.2 depicts shock propagation speed predicted by the Tillotson equation for a shock traveling into a still fluid of varying state. In the first case, the fluid state

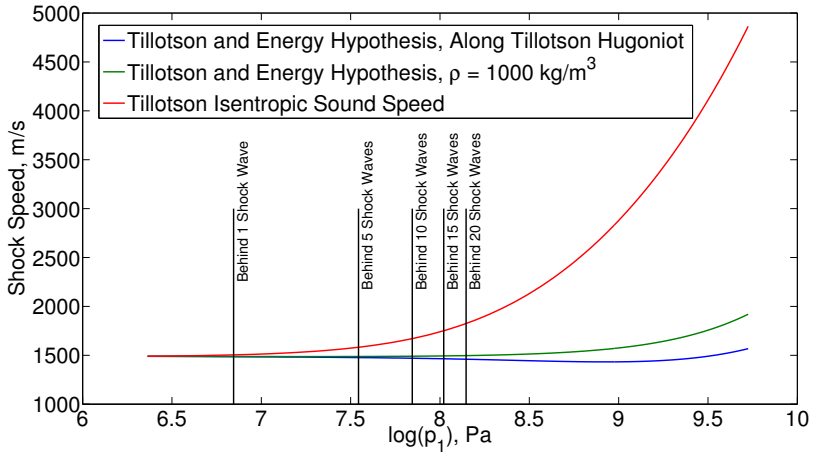

Figure 2.2: Shock Propagation Speed Prediction, Energy Hypothesis - Tillotson Equation Method

is defined by pressure-density pairs that form the points on the Tillotson Hugoniot

curve. Internal energy is assumed to be constant. This is a reasonable assumption as the magnitude of the energy jump terms in the Tillotson equation at a 1 m standoff for the shock wave produced by a 1 g charge are approximately 10000 times less than the magnitude of the pressure and density terms in the Tillotson equation at that radius. For the second case, propagation speed for a shock traveling into an increasingly pressurized fluid with constant density is plotted (with density set to the ambient value, or 1000 kg/m^3). Using constant density should generally result in an over-prediction of shock propagation speed. Sound speed in the fluid (a function of pressure and density, since internal energy is neglected) is calculated as well. The predicted speeds are based on a standoff of 0.5 m from a 1 g charge. Shock propagation speed predicted using the Energy Hypothesis - Tillotson equation method is not only less than the sound speed, but it also initially decreases as pressure increases! The net effect, when this model is included in a multiple source framework, is that trailing shock waves *decelerate* rather than accelerate in the wake of a leading shock. For reference, the isentropic sound speed in water using the Tillotson Equation can be derived as:

$$c = \sqrt{\frac{\omega p}{\rho} + \omega\left(e - e_o\right) + \frac{A + 2B\left(\frac{\rho}{\rho_o} - 1\right) + 3C\left(\frac{\rho}{\rho_o} - 1\right)^2}{\rho_o}}. \tag{2.7}$$

The Energy Hypothesis - Tillotson equation method also exhibits a peculiar behavior concerning the internal energy jump predicted across a shock traveling into a pre-shocked fluid. Figure 2.3 demonstrates a predicted decrease in internal energy as density of the undisturbed fluid increases beyond a certain threshold. To produce this plot, the Tait equation (Equation 2.2) was used to approximate pressure-density pairs which were then substituted into the Tillotson equation (Equation 2.1) to calculate the corresponding change in internal energy. At very high densities, the predicted density falls below the energy at standard temperature and pressure (represented by

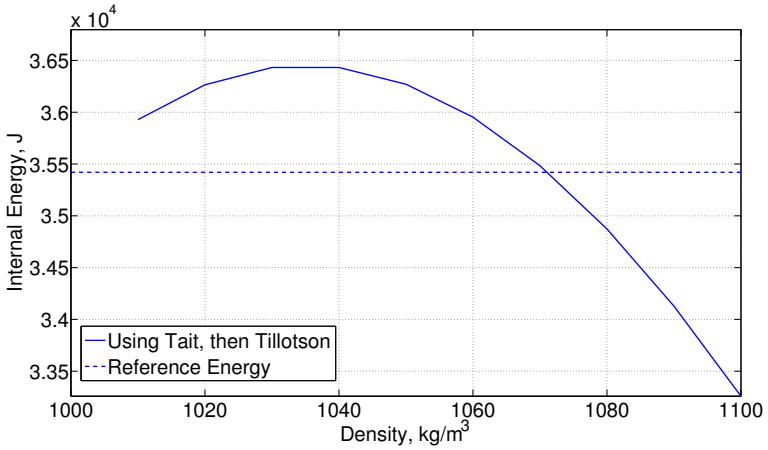

Figure 2.3: Tillotson Equation Internal Energy Failure

the dotted line). This behavior demonstrates the weakness of the Energy Hypothesis - Tillotson equation approach for disturbed fluids. The shock waves produced by the multiple-source array travel in heavily disturbed fluids. Although this method has been validated for spherical shock waves propagating in undisturbed fluid, the results in Figures 2.2 and 2.3 demonstrate that this approach is ill suited for implementation in the analytical model for the multiple-source array, where shocks propagate into heavily disturbed fluid.

The Tait equation of state for water struggles to represent shock waves traveling into pre-shocked media as well. This is shown in Figure 2.4, where shock propagation speed is again predicted to be less than the sound speed of the fluid into which the shock is propagating. In this case, shock speed is calculated using the Rankine-Hugoniot jump condition for continuity, Equation 2.4a (completely separate from the Thomas Energy Hypothesis). Assumed particle velocity values have been used in the calculation and are shown in Figure 2.4 as well.

2.1.3 A New Perspective on an Old Method

The failure of the methods above to predict shock propagation speed in a disturbed fluid is problematic. Shock waves generated by the multiple-source explosive

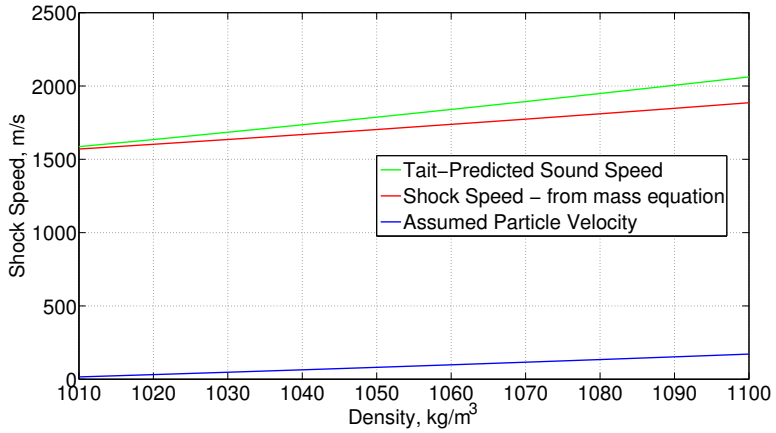

Figure 2.4: Tait Equation Shock Propagation Speed Failure

array interact with one another and acceleration of trailing waves is a common and important phenomena to capture. The weak shock formulation provides another avenue for shock propagation speed modeling, yielding the following equation for shock propagation speed (*Rogers*, 1977):

$$U = c_o + \frac{1}{2}\beta u \tag{2.8}$$

where c_o is the ambient sound speed in the fluid, β is a nonlinearity parameter for water, and u is the particle velocity. Shock waves not only compress water, increasing c_o, but they also accelerate water particles. This twofold effect leads to shock propagation speeds that are greater than the ambient-pressure sound speed (in direct contradiction to the behavior exhibited in Figures 2.2-2.4). Fluid compression and acceleration is also the mechanism by which trailing waves catch up to leading shocks (*Courant and Friedrichs*, 1948). Trailing waves travel through excited fluid characterized by a higher sound speed than the fluid into which the leading shock is propagating. Even simple waves catch the shock because the shock front propagates at a speed less than the sound speed immediately behind it. An expression for shock front propagation speed that demonstrates a front traveling slower than the fluid

behind it falls out of the 'weak' derivation of shock speed:

Let the mass flux be given by:

$$Q = \rho u \tag{2.9}$$

and let the shock be weak, such that particle velocity is much less than sound speed:

$$Q = Q(\rho). \tag{2.10}$$

The Rankine-Hugoniot Jump Condition for mass is given by:

$$U = \frac{Q(\rho_1) - Q(\rho_1)}{\rho_2 - \rho_1}. \tag{2.11}$$

At small perturbations of density, shock propagation speed trends toward characteristic velocity:

$$c^2 = \frac{\partial Q}{\partial \rho}. \tag{2.12}$$

Expanding Q about ρ_1 using a Taylor series gives:

$$Q(x) = Q(\rho_1) + Q'(x - \rho_1) + \frac{1}{2}Q''(\rho_1)(x - \rho_1)^2. \tag{2.13}$$

Substituting this equation into the continuity jump condition and the characteristic speed definition ($c^2 = \delta Q/\delta\rho$) gives:

$$U = Q'(\rho_1) + \frac{1}{2}Q''(\rho_2 - \rho_1) + H.O.T. \tag{2.14}$$

and :

$$c(\rho_2) = c(\rho_1) + Q''(\rho_1)(x - \rho_1). \tag{2.15}$$

Combining these two equations, gives:

$$U = \frac{c(\rho_1) + c(\rho_2)}{2} \tag{2.16}$$

and using the definition of sound speed in a disturbed fluid (*Whitham*, 1974), an expression for shock front propagation speed in terms of c_o, u_1, and u_2 is determined:

$$U = c_o + \frac{1}{2}\beta(u_1 + u_2). \tag{2.17}$$

This formulation has been implemented in the reduced-order model to calculate shock speed in the present model for both still and disturbed fluid, with one significant deviation from the literature. The highest value for β (also known as the nonlinearity parameter for water) that the authors have seen is 3.8 (*Cooper*, 1996). Singh uses a value of 3. Comparisons with numerical results have been conducted for single 1 g and single 1 lb charges propagating into undisturbed water and are plotted in Figures 2.5 and 2.6, using Equation 2.17 and β values from Cooper and Singh. A new proposed value for the nonlinearity parameter for water (5) is also used.

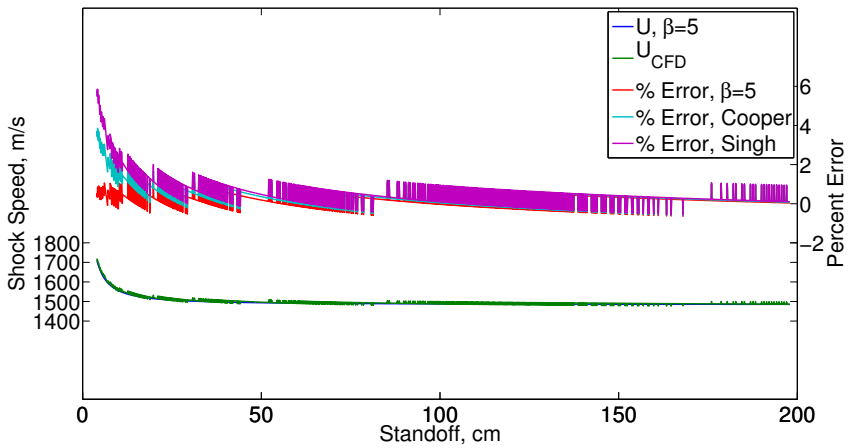

Figure 2.5: Shock Speed Comparisons: Single 1 g Charge

Data for the 1 g case is somewhat noisy due to the extremely fine increments

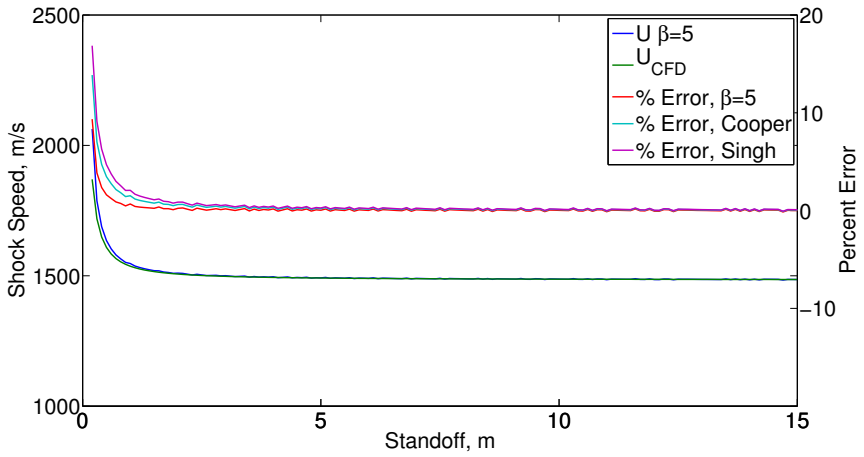

Figure 2.6: Shock Speed Comparisons: Single 1 lb Charge

used to monitor shock speed. The computation utilized a spherically-symmetric one-dimensional mesh and shock velocity was determined by calculating peak pressure arrival time at monitoring points spaced 0.1 cm apart. For the 1 lb case, shock arrival time was observed at 10 cm increments. Results for the 1 g case are shown in Figure 2.5 and results for the 1 lb case are shown in Figure 2.6. Particle velocity data used to calculate shock front propagation speed was generated using the CFD code. The only variable in Equation 2.17 not directly taken from CFD results is β. The correct tuning of β, therefore, should yield a close correlation with the numerical results. It is evident that the published values for beta fall short in this pursuit, given the deviation from the shock speed seen in CFD simulations of the near-field. Analysis has shown setting $\beta = 5$ yields a better agreement with the CFD simulations. The shock propagation speed calculated using the new β value is compared with the CFD-predicted speed on the 'Shock Speed' axes.

Calculating propagation speed using the weak shock formulation and new value for the nonlinearity parameter in water has been shown to be effective for single charges above. An added benefit over the Energy Hypothesis - Tillotson equation approach is that shock speed calculated in the weak sense will always increase when the initial fluid has been pre-shocked. This is critical and a significant advantage over

the other methods described earlier in the chapter. The weak shock formulation has been integrated into the physics-based, reduced-order model as a means of predicting shock front propagation speed in both still and disturbed media.

2.2 Shock Pressure Waveform

2.2.1 Similitude Equations

Single shock waves are characterized by their pressure waveform as well as propagation speed. The pulse from a single spherical explosive source is comprised of a sharp peak followed by exponential decay to an equilibrium state. A typical pressure-time history for a single charge is depicted in Figure 2.7. Optimization of the composite pressure wave at the target is the objective of the multiple-source explosive array design. It is critical, therefore, to accurately capture pressure wave behavior at the target. Shock interactions occur on the path to the target and are largely dependent on shock amplitude as well. This section details the method used in the analytical model to define the pressure waveform produced by a single shock.

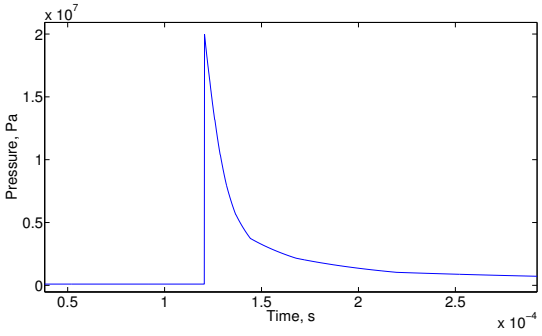

Figure 2.7: Typical Spherical Shock Pressure Waveform

2.2.2 Weak Shock Theory, an Adaptation

Singh's method for calculating propagation speed provides shock properties as a function of radius. The Rankine-Hugoniot jump conditions describe the jump across

a shock front, but any temporal effects are left undefined. Impulse, the integral of pressure over time, is a critical metric for the effectiveness of the array. Because impulse and the composite waveform at the target must be modeled (not just the pressure peaks), it is important to calculate state variables as a function of time. Weak shock theory has been implemented to address this need and is used to predict temporal and spatial decay of both pressure and particle velocity in the analytical model.

As developed by Rogers, weak shock theory includes the assumption that the linear impedance relation accurately relates pressure and particle velocity in water (*Rogers*, 1977). The linear impedance relation is:

$$p = \rho_o c_o u \tag{2.18}$$

where ρ_0 is the fluid density at ambient pressure. The acoustic velocity behind the shock front is given by the following relation:

$$c_a = c_o + \beta u \tag{2.19}$$

which gives

$$u = f\{t - [1 - (\beta u/c_o)](x/c_o)\} \tag{2.20}$$

for small values of u/c_o (*Blackstock*, 1966). As we have seen, the shock front for a wave propagating into an undisturbed fluid is given by:

$$c_s = c_o + \frac{1}{2}\beta u \tag{2.21}$$

meaning that the shock front is constantly being overtaken by the acoustic wave behind it. Another assumption is that at some radius close to the charge, the pressure-

time history remains exponential at all time. Therefore,

$$p = p_o e^{(-t/\tau_o)} \tag{2.22}$$

where τ_o is the decay time constant of a near-field pressure history. By the linear impedance relation:

$$u = u_o e^{(-t/\tau_o)}. \tag{2.23}$$

Use of Equation 2.23 leads to:

$$\hat{u} = e^{-(\hat{t}+\hat{u}\hat{x})} \tag{2.24}$$

with $\hat{u} = u/u_o$, $\hat{t'} = (t - x/c_o)/\tau_o$, and $\hat{x} = \hat{s}(\hat{u})$, which is the dimensionless distance where a point on the waveform that has been trailing the shock front catches up to the shock front. Finally, this gives

$$\hat{u}_m(\hat{x}) = \hat{s}^{-1}(\hat{x}) \tag{2.25}$$

and

$$p_m(\hat{x}) = p_o \hat{s}^{-1}(\hat{x}). \tag{2.26}$$

With these equations in place, the function $\hat{s}(\hat{u})$ can be found by performing a time-based discretization of an original time history near the charge. The distance where a point behind the shock overtakes a point on the shock can be calculated and rearranged into a recursive equation that is then transformed into a differential equation governing $\hat{s}$, namely:

$$\frac{1}{2} d\hat{s}(\hat{t})/d\hat{t} = e^{\hat{t}} + \hat{s}(\hat{t}). \tag{2.27}$$

This is solved using the initial conditions $\hat{s} = 0$ at $\hat{t} = 0$. Rogers implements this solution in spherical coordinates to develop the expression used in the present model

to predict peak pressure for a single charge:

$$p_m(R) = \frac{p_o\{[1 + 2(R_o/l_o)ln(R/R_o)]^{1/2} - 1\}}{(R/l_o)ln(R/R_o)}. \tag{2.28}$$

An expression for the initial decay time constant as a function of radius using the equation for peak velocity is also derived, giving:

$$\tau(R) = \tau_o[1 + 2(R_o/l_o)ln(R/R_o)]^{1/2}. \tag{2.29}$$

As Rogers acknowledges, this is only the initial decay constant. The pressure decay of an underwater shock wave is not perfectly exponential. A curve fit of an original pressure history recorded near the source using a single exponential function is compared to CFD results in the left plot of Figure 2.8. The discrepancy between the

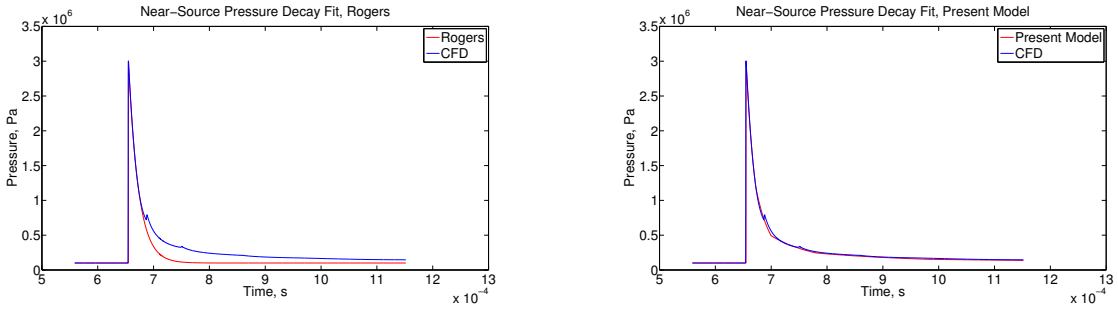

Figure 2.8: Curve Fit Comparisons, Single Decay Constant and 20 Decay Constants

curves is stark and highlights the fact that single exponential decay is an insufficient model for the pressure wave produced by a spherical explosive charge. Weak shock theory has been modified to address this issue. The initial curve is subdivided into several individual exponential segments, each with a unique decay constant. These separate curves are propagated in accordance with weak shock theory and fused together at the points of interest to reconstruct the total waveform. This approach leads to a much closer curve fit throughout the range of interest and is pictured for

the original pressure history on the right in Figure 2.8. For this analysis, weak shock theory is used to model the detonation of TNT. Weak shock theory has also been successfully used to model other explosive materials (*Liddiard and Forbes*, 1983).

An original pressure history near the shock source is procured from numerical results. The number of segments necessary to characterize the initial history varies with charge size. If an excess of segments is used, the curve fits that define the initial decay constants at the source become linear - a poor representation of the actual pressure time curve. At any point in the fluid where the pressure is desired, the segments are fused together to construct the waveform. The fusion of one segment to another proceeds as follows. The first segment, which is fitted to the peak section of the original near-field history, dictates the peak as well as the initial decay. As time progresses, the first segment will eventually define a pressure that is below the peak value of the second highest segment. At this time, the second highest segment is used to define the curve until a time where the peak value of the third segment is higher than the value of the pressure given by the second segment at that time. At this moment, the third segment begins to determine the waveform shape and so on.

Impulse histories for a single 1 g spherical charge of TNT are shown for standoffs of 1 m and 30 m in Figures 2.9 and 2.10. The line titled 'WS' on the impulse curve is the weak shock theory result with only one segment, or decay constant. It is compared with a curve defined by twenty segments, denoted by 'Adapted WS'. Twenty decay constants have been selected because they sufficiently capture the waveform shape throughout the range of interest. With five decay constants, weak shock theory predicts impulse within 9.15% of the CFD-calculated impulse at 30 m. Using twenty decay constants, weak shock theory predicts impulse within 1.41%. The impulse curves are truncated where the pressure in the CFD simulation becomes negative. This behavior is related to the gas bubble and the conservation equations. The negative portion of the pressure wave is not a factor in energy focusing in the range

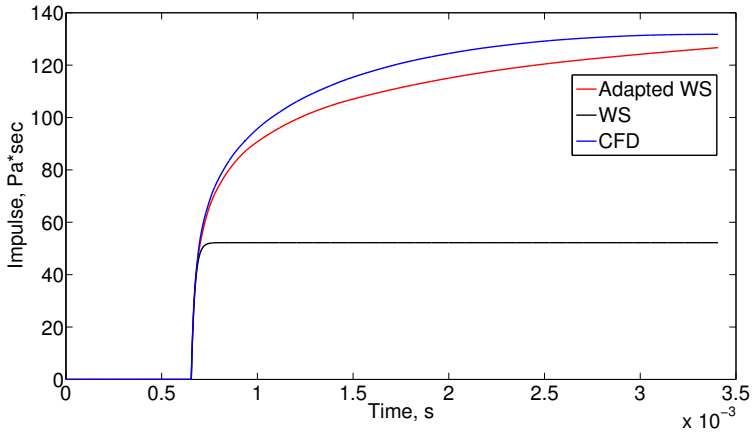

Figure 2.9: Single 1 g Spherical Source Impulse Prediction, 1 m Standoff

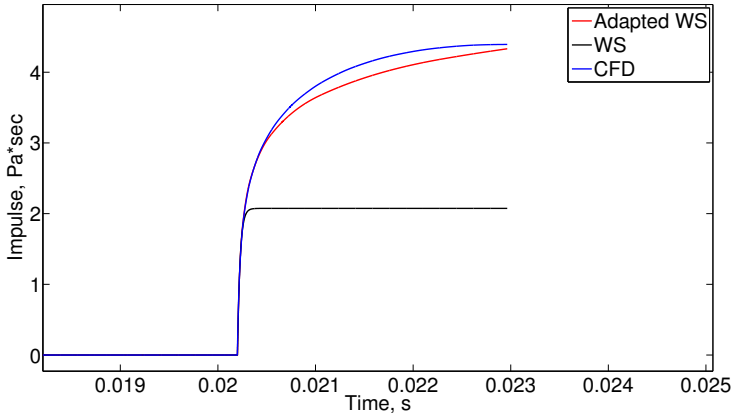

Figure 2.10: Single 1 g Spherical Source Impulse Prediction, 30 m Standoff

of interest, however, and has not been included in the model.

At both 1 m and 30 m standoffs, the modified version of weak shock theory sufficiently predicts impulse and greatly improves upon existing methods. As a final metric, peak pressure predictions calculated by CFD and weak shock theory are compared in Figure 2.11 as well as percent difference in impulse prediction in Figure 2.12. In the past, weak shock theory has been used to predict impulse in the far-field linear domain of shock wave propagation (*Cudahy and Parvin*, 2001). Here, weak shock theory is shown to model both the near-field and far-field well for a 1 g spherical charge of TNT.

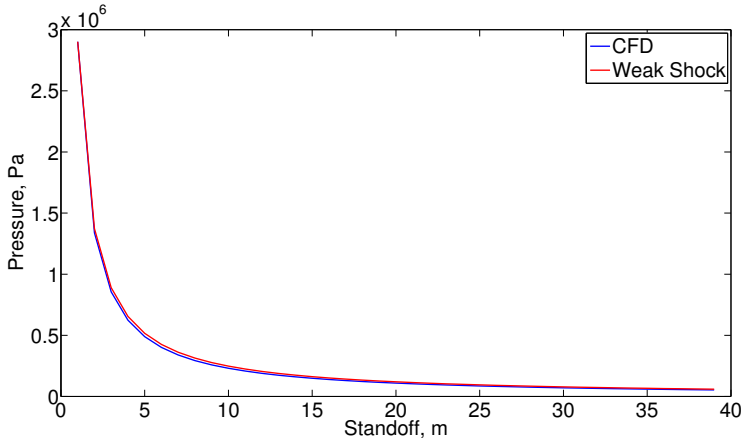

Figure 2.11: Single 1 g Spherical Source Peak Pressure Comparison

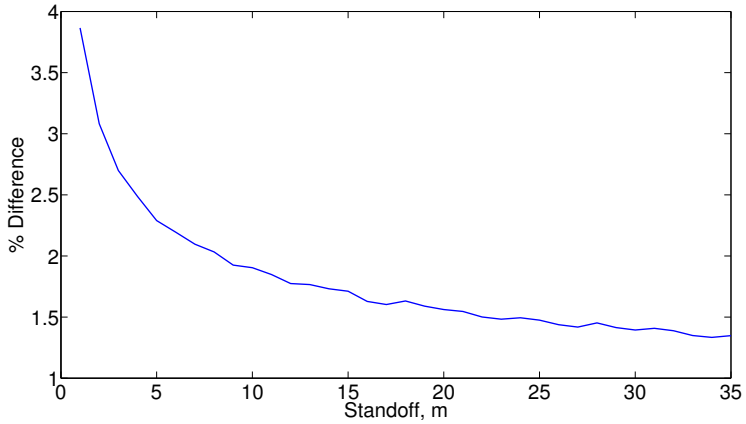

Figure 2.12: Single 1 g Spherical Source Impulse Prediction Error, Analytical Model Results vs. CFD Results

Weak shock theory is used to determine particle velocity in the analytical model. Weak shock theory, therefore, is used not only to predict pressure but is used to predict shock propagation speed as well. Figure 2.13 demonstrates the accuracy of the weak shock theory implementation for particle velocity, where u' is the nondimensionalized particle velocity u/c_o.

A final modification to weak shock theory has been developed to increase the accuracy of the method. Original histories generated by the numerical tool are recorded at varying standoffs from the charge. As a shock wave passes each of these standoffs,

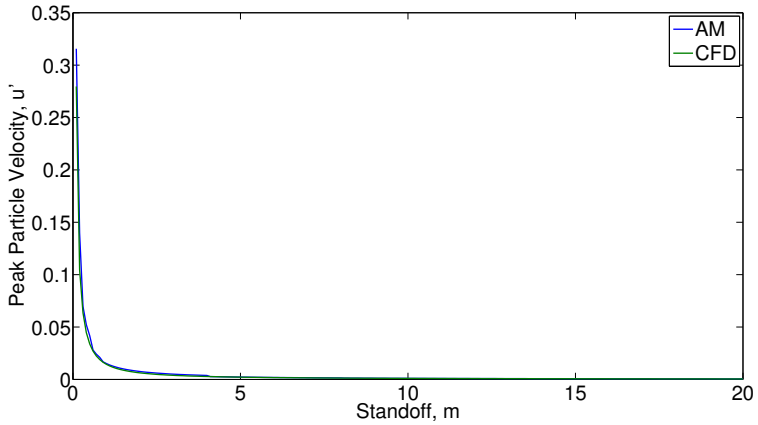

Figure 2.13: Single 1 lb Spherical Source Particle Velocity Comparison

the original history at that point begins to define the weak shock segments, superseding histories taken closer to the charge. This correction has been included because the waveform shape is subject to change slightly as the shock propagates away from the target. The peak becomes less sharp and the wave tail begins to widen. Recalibrating the shock as it propagates beyond known waypoints is an effective method of maintaining accuracy in the reduced-order model.

2.3 Chapter Summary

This chapter has described the technical underpinnings used to model the behavior of a single spherical shock wave. Singh's propagation speed approach has been rederived using the Tillotson equation of state for water. Although this approach yielded satisfactory results for shocks propagating in undisturbed fluid, the method struggled to predict speed in a shocked fluid accurately. This is a critical shortcoming in the context of the multiple-source explosive array because individual shocks interact and accelerate each other. The weak formulation for shock front propagation speed has been applied to the problem and an improved value for nonlinearity parameter for water has been identified.

Weak shock theory, as it pertains to pressure and particle velocity, was derived

and Rogers' initial method was improved by discretizing the 'seed' waveforms into segments. This technique enables shock tails to be resolved with higher accuracy, leading to better predictions downrange. In the next chapter, single shock effects will be used to determine the magnitude and type of several multiple-source interaction phenomena.

CHAPTER III

Multiple-Source Effects

The behavior of shock waves produced by single spherical explosive sources has been detailed in the previous chapter. The modeling techniques introduced in Chapter II capture propagation and attenuation of solitary shock waves as they propagate away from their origin. During the preliminary phases of this research effort, it seemed that modeling single source effects was sufficient to represent the behavior of the multiple-source explosive array. Several early studies using two-charge line arrays indicated that the simple superposition of single source results correlated well with numerical data generated with two-dimensional grids where shocks traveled in the midst of one another.

The correlation deteriorated, however, when more charges were used or when charges were spaced closer together. The tail of the composite waveform dropped off abruptly in these configurations, removing impulse from the shock tail. Interacting shock waves began to outpace their superposition counterparts as well. Lastly, peak pressure at the target exhibited unexpected attenuation.

This chapter will identify the physical causes behind each of these unexpected behaviors. Rarefaction waves, shock coalescence, and shock-rarefaction interactions will be explained, and the methods used to model these phenomena will be enumerated. reduced-order models for the multiple-source effects discussed here have been

integrated into the comprehensive analytical model for the multiple-source explosive array.

3.1 Rarefaction Waves

The near-field becomes chaotic when charges in the multiple-source array are detonated. Figure 3.1 depicts numerical results for pressure that underscore the complexity of the near-field flow. Shock waves propagate amongst each other and interact in important ways which influence the composite waveform at the target. Shock waves are not the only wave type produced by the multiple-source array, however.

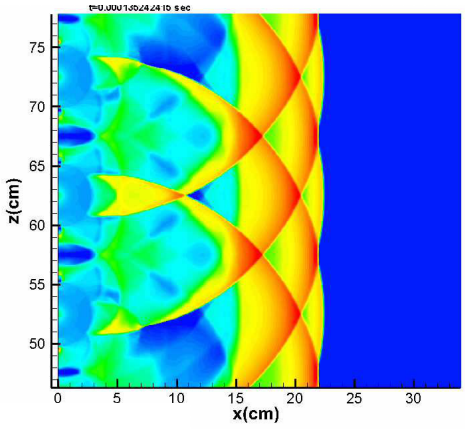

Figure 3.1: Complex Near-field Flow from Multiple-Source Explosive Array

As explained in Chapter I, an explosive gas bubble is created during the detonation process. The bubble expands and contracts cyclically, gradually floating to the surface where it is vented. Shin gives the bubble oscillation period for a 1 g charge submerged to 3 m depth to be 0.0271 seconds (*Shin*, 2004). The shock produced by a 1 g spherical explosive source reaches the explosive gas bubble of a neighboring source 10 cm away in less than 5×10^{-5} s. The rate of bubble expansion (and eventually, contraction), therefore, is slow relative to the speed of shock waves produced by 1 g charges. Based on the drastically different time scales of bubble period and shock

propagation, bubble oscillation effects can be neglected in the analytical model for the multiple-source array.

Although bubble oscillation effects have been ignored, the bubble itself must be modeled to accurately predict the composite waveform produced by the array. The existence of gas-filled bubbles in the midst of shock waves leads to waves of a different kind. Rarefaction, or expansion, waves are unlike shock waves in many regards. A rarefaction wave relaxes the fluid, reducing pressure, density, and particle velocity, while a shock wave does the opposite. Rarefaction waves have finite rise times, meaning pressure at the trough (the rarefaction analogue of the shock peak) is not reached instantaneously. Finally, unlike the tendency of points behind the shock to catch up to the front due to the increased acoustic speed in the shock wake, a rarefaction wave spreads as it propagates. The head of the wave travels faster than the tail because the tail travels in a relaxed fluid.

In most underwater explosion studies, rarefaction waves appear when a shock wave is incident upon the free surface. Conservation equations at the boundary dictate that an expansion wave must be reflected back into the fluid to offset the shock effects at the interface. In the multiple-source explosive array, explosive gas bubbles act as reflective surfaces, much like the free surface of a body of water. The presence of gaseous bubbles is accounted for in the analytical model by including theoretical representations of rarefaction wave strength and rarefaction wave propagation speed.

3.1.1 Rarefaction Strength

3.1.1.1 Conservation at the Interface

The Rankine-Hugoniot jump conditions can be combined with the ideal gas law to examine the physics present at a shock interface. Two fluid states separated by an interface is often referred to as the Riemann problem. The jump conditions for a shock propagating from left to right (in a one-dimensional sense) can be rewritten as

the following family of equations (*Smoller*, 1983):

$$\frac{p_r}{p_l} = e^{-x}, \tag{3.1a}$$

$$\frac{\rho_r}{\rho_l} = \frac{1+\beta e^{-x}}{\beta + e^{-x}}, \tag{3.1b}$$

$$\frac{u_r - u_l}{c_l} = \frac{2\sqrt{\tau}}{\gamma - 1}\frac{1 - e^{-x}}{\sqrt{1+\beta e^{-x}}} \tag{3.1c}$$

where $x = -log\left(\frac{p_r}{p_l}\right)$ and γ is the ideal gas constant. The relations across simple waves, which include rarefaction waves, can be derived for an ideal gas as the following family of equations (for a shock moving from right to left):

$$\frac{p_r}{p_l} = e^{-x}, \tag{3.2a}$$

$$\frac{\rho_r}{\rho_l} = e^{-x/\gamma}, \tag{3.2b}$$

$$\frac{u_r - u_l}{c_l} = \frac{2}{\gamma - 1}\left(1 - e^{-\tau x}\right). \tag{3.2c}$$

These families of equations form the basis for the solution to the Riemann shock tube problem. Shock incidence upon a bubble surface is physically similar to a shock reaching an interface in a shock tube. Conservation conditions at the boundary are:

$$\frac{p_r}{p_l} = 1, \tag{3.3a}$$

$$\frac{\rho_r}{\rho_l} = e^{x}, \tag{3.3b}$$

$$\frac{u_r}{u_l} = 0. \tag{3.3c}$$

The three families of equations (the relations across shock waves, relations across simple waves, and the boundary conditions at an interface between two fluid states) are used to solve for the wave type and wave magnitude resulting from the collision of a shock with an explosive gas bubble. A final relation, known as the Lax entropy

condition, is required to close the system. This condition ensures that the resulting waves do not exist in such manner that entropy would be destroyed. The Lax entropy condition, as it pertains to the Riemann problem, can be derived as follows: Let the fluid on the left of an interface be gas from the explosive bubble and the fluid to the right of the interface be water. Using Smoller's notation, we define the following: $A = \rho_r/\rho_l$, $B = p_r/p_l$, $C = \frac{u_r - u_l}{c_l}$. Assuming that a vacuum cannot be created by the shock-bubble collision, the following must hold for a rarefaction wave to be propagated into the bubble:

$$\sqrt{\frac{B}{A}}\frac{2}{\gamma-1}\left(1-e^{\left(\frac{\gamma-1}{2\gamma}log(B)\right)}\right) < C < \frac{2}{\gamma-1}\left(1+\sqrt{\frac{B}{A}}\right). \tag{3.4}$$

If this inequality does not hold, a shock wave will be transmitted into the bubble. Similarly, the following must be true for the liquid side:

$$\frac{2}{\gamma-1}\left(1-e^{\left(\frac{1-\gamma}{2\gamma}log(B)\right)}\right) < C < \frac{2}{\gamma-1}\left(1+\sqrt{\frac{B}{A}}\right) \tag{3.5}$$

for a rarefaction to be transmitted into the liquid. Otherwise a shock is propagated into the liquid side.

These equations form the basis of the reduced-order model for shock-bubble collisions. One final component is missing. The families of equations above have been derived for an ideal gas. The ideal gas law lends itself to algebraic manipulation due to its simplified structure. Neither the Tait nor the Tillotson equation can be used in the above derivation; the algebra cannot be solved. Holl determined a functional form equivalent to the ideal gas law with the Tait equation, which allowed formulations from gas dynamics above to be applied in the liquid domain (*Holl*, 1982).

3.1.1.2 The Functional-Form Equivalent Tait Equation

As discussed in Chapter II, equations of state are used to describe the relationships between state variables in a fluid. The Tait equation of state for water relates pressure to density, as demonstrated in Equation 2.2. Values of $A = 3.31 \times 10^8$, $B = 3.31 \times 10^8$, and $N = 7.25$ have been used in the analytical model. Although analyses using the CFD code have employed the Tillotson equation of state exclusively, the code is able to incorporate the Tait equation. The values for A, B, and N above come from the Tait equation definition in the CFD tool. The modified Tait equation, a functional form equivalent of the ideal gas law, is given as:

$$\bar{P}_1/\bar{P}_o = (\rho_1/\rho_o)^N \tag{3.6}$$

where $\bar{P} = P + B$. This equation can be used to determine sound speed in a very familiar form:

$$c^2 = \frac{N\bar{P}}{\rho}. \tag{3.7}$$

The modified Tait equation can be substituted into the families of equations derived in the previous section to solve the Riemann problem at a gas-liquid interface. Chen and Cooke were the first to do this, and their development has been implemented into the physics-based, reduced-order model (*Chen and Cooke*, 1994).

3.1.1.3 Bubble Dynamics on the Shock Time-Scale

To model the cumulative effect of the multiple-source array at the target, the rarefaction waves produced by the shock-bubble collisions must be characterized. The method for solving the Riemann problem at a gas-liquid interface provides the means to solve the interface problem, but the initial state on the gas and liquid sides of the interface must be defined. Conditions on the liquid side are given by the impending shock, as modeled according to the methods outlined in Chapter II. The remaining

unknown is the fluid state on the gas side of the interface.

Numerical experiments were conducted to determine the effect of an incident shock wave on an explosive gas bubble. Figure 3.2 shows the pressure field near a bubble at the instant before the shock collides with the bubble, the instant just after collision, and at a time when the rarefaction wave is fully formed (low pressure fields indicated by the dark blue semi-circles propagate into the pressurized regions and counter overpressure from shock waves). Figure 3.3 shows density plots in which the bubble boundary can be clearly seen. The bubble shape and the expansion rate depicted in the density plots do not appear to be affected by shock collisions.

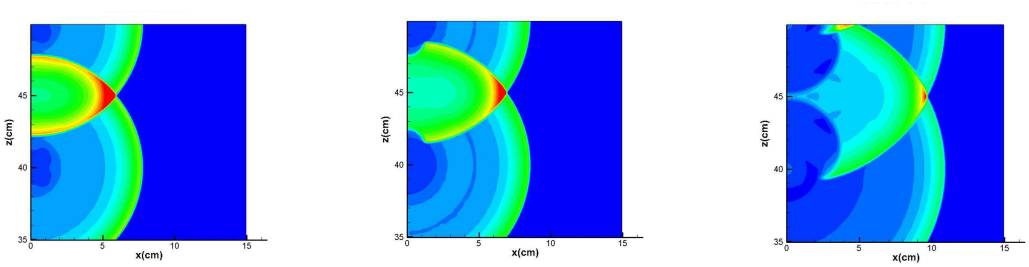

(a) (b) (c)

Figure 3.2: Rarefaction wave formation as seen in pressure contour plots a) just before the shock collides with the explosive gas bubble, b) just after the collision, and c) after rarefaction wave is fully formed

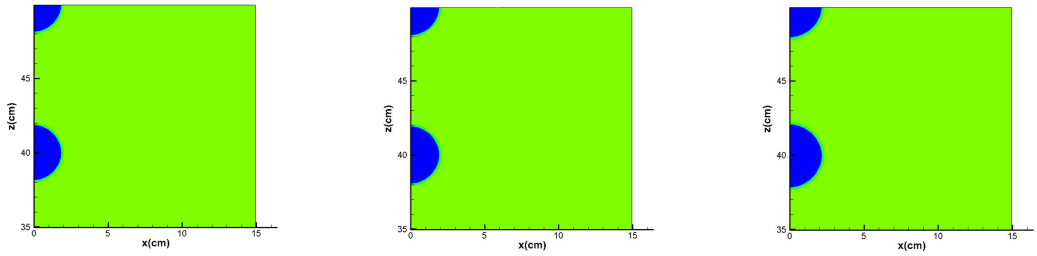

(a) (b) (c)

Figure 3.3: Bubble diameter as seen in density plots a) just before the shock collides with the explosive gas bubble, b) just after the collision, and c) after rarefaction wave is fully formed

These results demonstrate that bubble behavior is predictable because shock col-

lisions do not effect bubble geometry appreciably on the shock time scale. To characterize this behavior, CFD simulations have been conducted to collect bubble radius and state data as they vary with time. As implemented in the reduced-order model, the state of the explosive gas is queried from a lookup table that has been assembled from numerical simulation data. Knowing the initial explosive gas state as well as the initial state on the liquid side due to the shock, the approach of Chen and Cooke is applied to determine the rarefaction strength (*Chen and Cooke*, 1994). Validating this method is hampered by the difficulty in simulating isolated spherical rarefaction waves with the CFD tool. As a result, the rarefaction strength calculation is validated as part of the comprehensive model in Chapter IV.

3.1.2 Rarefaction Speed

Rarefaction waves propagate differently than shock waves in that rarefaction waves have finite rise time and spread as they propagate. As the rarefaction wave arrives, the overpressure is attenuated gradually. If a shock had arrived, the overpressure would jump discontinuously. The finite rise time occurs because of the nature of a rarefaction wave. The front of a rarefaction wave travels into fluid at an initial state, while the tail of the wave travels through fluid that has been relaxed from that initial state. The front travels faster than the tail, therefore, and arrives at the target first. Therefore, the rarefaction wave spreads as it propagates.

Rarefaction wave speed is calculated using the propagation speed of a nonlinear simple wave. The state of the fluid into which the rarefaction is propagating is known, therefore the speed of the head of the rarefaction wave can be calculated. Given the strength of the rarefaction wave, conditions at the tail of the wave can be determined. Propagation speed of the tail is determined by the acoustic wave speed in the relaxed fluid. This method has been integrated into the comprehensive model.

3.1.3 Numerical Comparisons

In the reduced-order model, the post-collision pressure on the liquid side of the explosive gas bubble interface is subtracted from the incident shock pressure to determine the initial magnitude of the rarefaction wave. Modeling initial strength alone is insufficient. Spatial and temporal attenuation of rarefaction waves must be calculated as well. CFD simulations were used to study rarefaction wave decay, and an analytical method for predicting rarefaction wave decay in space and time has been validated.

Pressure histories for three and five charge line arrays have been simulated and compared with linearly-combined single charge simulations. The superposition runs were conducted so that the results corresponded with the spacing and detonation timing of the line array simulations. Identical computational grids were used for both the line array simulations and the single charge runs. In the line array simulations, where individual shock waves were free to interact, shock coalescence caused shock waves to travel faster than the superposition runs. To account for this, peak arrival time of superposition waves has been modified so that each superposition peak arrives at the same time as its respective line array simulation analogue. As a result, rarefaction wave effects have been isolated from shock coalescence for examination.

The line array simulations, which included shock-bubble collisions, were conducted with a very low cavitation floor. The cavitation floor is the minimum pressure permitted by the CFD code. By allowing very low pressures to occur, the true strength of the rarefaction wave can be determined when compared with superposition. With the default cavitation floor of 5×10^4 Pa, the rarefaction troughs are occasionally truncated before they reach their minimum pressure.

A comparison between line array and superposition results for a three charge line array is shown in Figures 3.4 and 3.5. Note that the initial sharp trough in the Figure 3.5 at approximately 2.6×10^{-4} s is not a rarefaction wave; rather, it is the

result of differing peak pressure values for superposition and the two-dimensional analysis.

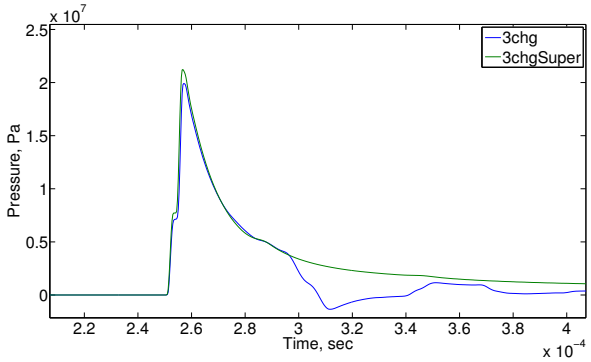

Figure 3.4: Three 1 g Source Line Array, Superposition vs Interacting Results, 40 cm Standoff

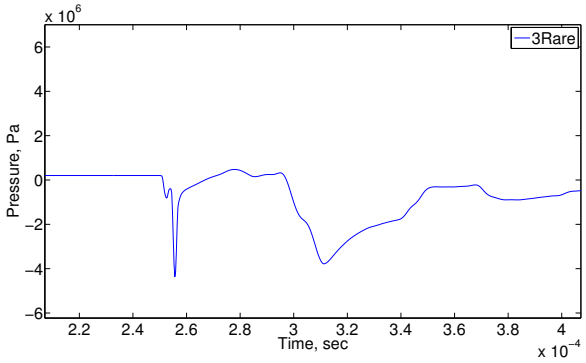

Figure 3.5: Three 1 g Source Line Array, Isolated Rarefaction Waveform, 40 cm Standoff

For comparison, similar plots are given for the five charge line array in Figures 3.6 and 3.7. Two distinct troughs can be seen in the rarefaction waveform produced by the five charge line array. The five charge array, when each charge is detonated simultaneously, creates three distinct rarefaction waves along the centerline (one from the center bubble, one from the intermediate bubbles, and one from the outer bubbles). By the time the wave train has propagated to the standoff shown in Figure 3.7, the first and second rarefaction troughs have merged.

Rarefaction strength has been plotted versus distance to determine spatial decay in Figure 3.8. The rarefaction strengths denoted 'First Wave' and 'Second Wave'

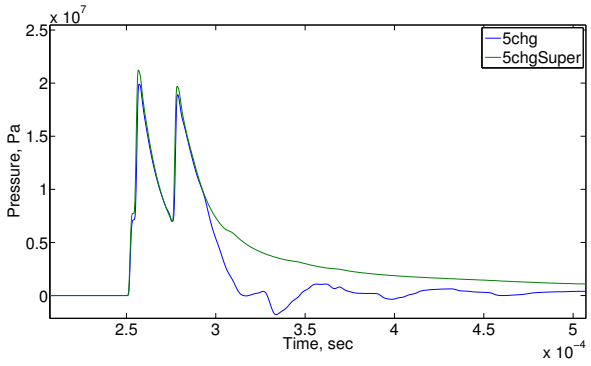

Figure 3.6: Five 1 g Source Line Array, Superposition vs Interacting Results, 40 cm Standoff

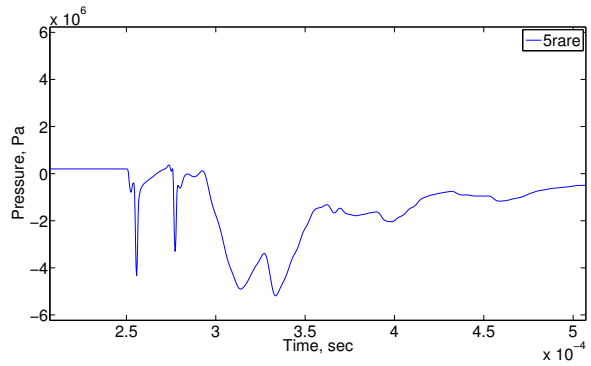

Figure 3.7: Five 1 g Source Line Array, Isolated Rarefaction Waveform, 40 cm Standoff

represent the magnitude of rarefaction troughs produced by the three-charge line array, such as those appearing in Figure 3.5. Merging of the two discrete waveforms occurs at 40 cm, after which the rarefaction waves produced by the three-charge line array propagate as one waveform. Rarefaction strengths determined from the line array - superposition comparison are compared with a $1/R$ spatial decay, which is characteristic of a spherical acoustic wave. The initial rarefaction strength for the acoustic decay curves is set to the initial observed value from the numerical study. Figure 3.8 demonstrates that simple acoustic decay is a reasonable approximation for a reduced-order model and can be used to represent the attenuation of a rarefaction wave as it propagates through space.

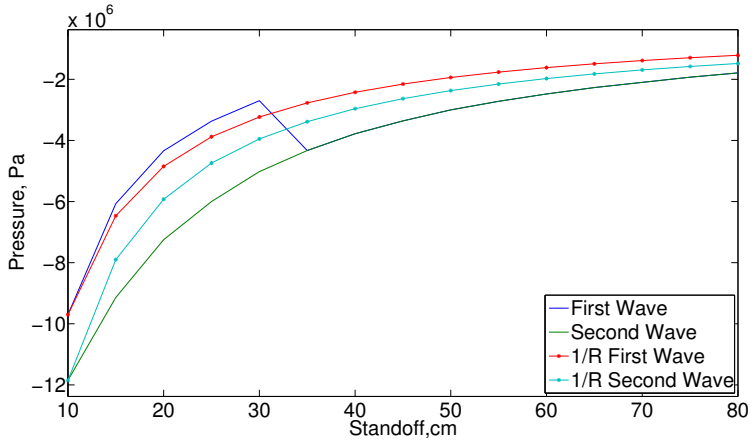

Figure 3.8: Rarefaction Wave Spatial Decay, Three 1 g Charge Line Array

3.2 Shock Coalescence

The creation of rarefaction waves is an important multiple-source effect and it must be included in the physics based reduced-order model. Other multiple source effects are equally important. Shock coalescence, or the tendency of trailing shock waves to catch up to and merge with leading shock waves, plays a critical role in the final composite waveform profile at the target. Figure 3.9 shows the progression of the wave train produced by a five charge line array with each source detonated simultaneously. Individual shocks interacted with one another and each pressure history was recorded at the stated standoff out from the center charge in the array. Superposition results generated by adding pressure histories from solitary shocks are plotted for comparison.

As waves produced by the multiple-source array propagate toward the target, trailing waves are accelerated and drawn into leading shocks. Acceleration can be observed where the interacting peaks outpace their superposition counterparts. The composite waveform generated from superposition results demonstrates coalescence as well, but this effect is due to geometry (when the target is moved far from the array, the distance between each charge becomes negligible and they appear to reach the target at the same time for simultaneous detonation schemes). Geometric coa-

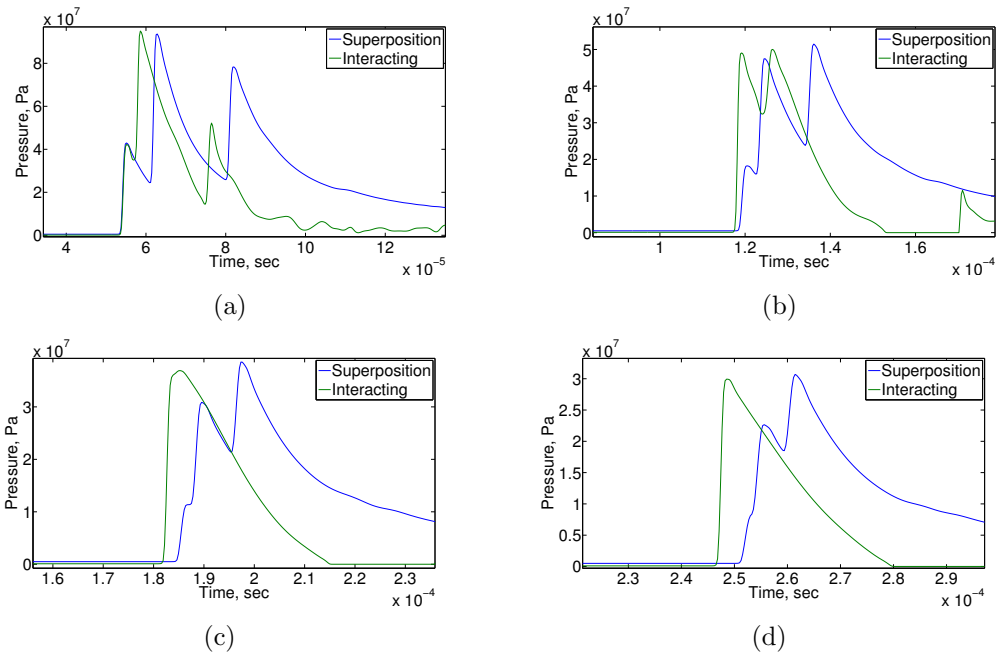

Figure 3.9: Superposition vs. interacting shock progression of wave train produced by five charge line array at a) 10 cm standoff, b) 20 cm standoff, c) 30 cm standoff, d) 40 cm standoff

lescence occurs at later times and further standoffs than coalescence caused by shock interaction.

The aggregate effect of trailing wave acceleration is twofold. First, energy is shifted toward the front of the waveform, as evidenced by the higher first peak seen at the 30 cm and 40 cm standoffs for the interacting wave simulation when compared with superposition in Figure 3.9 . Second, impulse is preserved, since the rarefaction waves arrive later relative to the shock peaks. When the rarefaction waves arrive later, the shock is able to decay further before being nullified by the rarefaction waves. Therefore, more energy is delivered to the target as the shock waves escape deleterious rarefaction effects for a few moments more than they would with no coalescence modeling.

Recent studies have explored coalescence of spherical shock waves experimentally. Exploding copper and nichrome wires were used to create blast waves in proximity to one another, and schlieren photographs were taken to capture the interaction

(*Higashino et al.*, 1991). Mach stems that can be seen in the images also appear in field plots from CFD analyses conducted during the present research effort. The formation of mach stems informs the shock coalescence modeling approach that has been implemented in the physics based reduced-order model.

Analytical models for shock coalescence do not appear in the literature. Kandula and Freeman studied shock coalescence experimentally and numerically (*Kandula and Freeman*, 2008). The models offered for shock coalescence deal only with the peak pressure of the coalesced wave, neglecting the coalescence process, which is a gradual progression. All numerical studies of both 1 g and 1 lb spherical charges indicate that superposition is a sufficient method for capturing peak pressure of the coalesced wave front, provided that rarefaction waves and shock-rarefaction interactions are accounted for. The latter multiple source effect has significant bearing on peak amplitudes and is described in the following section.

3.3 Shock-Rarefaction Interactions

A third important multiple-source effect is attenuation that occurs due to the interaction of shock waves and rarefaction waves. In large multiple-source arrays, shock waves from outer sources overtake rarefaction waves produced by inner source bubble collisions before the entire wave train collectively reaches the target point. Both shock waves and rarefaction waves are weakened when shocks overtake rarefaction waves. The extent of the attenuation is dependent on the state behind the shock before the interaction (state L), the state between the shock and rarefaction before the interaction (state 0), and the state in front of the rarefaction before the interaction (state R). The shock tube is used as a model for this process. The instant just before a trailing shock overtakes a leading rarefaction in a shock tube is shown in Figure 3.10.

The instant after the interaction is shown in Figure 3.11. Two oppositely-propagating waves always result from a shock-rarefaction interaction in a shock tube. These waves

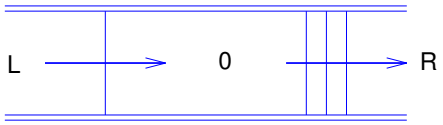

Figure 3.10: Shock Tube Diagram - Before Interaction

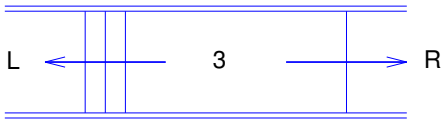

Figure 3.11: Shock Tube Diagram - After Interaction

can be any combination of shocks and rarefactions and the wave type is dependent on the properties of the fluid. The amplitude of the reflected waves is calculated in a similar fashion to the gas-liquid interface problem solved in Section 3.1.1.1. The change of state across simple waves and shock waves is constrained by physical relationships. From the method of characteristics, we know the relation across a rarefaction wave for a polytropic gas is (*Courant and Friedrichs*, 1948):

$$u_b = u_a \pm \frac{\sqrt{1-\mu^4}}{\mu^2}\left(\frac{1}{\rho_a}\right)^{\frac{1}{2}} p_a^{1/2\gamma}\left(p_b^{(\gamma-1)/2\gamma} - p_a^{(\gamma-1)/2\gamma}\right) \tag{3.8}$$

where $\mu^2 = \frac{\gamma-1}{\gamma+1}$ and the plus sign is taken for right-facing waves and the minus sign is taken for left facing waves. Using the Hugoniot equation and the Rankine-Hugoniot jump equations for a shock wave, the relation across a shock is defined as:

$$u_b = u_a \pm (p_b - p_a)\sqrt{\frac{(1-\mu^2)\,(1/\rho_a)}{p_b + \mu^2 p_a}}. \tag{3.9}$$

These equations describe the locus of fluid states b that can be reached from fluid state a across shock and rarefaction waves. The initial state between the rarefaction wave and shock (state 0) can be triangulated by determining where the locus of states across a rarefaction wave from state R intersects with the locus of states across a shock

wave from state L. For clarity, the locus of possible states that can be reached by either rarefaction wave or shock wave from an initial state defined on the left (state L) is plotted in Figure 3.12. The plotted curves represent the states possible to be reached by a shock and the states possible to be reached from a rarefaction when the wave is defined by state L. In this case, state L is characterized by zero particle velocity and a pressure of 1×10^8 Pa.

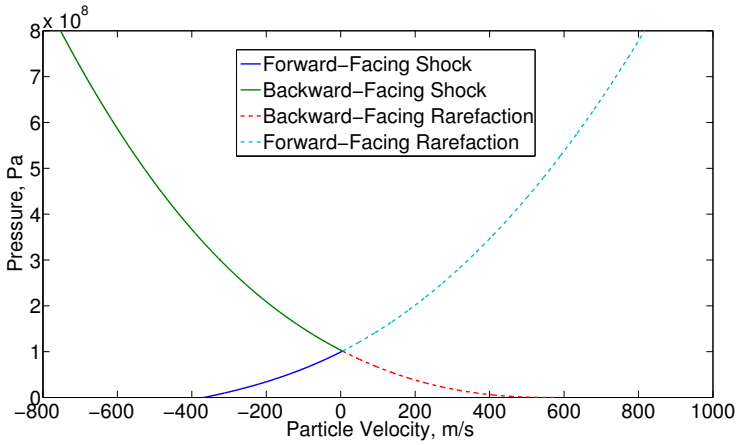

Figure 3.12: Typical P-u Diagram

By plotting these loci with those produced using state R (in Figure 3.13), the initial intermediary state between the shock wave and the rarefaction wave can be determined. The intersection of the forward-facing shock arm of the state defined on the left and the forward-facing rarefaction arm of the state defined on the right determines the initial state. When the shock passes the rarefaction, the intersection between the backward-facing rarefaction arm of the state defined on the left and the forward-facing shock arm of the state defined on the right is found iteratively using the state loci again. This new intersection defines the new intermediate state between the new rarefaction and shock wave. The equation that is solved to find the

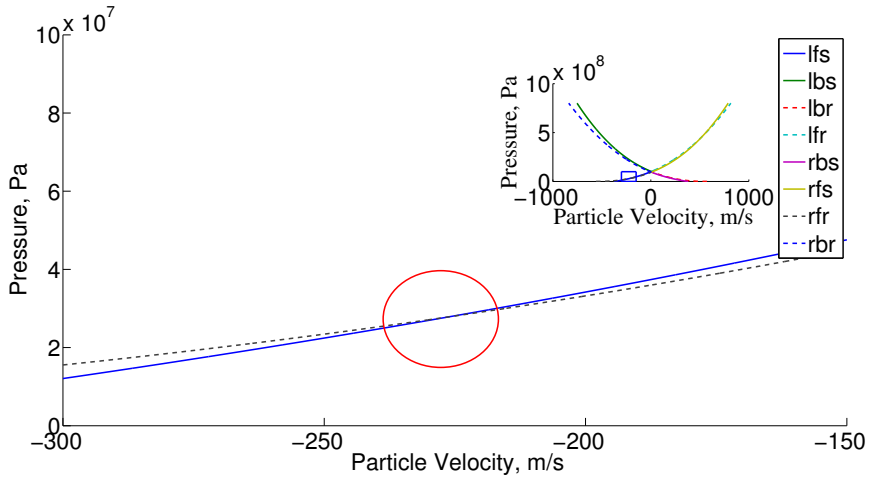

Figure 3.13: Typical P-u Diagram for the Interaction of Two Waves

new intermediate state 3 is:

$$-\left(\frac{p_0}{p_r}\right)^{\beta}\left(\frac{p_l}{p_0}-1\right)\sqrt{\frac{2}{\gamma\left(\gamma-1\right)\left[1+\alpha\left(\frac{p_l}{p_0}\right)\right]}}+\frac{2}{\gamma-1}\left[1-\left(\frac{p_0}{p_r}\right)^{\beta}\right]+$$
$$\left(\frac{p_3}{p_r}-1\right)\sqrt{\frac{2}{\gamma\left(\gamma-1\right)\left[1+\alpha\left(\frac{p_3}{p_r}\right)\right]}}-\frac{c_l}{c_r}\frac{2}{\gamma-1}\left[1-\left(\frac{p_3}{p_l}\right)^{\beta}\right]=0 \tag{3.10}$$

where $\alpha=\frac{\gamma+1}{\gamma-1}$ and $\beta=\frac{\gamma-1}{2\gamma}$ following the notation of Bremner et al. (*Bremner et al.*, 1960). In Equation 3.10, p_3 is the only unknown. The functional form equivalent Tait equation has been applied to this problem for the first time, applying the conservation equations described above to problems in the liquid domain.

For the magnitude of shock and rarefaction waves that are present in the wave train generated by the multiple-source array, all interactions that occur between shocks and rarefactions yield reflected rarefaction waves of negligible strength (when the interactions are computed for the shock tube model). CFD simulations, however, demonstrate that rarefaction waves continue to exist and propagate forward post-interaction, not backward as seen in the shock tube depicted in Figure 3.11. The actual post-interaction wave train seen in numerical examples is akin to the shock

tube setup shown in Figure 3.14. The method used to calculate the final intermediate state when oppositely-propagating waves result from shock-rarefaction interactions cannot be used for the instance when the resulting waves propagate in the same direction. Figure 3.14 illustrates this point. Although the wave types are known, and

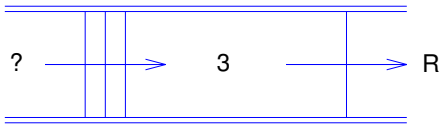

Figure 3.14: Shock Tube Diagram - After Interaction

therefore the conservation relations across each wave are known, the state on the left is now unknown because it is being acted upon by the rarefaction wave. The system of equations, therefore, is no longer closed. A heuristic method has been formulated to capture interaction phenomena in the analytical model. Accurate characterization of shock-rarefaction interactions remains a prime topic for further study.

3.4 Chapter Summary

Three important multiple-source effects have been identified in this chapter. The generation and propagation of rarefaction waves critically alters the pressure waveform at the target through accelerated decay at the waveform tail. The Riemann problem for a gas-liquid interface has been solved to characterize the initial magnitude of rarefaction waves. Rarefaction wave propagation speed is calculated quite differently than the approach used for shock propagation speed because rarefaction waves are simple waves: no discontinuous jumps are present. Conservation equations across a rarefaction wave, therefore, are much different than the Rankine-Hugoniot jump conditions. Acoustic models for spatial decay have proven to be reasonable approximations for rarefaction decay and have been included in the physics based reduced-order model.

Shock coalescence presents another significant deviation from superposition results and has been implemented using the shock propagation speed calculation described in Chapter II. To the author's knowledge, the coalescence problem has not been solved previously to predict the rate of coalescence analytically. Furthermore, superposition techniques used by existing coalescence methods to predict the magnitude of the coalesced wave neglect important interaction phenomena that lead to attenuation. The implementation of specific coalescence modeling techniques will be described in the following chapter.

Lastly, shock-rarefaction interactions were introduced and analyzed. The shock tube is used as an inspiration for the modeling techniques employed in the reduced-order model, as it describes attenuation that must be accounted for when predicting the pressure pulse at the target. Because the physics governing the multiple-source array differ slightly from the shock tube model, a heuristic method has been developed and included in the analytical model to represent the effects of shock-rarefaction interaction.

CHAPTER IV

A Physics-Based Reduced Order Model for the Multiple-Source Explosive Array

Methods for modeling shock waves generated by spherical explosive sources have been developed in previous chapters. Rarefaction waves are also produced by the multiple-source explosive array and have been explored. The propagation of each wave type and their subsequent interaction has been examined. In this chapter, individual elements of the analytical model will be synthesized into a comprehensive unit that can be used to accurately simulate the array at a significant computational savings when compared to existing CFD tools. To begin, the centerline framework is introduced.

4.1 The Centerline Piecewise-Analytical Model

A framework has been devised to model the interactions of the shock waves and rarefaction waves produced by the multiple-source array. The structure of the centerline piecewise-analytical model is shown in Figure 4.1. The method is best described as a piecewise-analytical model because a set of analytical equations is evaluated at each computational step. The process is as follows:

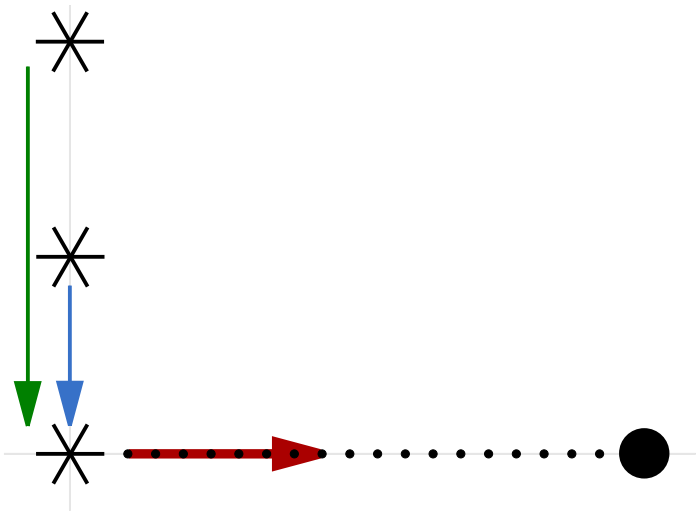

Figure 4.1: Centerline Piecewise-Analytical Model

1. A line perpendicular to the plane of the array (or perpendicular to the coaxial line of the array, if a line array is being used instead of a grid array) is drawn from the target point to the array plane. This is referred to as the *centerline*, or the computational path on which wave propagation and interaction is tracked. The centerline is represented in Figure 4.1 by the black dotted line. The point of intersection shared by the array plane and the centerline is called the *starting point*.

2. Each shock is propagated to the starting point from its source as though it is propagating through an undisturbed fluid. Individual wave propagation to the starting point is represented by the green and blue arrows in Figure 4.1. The detonation time for each respective source is added to shock arrival time at the starting point to calculate an initial arrival time for each shock wave.

3. As each charge detonates, the resulting explosive gas bubble becomes a candidate for a shock collision. The first shock to arrive at the bubble surface after the bubble is conceived reflects off of the bubble and creates a rarefaction wave.

4. Once they are created, rarefaction waves propagate to the starting point through fluid pressurized by a single shock wave, because rarefaction waves always travel behind at least one shock. Spreading is neglected until the rarefaction wave reaches the starting point. Therefore, the head and tail of each respective rarefaction wave arrive at the top of the centerline simultaneously.

5. Once the starting point arrival time of each wave has been computed, an initial order is established at the starting point.

6. The leading wave now propagates into undisturbed fluid along the centerline, which has been discretized into small spatial segments. When the first wave reaches the end of the first computational segment, the arrival time is recorded. The second wave travels in the wake of the first wave, the third wave travels in the wake of the first two waves, and so on.

7. The wave train continues from one spatial segment to the next (hence the "piecewise" label) and the order of waves is reevaluated at each new segment. The collective propagation of shock and rarefaction waves is represented by the red arrow in Figure 4.1. Once the new order has been established, the new first wave travels into undisturbed water, the new second wave travels in the wake of the new first wave, and so on until the wave train reaches the target.

4.2 Computational Implementation

The modeling techniques used to characterize the fluid at each computational segment are explained in this section. Specific implementation approaches and heuristic methods are described in detail to build on the theoretical foundation laid in Chapter III.

4.2.1 Single Shock Pressure

The pressure contribution from a single shock is calculated using weak shock theory. Pressure histories produced by the CFD tool are used to initialize the pressure wave. The original pressure histories are taken not only at the source, but at varied standoffs (referred to as *waypoints*) so that the wave profile can be recalibrated as it propagates toward the target. The advantage of recalibration can be seen in Figure 4.2. In this case, the advantage of added waypoints is slight, but discernible, as the curve representing the analytical model with more waypoints correlates better with CFD results than the curve representing the analytical model with less waypoints.

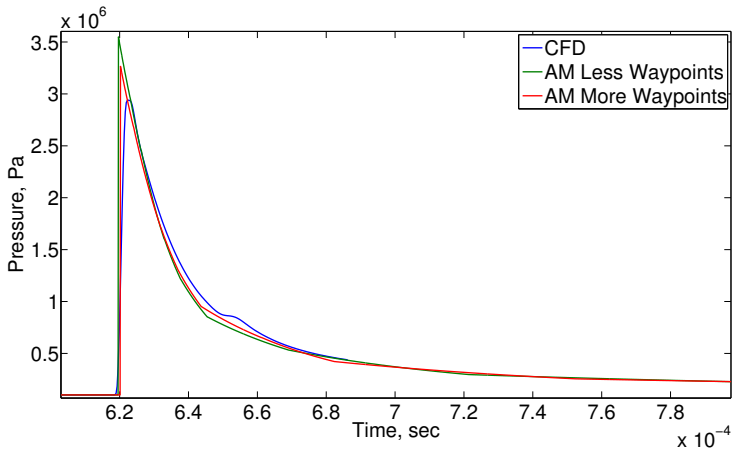

Figure 4.2: Weak Shock Waypoint Comparison, 95 cm Standoff

Waypoint frequency and location is somewhat unique to each charge weight. The number of weak shock segments required to characterize an original history at each waypoint is also dependent on the charge weight, in that the profile of the shock wave (its steepness and breadth) is a function of charge weight. When larger charges are used, peak magnitude increases along with the proportions of the waveform profile. The number of segments n used at each waypoint and the location of each waypoint is enumerated in Table 4.1 for 1 g sources. Waypoints used to characterize shock waves from 1 lb sources are listed in Table 4.2. Each segment represents a unique exponential curve fit to a specific region of the shock waveform at that waypoint.

Waypoint Radius (cm)	1	10	50	100
Weak Shock Segments	10	10	10	10

Table 4.1: 1 g Spherical Charge Weak Shock Theory Waypoints

Waypoint Radius (cm)	8	10	20	50	80	400	800
Weak Shock Segments	8	8	8	8	8	8	8

Table 4.2: 1 lb Spherical Charge Weak Shock Theory Waypoints

Sample weak shock segments are shown for the 1 cm waypoint for a 1 g spherical charge in Figures 4.3 and 4.4

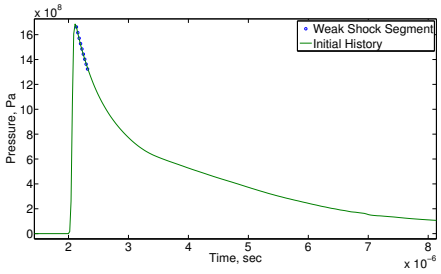

Figure 4.3: Weak Shock Near-Field History Fit, Segment 1

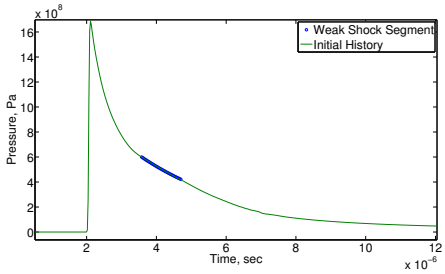

Figure 4.4: Weak Shock Near-Field History Fit, Segment 5

When evaluating the magnitude of a shock wave using weak shock theory, both the radius from the charge center and the retarded time are necessary. Retarded time is the time elapsed after a shock peak has arrived at a point some location, and is defined for an acoustic wave as:

$$t_{ret} = t - x/c_o. \tag{4.1}$$

The exact location of a trailing wave on a preceding shock tail can be triangulated given radius and retarded time. This information is used to predict the overpressure produced by the leading shock at the time the trailing shock reaches that coordinate.

4.2.2 Single Shock Speed

The propagation speed of weak shock waves is a function of two properties. Sound speed is a factor, as is particle velocity in the preceding fluid and the particle velocity behind the shock front. The sound speed used here is calculated as the isentropic sound speed determined by the Tillotson equation. Internal energy terms in the Tillotson equation are neglected because they are insignificant compared with pressure and density terms, so that sound speed is a function of pressure and density exclusively. When a particular shock wave reaches a discrete increment on the computational line, the leading shocks are identified. The time of arrival for the shock of interest is used to establish the retarded time for each preceding wave, and the radii to each respective source are known based on the spatial increment. The pressure of preceding shock and rarefaction waves is superposed to define the fluid pressure experienced by a trailing wave. The Tait equation is used to estimate fluid gotcha based on the calculated pressure, and the resulting pressure-density pair is used to calculate the isentropic sound speed in the fluid with the isentropic sounds speed equation derived from the Tillotson equation of state.

Certain important interactions are modified as the analytical model distills complex interaction phenomena onto a single computational line. One such effect is the pressure magnitude of leading waves. At far standoffs, where the shock waves are close to one another on the computational line, using the retarded time is a good representation of the effect of leading shocks. In the near-field however, shock waves interact *even before* they reach the computational line; without modeling this near-field contribution, the analytically modeled shock waves arrive late. To remedy this, near-field pressure from preceding waves has been assumed to be at the maximum; that is, a retarded time of zero is used to assess the strength of each preceding shock in the near-field (six charge spacings). Particle velocity effects are less influential and difficult to predict in the near-field. As a result, retarded time is used to assess the

particle velocity contribution of leading waves in both the near and far field. Unlike pressure, the particle velocity attributed to leading shock waves acts in a direction. Only the vector component of particle velocity along the computational line, therefore, is considered for the leading shocks and shock of interest as propagation speed along the computational line is calculated.

4.2.3 Superposition

Exploration of underwater shock interactions using the CFD code has led to the conclusion that shock pressures can be superposed. Superposition includes overpressure caused by a shock wave and the relaxation of pressure in the wake of a rarefaction wave. Superposition appears in two settings within the analytical model. It is used to determine the fluid state ahead of a certain wave when calculating the propagation speed of said wave. In the case of pressure, superposition of the peak values is used, as noted above. Second, the pressure history at the target is comprised of the sum of shock wave and rarefaction wave pressures, along with their respective arrival times.

4.2.4 Shock Coalescence

Existing spherical shock coalescence modeling methods address the magnitude of the coalesced wave, but not the spatial rate of coalescence. Coalescence is modeled in the analytical model by noting the propensity for shock waves in the far field to merge when a trailing wave catches up to a leading wave. The coalescence methodology implemented in the analytical model is called the cow-catcher method. Much like the devices affixed the front of 19th century steam locomotives, this coalescence modeling approach enables strong trailing waves to 'scoop up' slower leading waves along the computational line. The cow-catcher method is active for all portions of the computational line except the extreme near-field ($<$ one charge spacing).

Research on mach stem formation inspired the coalescence approach applied in

the reduced-order model. The formation of a mach stem between two symmetrical spherical shock waves in air is shown in Figure 4.5. The developed flow depicted in the rightmost image shows the coalescence behavior exhibited by two shock waves. Instead of two distinct waves in the vicinity of the intersection, the tails just aft of the intersection point have been accelerated and have coalesced with the leading waves. Although the shock tails are accelerated as they travel behind the respective

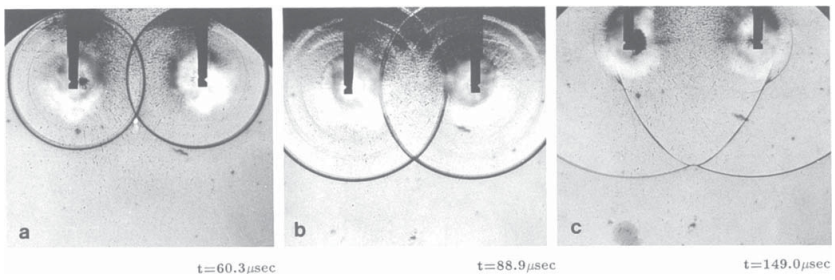

Fig. 3a-c. A sequence of schlieren photographs of a pair of weak symmetrical blast waves with 0.1 mm copper wires

Figure 4.5: Formation of Mach Stem for Symmetric Spherical Shocks (*Higashino et al.*, 1991)

fronts, they do not overtake the fronts. The tails and fronts coalesce in the region of the intersection. This behavior is replicated by the cow-catcher method. Similar interaction can be seen for the asymmetric case, depicted in Figure 4.6.

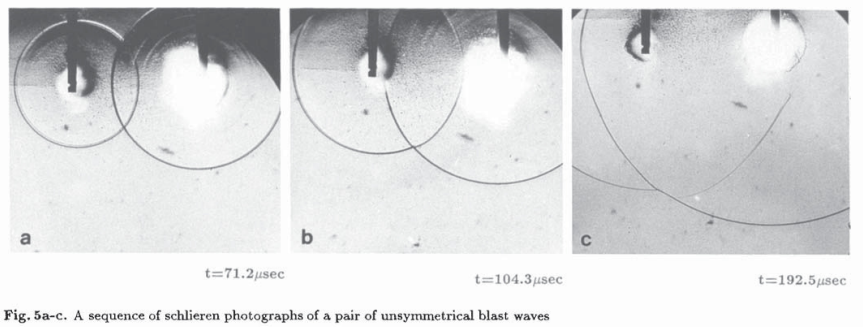

Fig. 5a-c. A sequence of schlieren photographs of a pair of unsymmetrical blast waves

Figure 4.6: Formation of Mach Stem for Asymmetric Spherical Shocks (*Higashino et al.*, 1991)

The asymmetrical case is a microcosm of the wave interactions present in the multiple-source explosive array. In the rightmost frame of Figure 4.6, the shock wave

on the left is 'stronger' at the interaction point than the shock on the right because the left shock is closest to its source. Despite the fact that it is stronger (and, therefore, faster) than the larger shock, the tail from the left shock does not overtake the front, but merges with it. Coalescence of waves with different strengths upholds the cow-catcher method as a reasonable approach to modeling shock coalescence for both symmetrical and asymmetrical shock intersections.

4.2.5 Rarefaction Waves

Rarefaction waves play a critical role in the analytical model. They reduce pressure along the computational line, slowing waves behind them. Rarefaction waves also interact with shock waves leading to mutual attenuation. Pressure reduction from shock-rarefaction interactions must be factored into array optimization in order to accurately predict the pressure history at the target.

The initial strength of a rarefaction wave is a function of the fluid state on both sides of the explosive gas bubble that initially reflects the rarefaction. Bubble expansion rate and the fluid state within the bubble is codified in a lookup table comprised of results from numerical experiments. The lookup table is appropriate because of the negligible effect that shock collisions have on explosive gas bubbles in the millisecond time scale that is relevant for the analytical model. It is possible, therefore, to simply simulate the bubble using the CFD tool; data collected in this case will bear a close resemblance to the actual state of a bubble in the midst of other shocks. The explosive gas bubble of a particular charge becomes a candidate for shock collisions in the instant after the particular charge is detonated. The first shock to collide with the bubble is identified, and an iterative process commences to determine the true bubble radius and, hence, the shock radius, when the collision occurs. This information is used to calculate the exact parameters of the collision (the state on the liquid and gas sides of the interface) and thus the best possible representation of the initial

rarefaction strength at the bubble surface.

Rarefaction waves are assumed to decay in similar fashion to spherical acoustic waves. Spherical acoustic wave spatial decay can be derived from the conservation of energy across the spherical wave front. Since the energy contained in a spherical simple wave at radius R_o is the same as the energy at some larger radius R, the conservation of energy gives us (*Medwin and Clay*, 1997):

$$4\pi i_R R^2 \left(\delta t\right) = 4\pi i_o R_o^2 \left(\delta t\right) \tag{4.2}$$

for a pulse duration δt where i is the intensity, or the sound power per unit area. Solving for intensity at the larger radius yields:

$$i_R = \frac{i_o R_o^2}{R^2}. \tag{4.3}$$

Therefore, intensity decays as $1/R^2$ for a spherical acoustic wave. Because sound intensity is proportional to the square of sound pressure, the spatial pressure decay for a spherical simple wave is proportional to $1/R$.

The center coordinate to determine R must be established for rarefaction waves. After it has propagated for a small distance, the rarefaction wave produced by a shock-bubble collision is approximately concentric with the initial explosive charge. This behavior has inspired the use of the explosive gas bubble radius at the point of the collision as the initial radius of the rarefaction wave for spatial decay purposes. Rarefaction wave radius, therefore, is measured from the center of the charge that caused the bubble that produced said rarefaction.

Rarefaction waves are so-called 'simple waves', meaning no discontinuous jumps are present. Simple waves travel at the acoustic speed of the fluid into which they propagate. Acoustic speed is defined in Equation 2.19 on page 26. Once the pressure contributions of waves ahead of a particular rarefaction wave are calculated at some

spatial coordinate along the computational line in the analytical model, acoustic speed is calculated using the superposition particle velocity, superposition pressure, the Tait-approximated density based on the superposition pressure, and the isentropic sound speed from the Tillotson equation. The head of the rarefaction wave travels into fluid of a different state than what the tail sees, because the fluid is relaxed as the rarefaction wave propagates through it. The head of the rarefaction wave, therefore, is assumed to propagate at the sound speed dictated by the initial superposition pressure, density, and particle velocity. Rarefaction tails are assumed to propagate at the sound speed dictated by the initial superposition pressure minus the rarefaction strength. Any superposed particle velocity ahead of the rarefaction tail is assumed to have been nullified, so the rarefaction tail travels at the acoustic speed with $u = 0$, also known as the sound speed of the relaxed fluid. The gradient from the high pressure rarefaction head to the low pressure rarefaction tail is assumed to be linear and is modeled in such fashion.

4.2.6 Interaction

Shock-rarefaction interactions play a significant role in the attenuation of shock waves as they propagate to the target point. The theoretical developments described in Chapter III provide a framework for solving the case where interaction results in two waves propagating away from one another. All CFD simulations, however, predict two waves propagating in the same direction post-interaction. This scenario cannot be solved by the existing theoretical framework because the system of governing equations becomes open in this instance. Given the goal of the present research effort (development of a physics-based, reduced-order model), a heuristic method has been devised.

When shock waves produced by the multiple-source array overtake rarefaction waves produced by the array, theory predicts the rarefaction wave is all but extin-

guished (the rarefaction wave that is reflected post-interaction is extremely weak). In this case, the percent reduction of peak pressure experienced by the shock as a result of interaction with the rarefaction wave can be defined as:

$$penalty = \frac{p_{rare}}{p_L - p_R + p_{rare}} \tag{4.4}$$

where p_{rare} is the strength of the rarefaction wave prior to the interaction, p_L is the pressure behind the shock before it overtakes the rarefaction wave, and p_R is the pressure ahead of the rarefaction wave before it is overtaken. Since the theoretical solution indicates that the rarefaction wave ceases to exist, rarefaction waves that have interacted with shock waves become 'invisible' for purposes of interaction after the first interaction in the analytical model. Therefore, one shock may interact with several rarefaction waves, but one rarefaction may only interact with one shock. The penalty applied to the shock wave is also applied to the rarefaction, because theory demonstrates that both waves are attenuated as a result of the interaction.

A shock may interact with several rarefaction waves as it propagates to the target point. Interaction penalties are applied to the shock overpressure in the following manner:

$$p_T = p_o \left(1 - penalty_1\right) \left(1 - penalty_2\right) \left(1 - penalty_3\right) ... \tag{4.5}$$

with p_T being the pressure experienced at the target from the shock of interest and p_o being the predicted peak pressure value of that shock wave at the target as predicted by weak shock theory (essentially the non-interaction pressure). Penalties are applied to each shock wave as they propagate, and are factored in when determining the fluid state experienced by following waves on the computational line because preceding superposition pressure calculations include these penalties. When the pressure history at the target is constructed, penalties are not used to scale the entire wave, rather, the penalty acts as a pressure ceiling defining the maximum pressure

magnitude contributed by the penalized wave at the target. Penalty implementation is demonstrated graphically in Figure 4.7. CFD simulations show that shock waves that have undergone deleterious interaction effects are broadened at the peak, which further establishes the penalty application approach as a reasonable method for the reduced-order model.

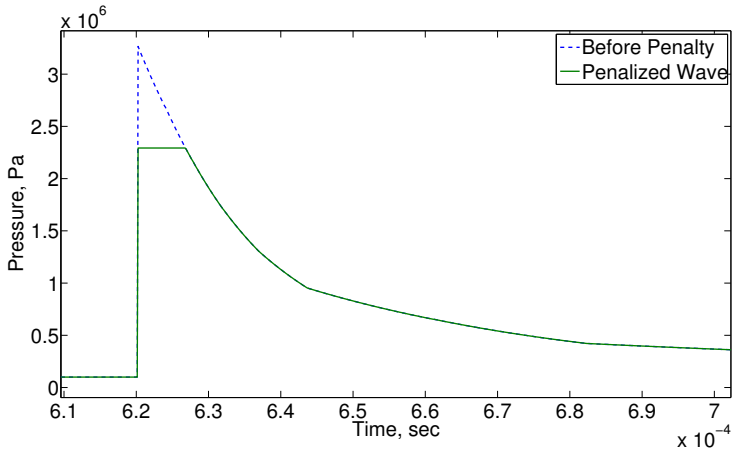

Figure 4.7: Interaction Penalty Implementation

4.2.7 Bulk Cavitation

The multiple-source explosive array will be deployed below the surface of the ocean. The depth of deployment must be considered, as it plays a critical role in the ability of the array to transmit strong shock waves in the direction of the target. Rarefaction waves resulting from shock-bubble collisions have been addressed previously. It is important to account for the effects of rarefaction waves originating from the surface as well. The most critical free surface effect, in terms of the multiple-source array, is bulk cavitation.

Bulk cavitation has been studied in fields as diverse as ship shock analysis and marine wildlife conservation (*Christian*, 1973; *Zong et al.*, 2012). This phenomena is relevant to ship shock applications because the collapse of the bulk cavitation region can result in a second shock wave that impacts the structure. Bulk cavitation is

important for marine wildlife conservation because the near-zero pressures caused by a rarefaction wave near the surface cause the swimbladders of certain fish to fatally overextend. This tragic reality highlights the physical phenomena responsible for bulk cavitation. When the shock generated by a single spherical source reaches the free surface, the reflected rarefaction wave, in certain instances, can be strong enough to reduce pressure in the fluid it travels through to the vapor pressure of water. In those cases, water near the surface is ripped apart. This is why vapor pressure, or cavitation pressure, is sometimes referred to as the 'breaking pressure' of water. Rarefaction waves created from shock-bubble collisions in the array occur in a highly pressurized region. Due to significant local pressure, the rarefaction waves never reduce the total overpressure below the hydrostatic value or, if they do, it is for a short time duration. This interpretation is corroborated by CFD data which correlates well with analytical solutions that ignore cavitation.

Empirical methods have been derived to estimate the region where bulk cavitation is likely to occur after an underwater explosion (*Malone*, 2000). The upper boundary of the bulk cavitation zone is a function of atmospheric pressure, hydrostatic pressure, shock strength, and rarefaction strength. The lower boundary is a function of the decay rates of the shock and rarefaction wave respectively. Where the shock wave has weakened such that the rarefaction wave reduces the absolute pressure in the water to the cavitation pressure, bulk cavitation will occur. The bulk cavitation regions created by a single 1 g and 1 lb spherical explosive source (of TNT) have been identified using the model outlined by Malone. Figure 4.8 shows the 1 g charge case and Figure 4.9 depicts the 1 lb result.

The plotted bulk cavitation regions are axisymmetric about the vertical axis. The 1 g case, for a 1 m charge depth, exhibits a bulk cavitation zone that is never deeper than 0.5 m. It is concluded, therefore, that placing a multiple-source array of 1 g charges at a 1 m depth should be sufficient to avoid any interaction between the array

and the target of shock waves with the cavitated region. The 1 lb charge creates a much larger bulk cavitation zone, even at a depth of 3 m. Although the cavitated region extends below the charge depth, the non-cavitated region has a radius of 10 m at a 3 m depth. The array will be less than 20 m wide (as a constraint); as such, bulk cavitation effects can be neglected when the array is deployed at a minimum depth of 3 m.

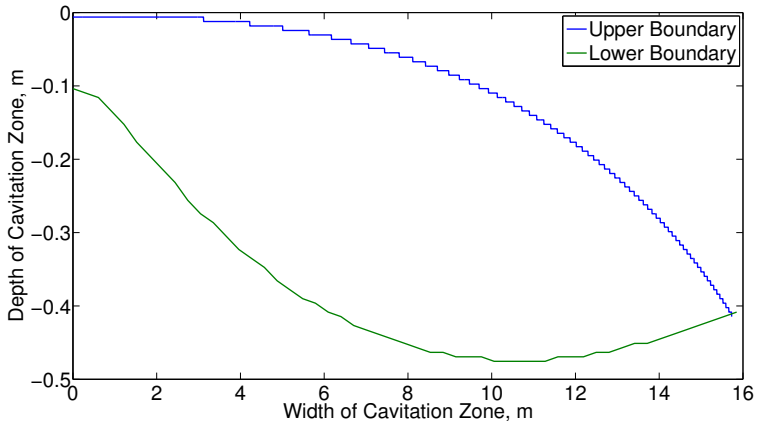

Figure 4.8: Bulk Cavitation Zone, 1 g Charge, 1 m Depth

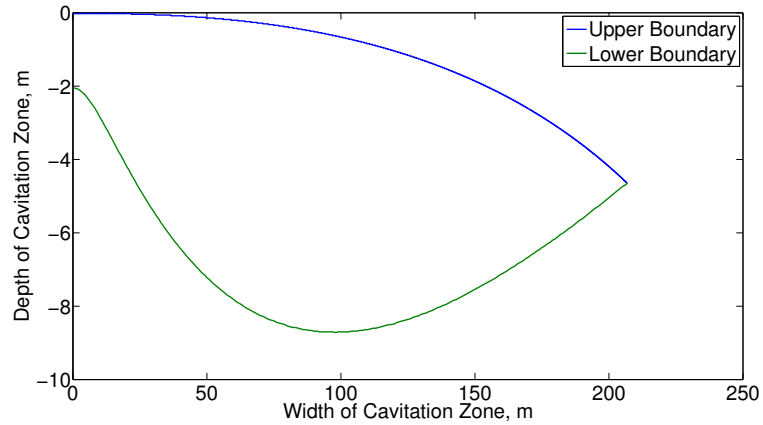

Figure 4.9: Bulk Cavitation Zone, 1 lb Charge, 3 m Depth

4.3 1 g Charges

Arrays comprised of spherical 1 g charges were simulated using CFD and compared to analytical model predictions. Shock waves produced by a single 1 g source have been studied in terms of magnitude, peak pressure, and impulse (the integral of pressure over time) in Chapter III. Correlations between numerical and analytical results were very strong for single sources out to standoff ranges in excess of 30 m. This section will compare numerical and analytical results for two line array configurations. Modeling two-dimensional arrays and the associated difficulties will also be discussed.

4.3.1 Line Arrays

Two 1 g charge line array configurations were studied to validate the analytical model. A line array is arranged such that the explosive charges share a common axis. The charge spacing used in both instances is 10 cm. At smaller radii, nonlinear near-field interactions dominate local flow characteristics and result in significant shock attenuation. The 10 cm spacing is a threshold of sorts, and is the approximate minimum spacing that can be used for 1 g sources to avoid highly-nonlinear deleterious near-field effects. Charges have been spaced as closely as possible in order to maximize the peak pressure generated by the array. The first configuration examined below is a five charge line array.

4.3.1.1 Five Charge Line Array

A line array comprised of five 1 g TNT sources has been simulated with the CFD tool to validate the analytical model. The array setup can be seen in Figure 4.10. All numerical results are computed for an infinite fluid with ambient pressure set to 100 kPa and ambient density set to 1000 kg/m^3. Perfectly reflective boundary conditions are used and the computational domain size has been selected for each case so that reflections from the boundaries arrive significantly later than the waveform

of interest and, therefore, do not contaminate the results. Charges are detonated simultaneously for the five charge line array test case, and pressure histories have been simulated at standoffs of 10 cm increments below the center charge. It is critical to note that the numerical computation used to validate the analytical model lasted for *6 hours* on six processors. The analytical model results were generated in *15 seconds* on a single processor. The disparity of computational time illustrates the necessity of a physics based reduced-order model for optimization analysis of the multiple-source explosive array.

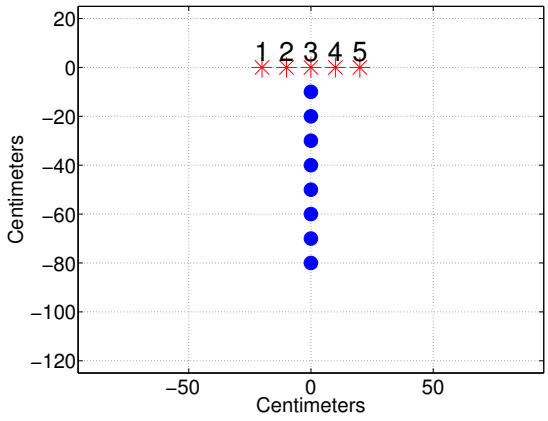

Figure 4.10: Five 1 g Charge Line Array Setup

The 10 cm standoff result, shown in Figure 4.11, is especially enlightening. Three distinct peaks can be seen due to the symmetry of the charge configuration and the detonation timing. Arrival time of each peak is determined correctly, indicating that the propagation speed modeling techniques are sufficient at near-field standoffs for 1 g charges. The arrival of two rarefaction waves can be clearly seen with the first at approximately $1{\times}10^{-4}$ seconds and the second shortly thereafter. The magnitude of both the shock peaks and rarefaction troughs is estimated correctly as well. The 10 cm standoff results are proof that the methods used to predict overpressure (weak shock theory, rarefaction strength from the Riemann solution at a gas-water interface, and superposition) are sufficient for a five charge array in the near-field.

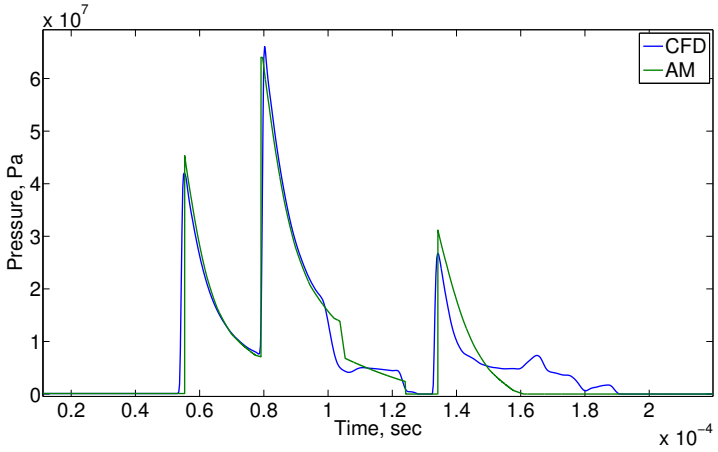

Figure 4.11: Five 1 g Charge Line Array Centerline Pressure History, 10 cm Charge Spacing, 10 cm Standoff

Analytical and numerical predictions for the next standoff, 20 cm away from the center charge, are shown in Figure 4.12. The peak prediction and decay of the first wave is predictably good. The first peak is created by the middle charge and, therefore, is essentially the case of a single spherical shock traveling into an undisturbed fluid. The capability of the analytical model has been proven in this situation. The prediction of the second peak magnitude is also close to the numerical result, demonstrating superposition as an effective modeling approach. It should be noted that sharpness of the shock peaks in numerical results is correlated to the density of the computational mesh used for the numerical simulation. Even the finest mesh that discretizes the fluid domain into minuscule elements will round the peaks to some extent because the peaks are so sharp. Therefore, peak amplitude seen in CFD simulations will always be reduced from the actual peak value, to some extent. The coarser the mesh, the greater the rounding effect becomes. Not all peak rounding is due to numerical nuance, but the second peak in Figure 4.12 most likely exhibits this behavior. The analytical model is also slightly overpredicting the propagation speed of the second wave, leading to a small overprediction of peak pressure when waves are superposed.

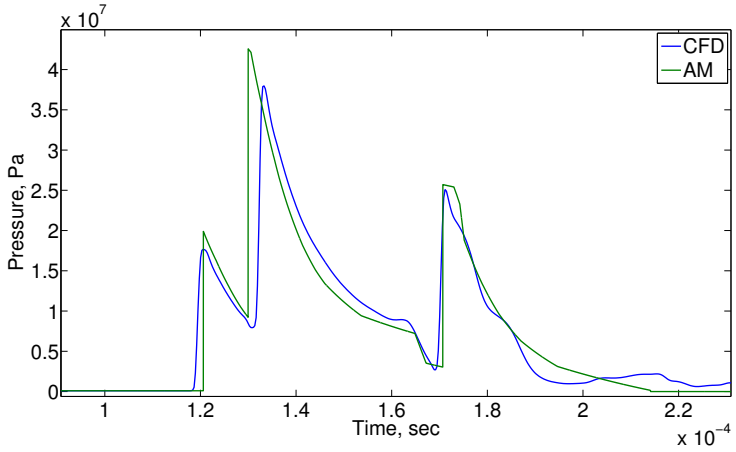

Figure 4.12: Five 1 g Charge Line Array Centerline Pressure History, 10 cm Charge Spacing, 20 cm Standoff

The two most exciting characteristics of the 20 cm standoff result are the prediction of the rarefaction notch and the shock penalty that is visibly influencing the third peak. The arrival time, magnitude, and duration of the rarefaction waves following the second peak are predicted perfectly, further validating the rarefaction wave model in the near-field. The penalty method also yields promising results. The peak magnitude is predicted correctly and the broadening of the third peak can also be seen (for comparison, examine the sharper third peak in the numerical results shown in Figure 4.11). It is the author's opinion that the heuristic method used to model shock-rarefaction interactions performs best for single interactions. Subsequent interactions are predicted with reasonable accuracy for a reduced-order model, but this topic is certainly a significant opportunity for future work.

Results for the intermediate standoffs are shown in Appendix A. Far-field results for standoffs of 70 and 80 cm are depicted in Figures 4.13 and 4.14 respectively. These figures show that the rate of coalescence predicted by the analytical model is close to the numerical result. The penalty assigned to the third peak from the earlier interaction ensures that the magnitude of the second coalesced peak in Figures 4.13 and 4.14 (to which the original third peak contributes) is not overpredicted at the

far-field standoffs. The rarefaction waves arrive at the correct time, duplicating the knuckle seen in the tail of the pressure pulse from the numerical model. Although the rarefaction waves seem to oscillate around the correct solution, the averaged trend is correct.

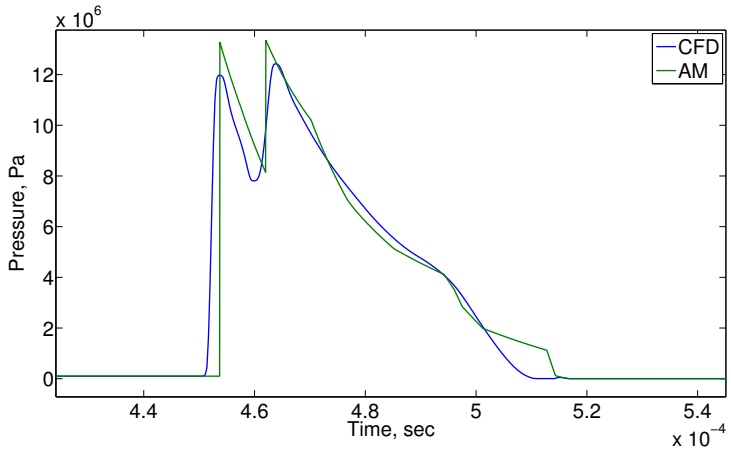

Figure 4.13: Five 1 g Charge Line Array Centerline Pressure History, 10 cm Charge Spacing, 70 cm Standoff

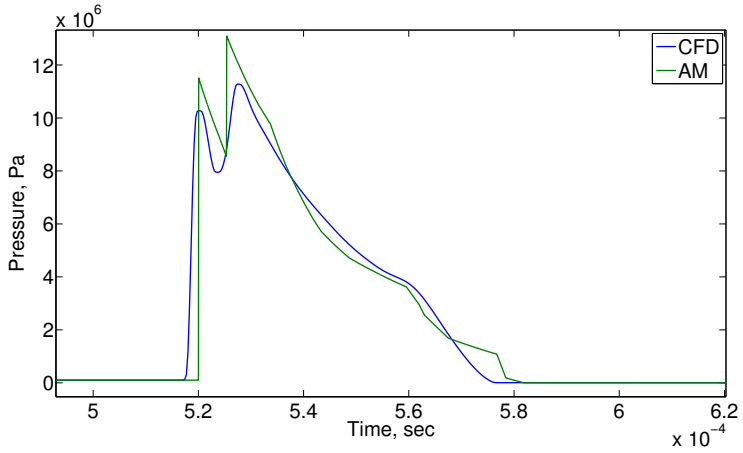

Figure 4.14: Five 1 g Charge Line Array Centerline Pressure History, 10 cm Charge Spacing, 80 cm Standoff

To demonstrate the importance of the models for nonlinear propagation speed, coalescence, rarefaction waves, and shock-rarefaction interaction that have been developed as part of this research effort, the prediction from a linear analytical model at the 80 cm standoff is shown in Figure 4.15. Weak shock theory was used to gener-

ate the shock amplitude and decay for the linear model, shock waves were assumed to propagate at the sound speed in the fluid, and rarefaction waves were neglected altogether. This setup mimics the state of the art for analytical underwater explosion models existing prior to the present research effort. The poor correlation is expected, as the multiple-source array produces complex flow fields that must be modeled with sophisticated means, even in a reduced-order form.

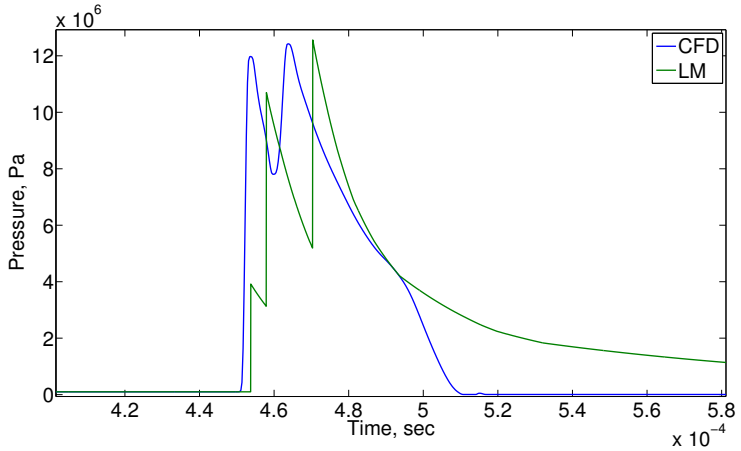

Figure 4.15: Five 1 g Charge Line Array Centerline Pressure History, 10 cm Charge Spacing, 80 cm Standoff - Linear Model

4.3.1.2 Twenty Charge Line Array

A twenty source line array with 1 g charges was also simulated using the CFD tool. The array was similarly arranged with 10 cm charge spacing, but the target point was placed 4 m out from the array center. Simultaneous and 'focused' timing schemes were analyzed. The simultaneous case is compared with numerical results in Figure 4.16. The wave field produced by the twenty charge array is obviously much more complex than the five charge array. Nonetheless, the troughs predicted by the analytical model roughly trace the spine of the numerical waveform and the pulse width correlates very closely. It should be emphasized that the numerical results were computed on a supercomputer with *100 processors* working for *196 hours*. The reduced-order mode

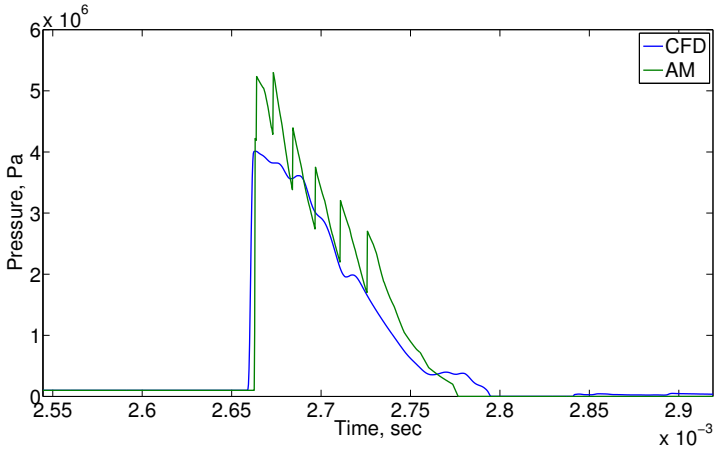

Figure 4.16: Twenty 1 g Charge Line Array Centerline Pressure History, 10 cm Charge Spacing, 400 cm Standoff

produced the waveform seen in Figure 4.16 in *80 seconds* on a *single processor*. Given the required computational time for the CFD results, optimization would be infeasible if the numerical tool was used to predict the behavior of the twenty source array; the analysis would take months to complete.

A focused timing scheme was also explored. The distance between the target and each respective charge was used to determine an approximate time of arrival for each shock. The estimated arrival times were used to specify the detonation timing of each charge, with the outer charges being detonated first in an attempt to have each wave arrive at the target simultaneously. The resulting waveform is plotted in Figure 4.17. The peak pressure and decay profile are captured quite well by the analytical model. The interaction penalty model, with some refinement, may enable an even better prediction of the waveform generated by the twenty charge array. One final observation is important to note regarding large arrays. The analytical model predicts shock propagation speed and coalescence with a high degree of accuracy for the five charge array at all standoffs. In the twenty charge case, the analytical model successfully predicts *when shock waves coalesce and when they do not*. Accurate coalescence rate predictions are a critical component of the analytical model. Without

this capability, the analytical model and the CFD code would give different results for the same detonation timing scheme.

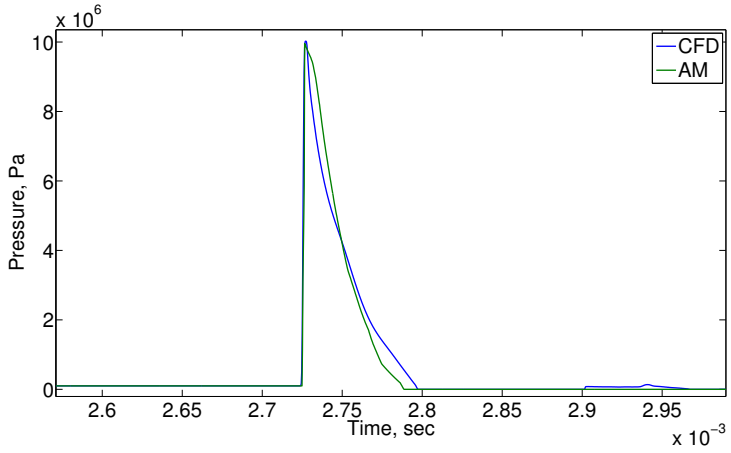

Figure 4.17: Twenty 1 g Charge Line Array Centerline Pressure History, 10 cm Charge Spacing, 400 cm Standoff

4.3.2 Grid Array

The line array examples illuminate the capability of the reduced-order model to capture important shock phenomena. The proposed design for the multiple-source array is a grid, however. While the analytical model is able to generate pressure histories for line arrays and grid arrays alike, numerical tools are more limited. Line arrays are simulated in two-dimensional computational meshes, since the charges are spherical and, hence, axisymmetric. CFD simulations of grid arrays, however, require three-dimensional computational grids. Given the fine grid required to resolve shock interactions and pressure peaks, the number of elements required for an accurate analysis of grid arrays using CFD quickly becomes infeasible.

With the computational limitations in mind, a small grid array of 1 g sources was simulated. The numerical simulation lasted *10 hours* on *512 processors*. The analytical model results were generated in *5 seconds* on *one processor*. The array size is essentially at the limit of what is computationally possible at present using the

CFD code. The array and standoffs where pressure histories were recorded appear in Figure 4.18. Pressures were observed directly beneath the front, center charge at

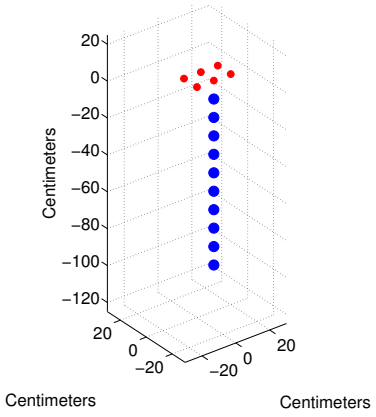

Figure 4.18: Six Charge Grid Array

10 cm increments. The grid spacing used in the 2x3 array is 10 cm. The composite waveform at the 10 cm standoff generated by the analytical model is compared to the numerical simulation in Figure 4.19. Given the complexity of the near-field behavior

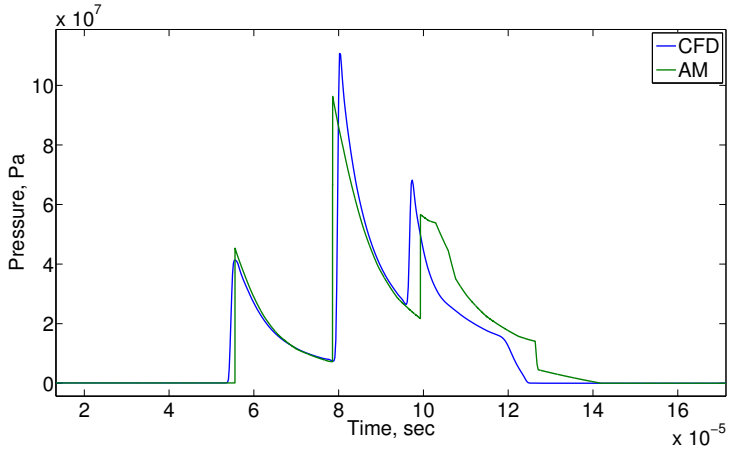

Figure 4.19: Six 1 g Charge Grid Array Pressure History, 10 cm Standoff

in an explosive array, and considering the nuances introduced by the grid geometry, the correlation is close. Peak amplitude is accurately represented and the decay profile of each individual wave matches both in profile and duration.

A second near-field result is shown in Figure 4.20. Again, peak magnitude is

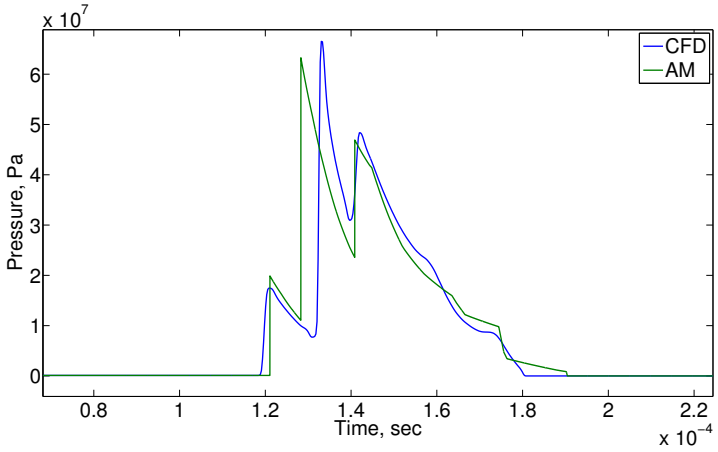

Figure 4.20: Six 1 g Charge Grid Array Pressure History, 20 cm Standoff

predicted correctly, and the decay profile due to the superposition of rarefaction and shock waves is adequately characterized. A final result from the 2x3 array, the pressure history at the 100 cm standoff, is depicted in Figure 4.21. The peak is somewhat overpredicted, but the overall correlation is strong.

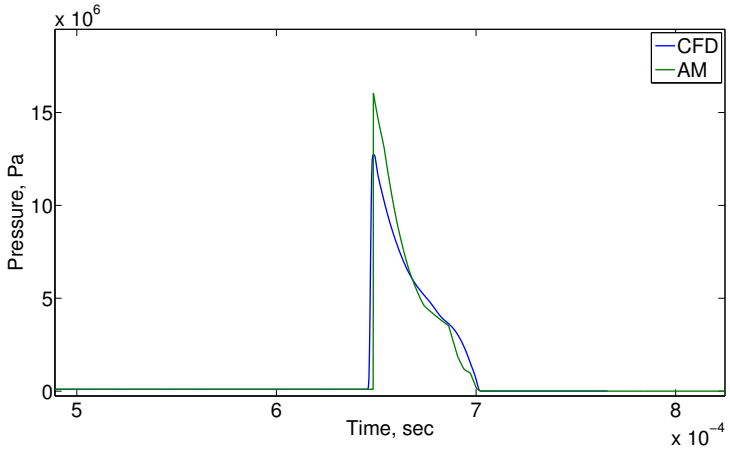

Figure 4.21: Six 1 g Charge Grid Array Pressure History, 100 cm Standoff

It is important to mention that the target region for the full scale multiple-source array is not the near-field, rather the target point will likely be several array spans below the array. Analytical model performance in the far-field must be as accurate as possible, while near-field deviations from numerical simulations can be afforded if they are relatively minor (as in the case of the second peak which arrives prematurely

in Figure 4.20). In view of the pertinent target range, and in consideration of the pressure waveform results that have been presented for line and grid arrays of 1 g sources, the analytical model has been validated for use in multiple-source explosive array design optimization for 1 g sources. The following section will compare results for similar charge arrangements with the source weight increased to 1 lb.

4.4 1 lb Charges

When the multiple-source explosive array concept was first envisioned, the proposed shock sources were not explosives at all. Rechargeable nastic arrays were studied as a means of imparting and focusing energy in water. Nastic sources are comprised of a flexible membrane backed by a detonation cavity where hydrogen is ignited. The explosion deflects the membrane outward, creating a shock wave (much like an acoustic speaker creates a sound wave). The peak pressure and decay characteristics of the shock waves produced by these devices closely resembled the pulse created by a single 1 g TNT charge. However, the impulse produced by an array of 1 g charges too small to impart significant energy at large depths (>30 m). Using larger 1 lb spherical sources has been suggested as a means to marshal sufficient pressures at deep standoffs. CFD results have been generated for arrays with 1 lb charges and are compared with analytical model predictions below.

4.4.1 Line Array

Numerical results were computed for a five charge line array with the same fluid domain setup as in the analyses discussed earlier. Charge spacing was increased to 77 cm (approximately 2.5 ft). A 1 lb TNT charge has a radius of approximately 4 cm. Using 10 cm spacing, as before, would leave less than 2 cm between the surfaces of neighboring charges. Detrimental interaction leading to significant weakening of the pressure pulse at the target would ensue. Just as 10 cm was selected for the 1 g charge

arrays, 77 cm was selected for 1 lb charges because, with this spacing, neighboring charges are spaced sufficiently far apart to avoid deleterious near-field interactions.

4.4.1.1 Centerline Results

Pressure histories were examined at further standoffs than the 1 g charge examples. Figure 4.22 depicts the five 1 lb charge array layout and target distances that were studied. As before, two near-field and two far-field examples will be presented. Intermediate cases can be found in Appendix B. It is important to note that the numerical results were generated in *8 hours* using *six processors*. The longest analytical model computation time (for the 800 cm standoff) was less than *200 seconds*.

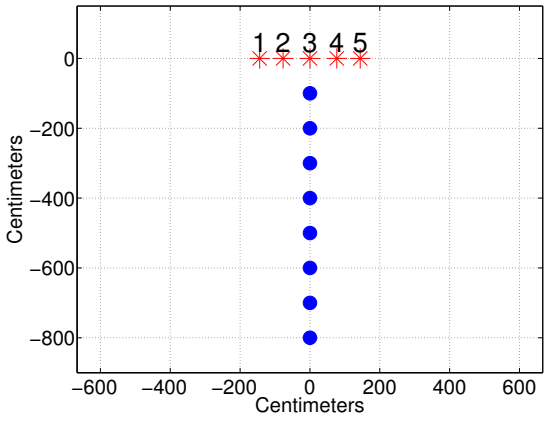

Figure 4.22: Five 1 lb Charge Line Array Setup

The 100 cm standoff case is shown in Figure 4.23. The composite waveform closely resembles that pulse created by the 1 g charge array at a 10 cm standoff. The resemblance demonstrates that 100 cm can be considered the near-field for a 1 lb charge array with 77 cm source spacing. The magnitude and decay of the first wave is predicted accurately, validating the use of weak shock theory for single 1 lb sources (the first wave travels alone into an undisturbed fluid, just as the wave produced from a single source would). The magnitude of the second peak is correct as well, although the second peak is accelerated slightly faster in the analytical model than

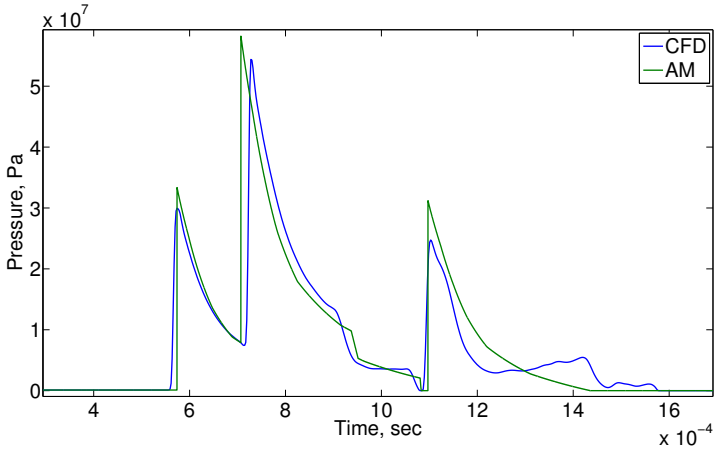

Figure 4.23: Five 1 lb Charge Line Array Centerline Pressure History, 77 cm Charge Spacing, 100 cm Standoff

in the numerical results. Rarefaction wave magnitude and propagation speed also correlate well with those determined by the CFD code.

Results are shown for the 200 cm standoff in Figure 4.24. The peak pressure correlation between analytical and numerical results is strong for the first wave. The second wave has begun to coalesce with the first in the analytical results. Had it arrived at

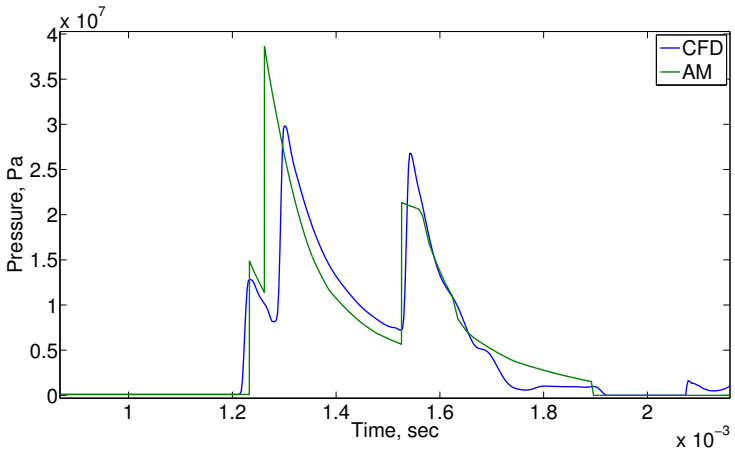

Figure 4.24: Five 1 lb Charge Line Array Centerline Pressure History, 77 cm Charge Spacing, 200 cm Standoff

the same time as its numerical analogue, the second wave magnitude would more closely resemble the corresponding numerically-generated peak. Shock-rarefaction interaction effects somewhat crudely model the third peak, though the disparity is

reasonable, and the rarefaction wave magnitude and arrival time seem to perfectly mimic the output from the numerical solver.

The first far field result is plotted in Figure 4.25. Although the first two waves coalesced prematurely in the near-field analytical results, the coalescence rate of the remaining two independent waves is predicted correctly in the far field. Once again, an average of the rarefaction wave effects yields close correlation with the rarefaction waves present in the CFD results. The peak magnitude of the second wave is noteworthy. In Figure 4.24, the first two peaks, barring the overestimated acceleration of the second peak, have magnitudes that are very close to the numerical values. The third peak is less than the numerical value. How, then, could the superposed analytical peak magnitude in the far-field exceed the numerical value when no shock-rarefaction interactions occur beyond the near-field?

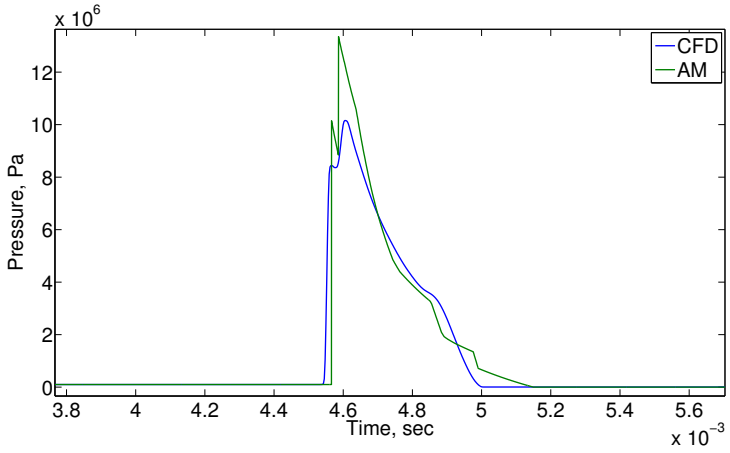

Figure 4.25: Five 1 lb Charge Line Array Centerline Pressure History, 77 cm Charge Spacing, 700 cm Standoff

An answer lies in the computational mechanics of the problem. A fine computational mesh is required when using the numerical tool to simulate shock waves produced by very small charges. A coarse mesh with large elements is analogous to decreasing the number of pixels in an image; the result is blurry and approximated. The line array results for 1 g charges have been computed using a two-dimensional

mesh (the problem is axisymmetric) with 0.05 cm square elements. Shock peaks can be clearly visualized at this resolution. The bounds of the computational mesh are increased for the 1 lb charge model, and, therefore, the individual element size is increased to maintain computational feasibility. Although the shock created by larger sources can be resolved with coarser elements than the shock from a 1 g source, the 1 lb source computation will sacrifice accuracy in the calculation of peak amplitude simply because the resolution is not fine enough. As such, it is concluded that the magnitude of the second peak in Figure 4.24 predicted by the analytical model may be a better estimate of the actual peak pressure than it appears.

A final far-field result for the five 1 lb charge array is depicted in Figure 4.26. Coalescence of all waves is predicted correctly, as are the rarefaction wave arrival times and magnitudes. The peak pressure from the analytical model may be more accurate than it appears, as discussed above.

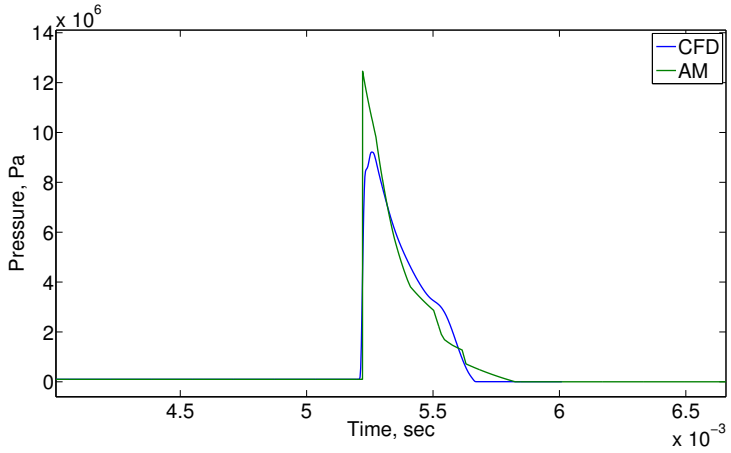

Figure 4.26: Five 1 lb Charge Line Array Centerline Pressure History, 77 cm Charge Spacing, 800 cm Standoff

4.4.1.2 Edge Results

The previous section presented numerical and analytical results for various standoffs below the center charge of the five charge line array. When the system is deployed,

however, the target may not lie directly underneath the center of the array. In such cases, it is important that the analytical model perform well when the target is located obliquely. To test this scenario, numerical simulations were conducted for the array and target points depicted in Figure 4.27. As before, near-field and far-field results will be presented.

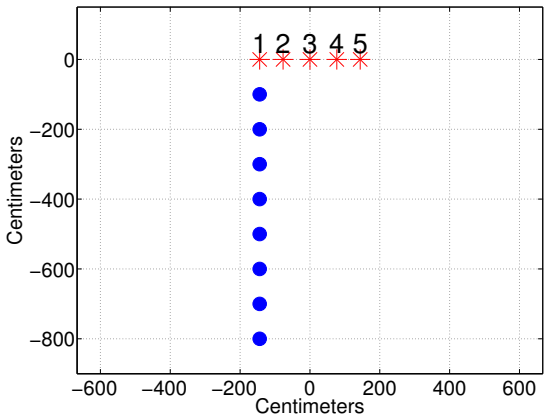

Figure 4.27: Five 1 lb Charge Line Array Setup, Edge Standoffs

Numerical results are compared to analytical model predictions for the 100 cm edge standoff in Figure 4.28. The added complexity of the composite waveform along the edge of the array is clearly visible. The fifth shock peak has been entirely decimated due to rarefaction interactions by the time the pressure waves reach the 100 cm edge distance. The peaks and troughs of the first two waves at 100 cm are predicted well by the analytical model, including the arrival of the first rarefaction wave. Although the peak magnitude of the third wave is modeled accurately, unknown nonlinear phenomena govern its decay as well as the characteristics of the final peak. It is noteworthy that, despite the presence of nonlinear phenomena that have not been included in the reduced-order model, the model still predicts peak arrival time correctly, a trend seen in all results presented in this chapter. The cause of the behavior following the third peak in Figure 4.28 is not yet understood. Near-field accuracy is not an emphasis in the reduced-order model except as it pertains to composite

waveform behavior in the far field.

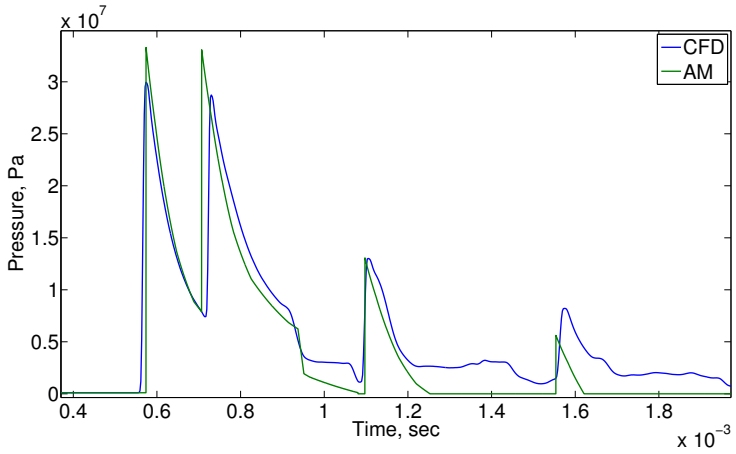

Figure 4.28: Five 1 lb Charge Line Array Pressure History, 77 cm Charge Spacing, 100 cm Edge Standoff

Moving further from the array, results at the 200 cm edge standoff are shown in Figure 4.29. All five peaks are now present, and the arrival time determined by the analytical model closely matches the arrival time in the numerical simulations. The shock-rarefaction penalty that has clearly affected the third peak proves to be a close representation of the actual attenuation and broadening of the wave that occurs in the numerical result. Nonlinear phenomena continue to hamper the prediction of the final wave. These effects are minimized in the far-field, however, as is seen at the 700 cm standoff in Figure 4.30.

The composite waveform is notably different in appearance at 700 cm. Each trailing shock is directly in the wake of a leading shock and the peaks have begun to coalesce. The analytical model predicts the rate of coalescence, peak shock magnitude, and the decay at the tail of the waveform (which is due to rarefaction wave superposition) in a result that closely resembles the numerically-generated pressure history at this standoff. The rarefaction wave between the third and fourth peak that has been calculated using the analytical model is too strong. The rarefaction strength error is most likely a symptom of inaccuracy in the heuristic shock-rarefaction inter-

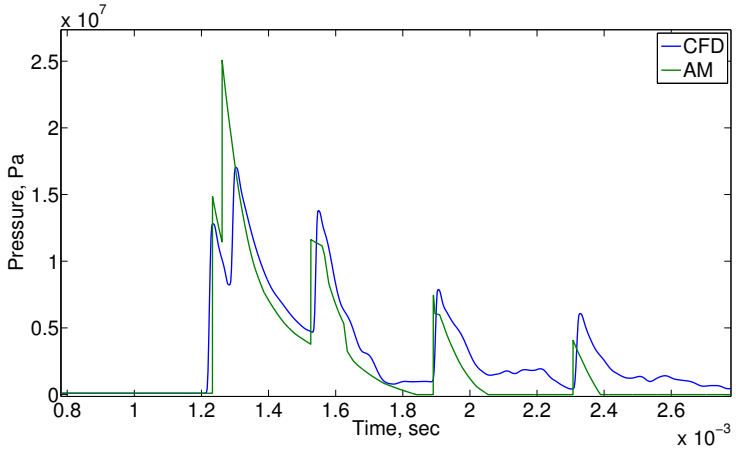

Figure 4.29: Five 1 lb Charge Line Array Pressure History, 77 cm Charge Spacing, 200 cm Edge Standoff

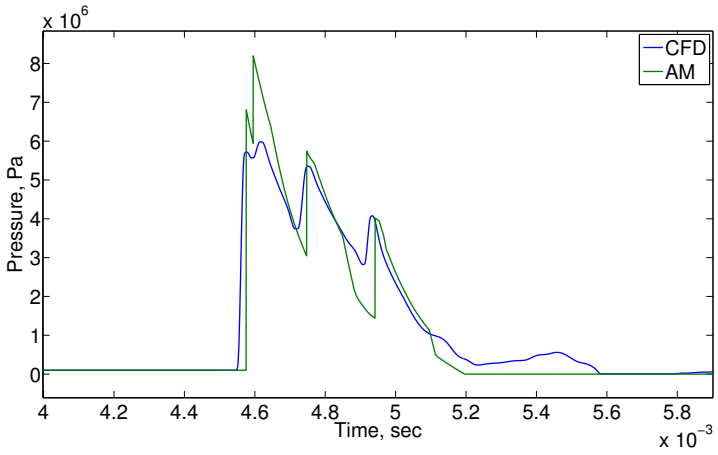

Figure 4.30: Five 1 lb Charge Line Array Pressure History, 77 cm Charge Spacing, 700 cm Edge Standoff

action model. In this case, the interaction penalty assigned to the rarefaction wave is too small. The strengths and weakness of the analytical model that are exposed at the 700 cm standoff can also be seen at the 800 cm standoff in Figure 4.31.

The centerline and edge standoff examples above validate the physics based reduced-order model for 1 lb charge line arrays, especially in the far-field. Any nonlinear effects in the near-field omitted in the analytical model do not, apparently, influence the waveform at large standoffs to an appreciable extent. Five charge line arrays were used as test cases because numerical computational restrictions prohibit simulation

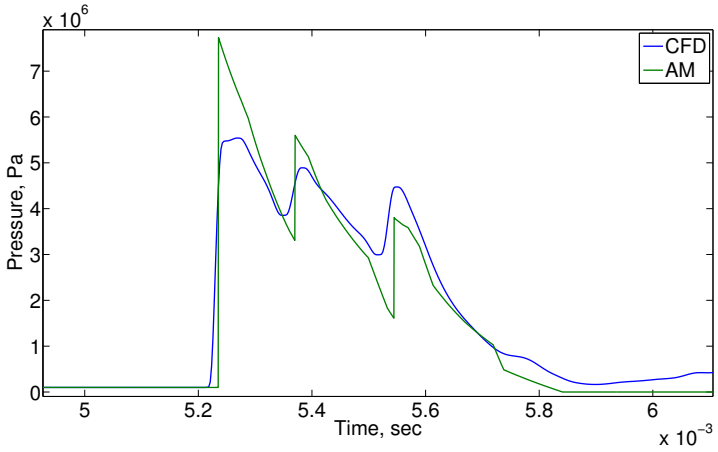

Figure 4.31: Five 1 lb Charge Line Array Pressure History, 77 cm Charge Spacing, 800 cm Edge Standoff

of larger arrays, as will be described in the next section. The analytical model has been validated for five charge line arrays incorporating both 1 g and 1 lb sources. The model has also been validated for small grid arrays with 1 g charges. The wave trains for five charge line arrays of 1 g and 1 lb sources resemble one another when standoff is scaled for charge size. Given that, it is assumed that the analytical model will perform well for small grid arrays of 1 lb charges, just as it does well for small grid arrays with 1 g sources.

4.4.2 Grid Array

The number of computational elements that can be used in the CFD model is restricted by available computational power. For large arrays, grid coarseness required for computational feasibility severely compromises the integrity of the solution. In plain terms, there are no existing means to simulate a two-dimensional multiple-source explosive array layout numerically at a charge spacing that is appropriate for 1 lb charges. From one perspective, the limitation of numerical solvers emphasizes the contribution of the reduced-order model: new areas of the design space such as large charges and deep standoffs, can now be probed and explored where they could not be examined previously. On the other hand, the analytical model cannot be validated for

such large arrays. Therefore, the realm of the multiple-source explosive array design space that includes larger array configurations is somewhat of an unknown frontier.

4.5 Chapter Summary

The efforts described in this chapter have sought to define and validate the physics-based, reduced-order model for the multiple-source explosive array. Initially, 1 g charges were studied due to the similarity between the pressure wave emitted from nastic sources (which were being proposed as an alternative to explosives at the time) and the pressure waves generated by detonating a 1 g spherical TNT charge underwater. Larger 1 lb spherical TNT charges were studied later due to the interest in focusing energy at large standoffs. The analytical model has replicated CFD results for line arrays and a grid array. Most importantly, the analytical model performs the computation for each case on the order of seconds, while the numerical simulation time ranges from hours to days on several processors. The reduced-order model has been used as a constraint function for the optimization framework discussed in the following chapter. The optimal designs for grid arrays with 1 g and 1 lb charges are presented in Chapter VI.

CHAPTER V

Optimization Overview and Setup for the Multiple-Source Explosive Array

Design can be described as a sequence of decisions where alternatives are identified in the construction or creation of an artifact (*Papalambros and Wilde*, 2000). Design *optimization* is the process by which decisions are made and favorable alternatives are selected to improve the designed artifact for its intended purpose. For some systems, evaluation of each alternative and its overall effect on the system can be accomplished by unsophisticated means. Designs of complex systems, such as the multiple-source explosive array, are harder to assess. Mathematical optimization techniques bridge this gap by analyzing esoteric tradeoffs and selecting design alternatives that improve overall functionality of a system. In the case of the multiple-source array, these alternatives include the number of sources in the array and the detonation timing of each source. The degree to which the waves produced by the array interact is complicated and highly nonlinear. In other words, it is impossible for the designer to determine an optimal timing scheme through intuition or trivial calculations. In essence, mathematical optimization extends understanding of complex systems. In the following section, optimization terminology and the elements that comprise an optimization problem will be enumerated, followed by a survey of optimization techniques.

5.1 Mathematical Optimization

5.1.1 Terminology

An optimization problem is characterized by the following parts:

- *Objective Function* - The criterion used to assess the quality of the design. In the case of the multiple-source explosive array, the best design will use as few sources as possible. The optimization algorithm will try to minimize the number of sources in the array. The number of sources, therefore, is the objective function.

- *Design Variables* - Aspects of the design that can be altered by the optimization algorithm. Variables represent design alternatives, such as the number of sources along the x-axis and the number of sources along the y-axis for the multiple-source array.

- *Parameters* - Not all facets of a design are negotiable, and some properties that could be variables are predetermined. In the design of a car, for instance, although four wheels are not necessarily required for a good design, the automotive engineer most likely is uninterested in a three or five-wheeled car. Four wheels, therefore, are a design parameter. The charge spacing and rectangular geometry selected for the multiple-source array are both parameters.

- *Constraints* - Limits placed on variables or functions of variables. For instance, if optimizing the diameter of a rod, we know that the diameter of the rod must be greater than zero. Likewise, the diameter may not exceed a certain limit. In this way, constraints set the upper and lower bounds of a variable. Constraints can be functions that are dependent on design variables as well. As an example, the rod in question must be able to sustain a certain amount of torque. This is a function of the design variables, and will ultimately contribute

to the determination of the rod diameter lower bound. The critical constraint for the multiple-source array is a particular pressure duration at the target.

The broad field of optimization research attempts to identify the best way to improve a given objective function. Methods such as Monte-Carlo analysis, gradient-based methods, and genetic algorithms have been devised to achieve this task. Monte-Carlo analyses entail calculating objective function values for a massive set of randomly-selected design variable combinations. Feasibility (adherence to constraints) and optimality are evaluated and the best feasible design is simply picked out of the group. Essentially, this is a 'brute force' method. Monte-Carlo analysis is poorly suited to solve optimization problems with computationally expensive objective functions or large ranges of possible design variable values.

Gradient-based methods are named for the mathematical approach they employ. Also called 'hill-climbing' methods, these algorithms approximate the derivative of a composite function formed by some combination of the objective function and constraint functions, and follow the gradient to higher or lower values, depending on whether the objective function is to be maximized or minimized. Gradient-based approaches rely on continuously differentiable functions, which also requires variable values to be continuous. Although some enabling modifications have been developed, gradient-based optimization techniques generally cannot be applied to problems with discrete variables, such as the number of sources in the multiple source array. Furthermore, gradient-based methods tend to struggle with highly multimodal problems; local gradients can become misleading in the search for a global optimum. For these reasons, a hill-climbing approach has not been appropriated for this research effort. A genetic algorithm has been selected instead, due to the resistance to local minima and the ability to incorporate discrete variables it offers.

5.1.2 Genetic Algorithms

Genetic, or evolutionary, algorithms are global search methods inspired by the process of biological evolution (*Chipperfield and Fleming*, 1995). They are effective for problems with high levels of variable interaction, known as epistasis in the field of biology (*Haupt and Haupt*, 2004). A genetic algorithm begins by establishing a randomly generated population of design variable combinations. The 'fitness' of each population member is assessed and the most fit members of the population, those whose objective function value is best, are most likely to 'mate' and create a new population member for the next generation. The offspring are evaluated again, with the best members of the population becoming the most likely candidates to produce new designs for the next generation, and so on. The reproduction process is underpinned by chromosomal encoding. Variable values are encoded into 'genes' which, when combined with other genes, form a chromosome that defines a particular design. A chromosome is essentially a complete sequence of design variables. The most common encoding scheme is binary encoding, where variable values are translated into binary strings that are later used for crossover and mutation (to be explained later) in the algorithm. A sample binary coding scheme is given for clarity (*Haupt*, 1995).

Given a design with N_{var} variables v_i, a chromosome will be defined by N_{var} variables given by:

$$chromosome = [v_1, v_2, ...v_{N_{var}}] \tag{5.1}$$

The fitness function, therefore, is dependent on the genes comprising the chromosome. The variable values can be converted into binary form using the following function:

$$q_n = \sum_{m=1}^{L_n} b_w[m] 2^{1-m} Q \tag{5.2}$$

where q_n is the quantized version of v_n, L_n is the number of quantization levels for q_n,

b_w is the array containing the binary string that represents q_n, and Q is the largest quantization level. Quantization is the process by which a set of continuous values is sampled and categorized into nonoverlapping subgroups. Adding quantization values is akin to adding significant digits to the resolution of each variable.

Once each design has been sequenced into a chromosome, the fitness is assessed and the strongest population members are most likely to 'mate', or swap certain genes. The number of genes that are swapped, or the point on the chromosome that operates as the boundary for a swapped region, is defined by the crossover operator used by the genetic algorithm. The 'offspring' of this genetic exchange, therefore contain traits from both of the 'parent' chromosomes. The amount of crossover that occurs during each mating is often a probabilistic process. Parent chromosomes ultimately produce enough offspring to take their place in the future generation as well as replace members of the current population that have been thrown out due to poor fitness. In this way, the population size remains constant from generation to generation.

Mutation is an important characteristic of a genetic algorithm. Mutation randomly alters specific genes in offspring chromosomes to maintain diversity of the overall population. Hill-climbing optimization techniques are often stymied by multimodal problems where several local optima crowd a global optimum. By mutating a portion of the population, a genetic algorithm ensures that the population does not get stuck in a local optimum; there are always a few outlying designs that are exploring other regions of the design space. When a mutated population member finds a more optimal region, the population, through crossover, will gradually shift to the new region and collectively attain increased fitness. The composite waveforms produced by the multiple-source explosive array are not always exclusive functions of a single unique detonation timing scheme. It is possible that identical pressure histories at the target may be produced by different detonation timings. As a result, many local optima abound. Genetic algorithms, through mutation, counteract this

difficulty by constantly searching multiple regions of the design space.

5.2 Relevant Optimization Design Problems

The multiple-source array problem is complicated due to the interaction of various shock and rarefaction waves as they propagate to the target. In the absence of interaction, the design problem is quite simple and sophisticated optimization techniques become unnecessary. The wind farm layout problem is subject to similar source interaction effects that influence the system objective (*Chowdhury et al.*, 2012).

Much like the composite waveform generated by the multiple-source explosive array, the total power generated by a wind farm is less than the total power potential of each wind turbine. Wake effects, such as shading, can decrease the efficiency of downstream turbines (*Beyer et al.*, 1996). This effect is similar to the rarefaction waves produced by neighboring explosive gas bubbles; shock-rarefaction interaction and superposition of rarefaction waves at the target reduce the potential contribution of each source. Turbine locations and number are the design variables in the wind farm optimization problem.

The number of sources is also a variable in the explosive array design problem. Because spacing is fixed, the detonation timing of each source forms the set of variables for the second-tier array optimization problem. In one sense, explosive source spacing can be used in lieu of detonation timing; shock arrival time can be increased by detonating the source later or moving it farther from the observation point. Extending the breadth of the array by moving sources away from one another reduces the contribution of the outer sources, simply because the standoff for these sources at the target increases as charge spacing in the array is increased. For this reason, explosive charges have been placed as closely as possible and detonation timing is used to govern the way shock and rarefaction waves propagate and interact in the multiple-source array.

In view of the similarity between the multiple-source explosive array design problem and the wind farm layout optimization problem, it comes as no surprise that common difficulties arise when attempting to optimize these systems. When a total aggregate efficiency objective is used, the wind farm layout problem becomes highly multimodal. Chowdhury et al. selected a particle swarm optimization (PSO) algorithm to overcome the difficulty posed by numerous local optima. PSO's are cousins to evolutionary algorithms because both use stochastic search methods to adeptly handle multimodal design spaces. A PSO was selected for the wind farm optimization problem because it was simple to implement compared with genetic algorithms (*Chowdhury et al.*, 2012). The present study employed the *ga* function in MATLAB, a tool that greatly simplified implementation and adjustment of the genetic algorithm.

5.3 Framework

A unique optimization structure is required to study the multiple-source explosive array design. The overarching design objective is to use as few shock sources as possible. The most important performance metric is that pressure at the target must exceed a certain threshold for a specified duration. The feasibility of each design, therefore, is established by achieving this duration through strategic detonation of each source in the array. The optimization process is two-tiered in this sense. On the top level, an optimization algorithm attempts to reduce the number of sources in the design. Meanwhile, the feasibility of each design specified by the top level is assessed by optimizing the detonation timing of each design on the second tier. Figure 5.1 depicts the conversation between the individual optimizations.

Spherical TNT explosive charges have been selected as sources. To simplify the analysis, a rectangular grid of sources has been specified for the array geometry. The problem is constrained further by maintaining a uniform spacing between each charge in the rectangular grid. The top level optimization is characterized by only

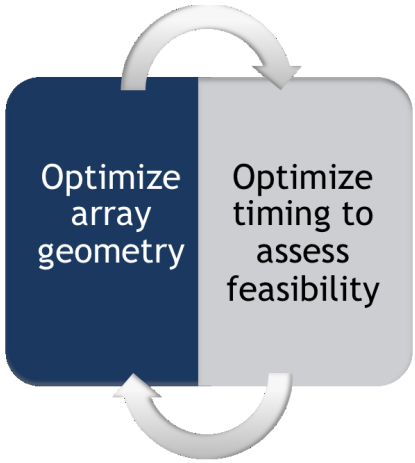

Figure 5.1: Two-tiered Optimization Structure

two design variables: the number of columns and number of rows in the array. As noted in Chapter IV, spacings of 10 m and 77 cm have been selected for the 1 g and the 1 lb sources, respectively. Multiple numerical analyses have demonstrated significant deleterious interaction effects when the charges are spaced closer together. At small charge spacings, complex near-field phenomena destroy most of the useful overpressure and feasible designs require many more sources. The specified charge spacings ensure suboptimal near-field interactions are minimized.

The two-tiered optimization is implemented with the top tier operating as the objective function and the second-tier optimization operating in the place of a constraint function. A satisfied constraint in the *ga* function in MATLAB has a negative value. Therefore, the pressure duration at the minimum threshold resulting from the optimal detonation time of each array geometry is subtracted from the minimum duration requirement. When the number of sources is insufficient (no timing can be found for that configuration that will achieve the required pressure duration at the target), the constraint is not satisfied and the top-level algorithm searches elsewhere in the configuration design space. The constraint optimization is terminated as soon as the constraint is satisfied, rather than continuing to search for a more optimal tim-

ing scheme, to maximize computational efficiency. In summary, the multiple-source explosive array design optimization can be described as follows:

Minimize: *Total number of charges*

with respect to: *numC, numR*

subject to: *Duration minimum* d_{min} *at threshold* P_{min}

The second tier optimization, which acts as a constraint for the top-level optimization, is described below:

While $duration < requiredDuration$:

Maximize: *Duration of* $p > p_{min}$

with respect to: *detonation times* $t_{d1}, t_{d2}, ...t_{dn}$

subject to: $0 < t_{di} < 2 * r_i/c_o$

Where p_{min} is the specified threshold pressure and r_i/c_o is the arrival time at the target of a shock emitted from source i if it traveled at the sound speed of the fluid. The effectiveness of the second-tier optimization, followed by an application of the full two-tiered analysis for both 1 g and 1 lb source arrays are established in Chapter VI.

5.4 Chapter Summary

The mathematical optimization approach applied to the multiple-source array problem has been described in this chapter. Evolutionary-type algorithms have been selected as opposed to gradient-based methods because the design problem is highly multimodal and the number of explosive sources is discrete (gradient-based optimization algorithms typically require continuous variables). Monte-Carlo analysis has also been ruled out given the computational expense stemming from the sheer number of

model evaluations necessary to explore the design space. The design objective for the multiple-source array, to use as few sources as possible, is bounded by the pressure threshold duration constraint. In order to assess an array configuration proposed by the top-level optimization, a second-tier optimization must ensure to probe the maximal destructive capability of the proposed configuration. The threshold constraint inspired the development of the two-tiered optimization approach. The following chapter describes multiple case studies where the optimization framework described here has been applied to array design problems.

CHAPTER VI

Two Case Studies: 1 g and 1 lb Charge Arrays

The reduced-order model and optimization framework described heretofore have been combined for the analysis of multiple-source array designs. In keeping with the originally proposed concept, sources are arranged in a grid configuration and each charge is detonated independently. Performing optimization analysis with preexisting analytical or numerical methods would have been fruitless. Existing analytical models poorly characterize the composite waveform produced by the multiple source array and, thus, the optimal results identified by the algorithm would not be replicated upon deployment of the array. Existing CFD options require excessive computational time and storage. Evolutionary algorithm-based optimization could take months under these circumstances because each model evaluation would be costly. Furthermore, computational power necessary to simulate large grid arrays is not available at present. With the limitations of pre-existing methods in mind, the analytical model developed and presented in this thesis is used to optimize grid arrays of explosive sources in this chapter.

It is important to mention that the optimization analyses described below were conducted for a notional objective function: minimize the number of sources. The constraint function, a sustained pressure for a specified duration, is also somewhat arbitrary. Depending on the application, an array might be called upon to perform

any number of tasks. As such, the numeric values used in the constraint function and even the objective function itself merely form a proof of concept study. The two-tiered optimization structure is relatively easy to implement, and was specially developed for a particular design objective. The analytical model, itself, is the centerpiece and comprises the lion's share of the technical developments accomplished in this research effort.

6.1 Constraint-Level Detonation Timing Optimization

The second-tier detonation timing optimization setup is validated using a five source line array of spherical 1 g TNT charges. The charge and target arrangement are depicted in Figure 6.1. For the validation case, the pressure threshold is set to 30% of the peak pressure from simultaneous detonation: 3.6×10^6 Pa. This threshold

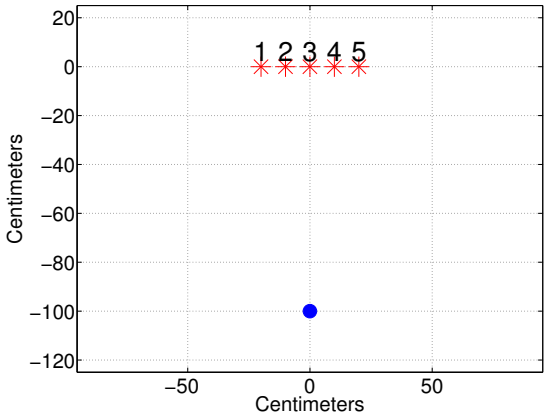

Figure 6.1: Detonation Timing Validation, Five 1 g Charge Array

has been selected because the waveform from simultaneous detonation is broad at this pressure level. As such, the duration of the pulse from simultaneous detonation should be relatively long at the threshold, yielding a near-optimal pressure wave at the target. Timing schemes identified by the optimization algorithm, therefore, are competing with an intuitively optimal detonation timing sequence. If improvement is

made on the intuitive solution (the duration increases), the strength of the detonation timing optimization approach will be demonstrated.

As mentioned previously, the timing optimization problem is highly multimodal. The default mutation rate in the *ga* function in MATLAB is 1%. Bhatia and Basu suggest setting the mutation rate to the inverse of the total number of variables (*Bhatia and Basu*, 2003). The convergence rate of a genetic algorithm slows as the mutation rate increases, hence the algorithm may never converge if the mutation rate is too high. Because a mutation rate of 20% could hamper convergence, 10% has been used both in the detonation timing validation case and in the second-tier optimization as implemented in the overall framework.

When using genetic algorithms, it is best to use the largest feasible population and number of generations. Adding generations will only improve the solution, and the optimization termination criteria can be set so that the algorithm stops when a single optimal value has been identified for a pre-set number of generations (the solution stagnates). To explore the detonation timing optimization validation case fully, 1000 generations with populations of 100 unique timing schemes were allocated. Table 6.1 lists the optimal detonation timing scheme for a five charge array that was determined using the optimization algorithm. Geometric symmetry was used to simplify the analysis. The resulting waveform is compared to the pulse generated when the charges are detonated simultaneously in Figure 6.2. The CFD results for the optimal timing scheme are also shown to illustrate the accuracy of the analytical model as a surrogate for the numerical tool in its role as the constraint function in the optimization framework.

When the charges in the array are detonated with the optimal timing scheme, a trailing shock wave arrives at the target just as the pressure from the leading shock decays to the approximate threshold level. The optimal waveform exhibits two distinct peaks. In the intuitively optimal case, each wave would arrive separately to

Charge Number	Detonation Time [s]
1	1.59×10^{-5}
2	0
3	5.3×10^{-6}
4	0
5	1.59×10^{-5}

Table 6.1: Five Charge Line Array Optimal Timing

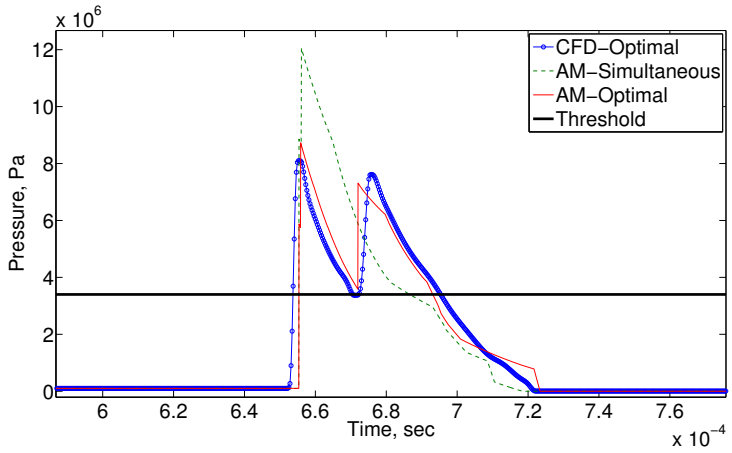

Figure 6.2: Optimized Detonation Timing Pressure History, Five 1 g Charge Line Array

sustain the threshold for the longest duration possible. The five charge line array is capable of creating three distinct waves when symmetric detonation timing is used. Coalescence appears to be unavoidable, however, for the first two waves produced by the five 1 g charge line array if the composite waveform must meet the specified pressure threshold. Coalescence may be avoidable only if the detonations were spaced further apart; this would, almost certainly, cause the aggregate pressure to fall below the threshold.

The optimal pulse is also wider than the simultaneous detonation pulse at all pressures below the threshold. As mentioned previously, the threshold of 30% simultaneous peak pressure was an ambitious challenge for the optimization algorithm because the simultaneous detonation waveform is broad at that pressure. Had the threshold been decreased, the duration would have increased for the optimum as the

trough between the first and second peaks would be lower and, hence, the optimal timing case would yield results that far surpassed the simultaneous timing case. The results depicted in Figure 6.2 demonstrate the power of the second-tier optimization algorithm. The analytical model itself is further validated by the comparison with CFD results for the optimal timing case and the analytical and numerical predictions closely resemble one another. It is important to note that the CFD results shown in Figure 6.2 were generated over 5 hours and 49 minutes using six processors. Optimization with the analytical model was executed in 2 hours and 13 minutes on six processors. The optimization algorithm terminated after fifty-one generations due to stagnation of objective function value. Performing the same number of function evaluations using the CFD solver would have taken over three years.

6.2 Grid Array with 1 g Sources

Once the second-tier algorithm had been validated, the entire optimization framework was exercised with a grid array incorporating 1 g charges. The minimum and maximum array size constraints are plotted in Figure 6.3, with the minimum array size constraint represented by the solid spheres and the maximum array size constraint represented by all spheres, both solid and empty. The target is located 1 m below the center front edge of the array and the explosive charges are spaced 10 cm apart. Symmetry was used to reduce computational time. Therefore, if $numC = 2$ in the symmetry case, there are three columns total, if $numC = 3$ in the symmetry case, the actual array has five columns total, and so on.

The optimization statement for this test case is stated as follows:

Minimize: *Total number of charges*

with respect to: *numC, numR*

subject to: $P > 1.4{\times}10^{7}$ *Pa for* $3.5{\times}10^{-5}$ *s @ 1 m depth,*

$2 < numC < 5,\ 2 < numR < 5,$

$0 < t_{di} < 2 * r_i/c_o$

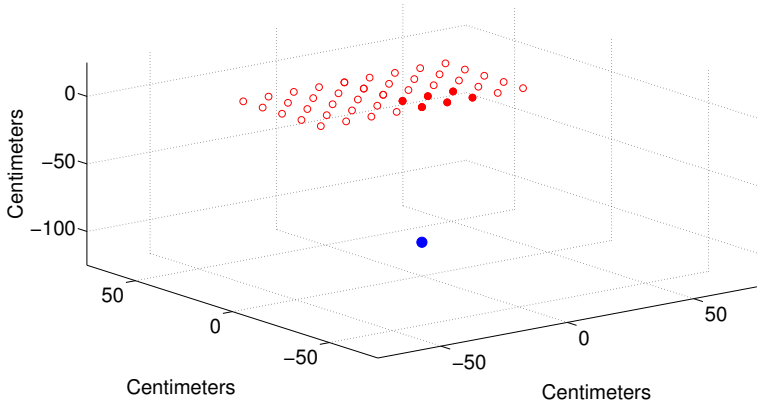

Figure 6.3: Grid Array Test Case, 1 g Sources

The pressure threshold was set to quadruple the threshold used in the five charge line array problem in hopes that the optimal design would not be the minimum or maximum array size. Limiting the detonation time range ensures that the variable space is not so broad that the algorithm searches fruitlessly without convergence. Still, the constraints provide enough flexibility for unique waveforms to be created with several different composite wave profiles.

Given the geometric bounds, 16 different array geometries are possible. The top level optimization is not necessary in this case, therefore, as each design could easily be optimized for detonation timing alone followed by a simple comparison of the results to identify the optimal case. In this sense, the top-level optimization would be a Monte-Carlo approach, while the second-tier approach would remain the same.

This particular design problem is elementary, however. The array size is small relative to certain applications and the target is relatively close at 10 charge spacings. The computational time for larger arrays and further targets will necessitate a truncated search of the array design space. Optimization, rather than a brute force approach, has been conducted at the top level for this reason.

The optimal geometry identified through the analysis is represented by the solid spheres in Figure 6.4. The resulting configuration is somewhat uninteresting, as

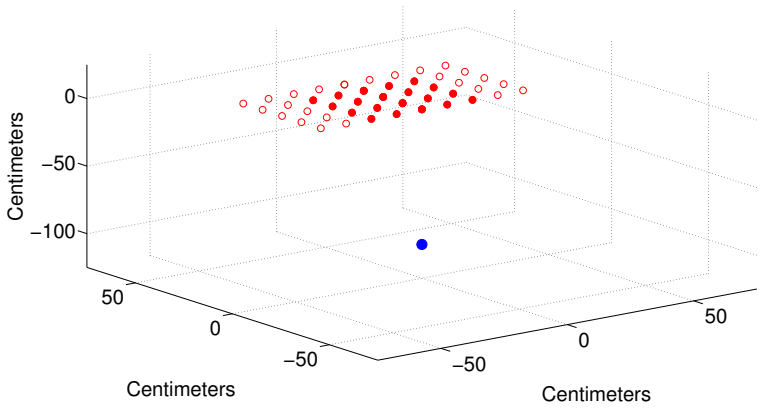

Figure 6.4: Grid Array Test Case, 1 g Sources - Optimal Configuration

the optimum geometry is quadruple the size of the original line array, just as the threshold has been quadrupled. Second-tier optimizations were performed with 20 generations of 50 member populations and a 10% mutation rate. This population size and number of generations is smaller than the quantities that were used to validate the constraint-level optimization, potentially sacrificing solution quality in exchange for computational efficiency. To ensure that the analysis did not omit a good solution due to fewer design space evaluations, 100 generations of 100 member populations at a 10% mutation rate were used to optimize detonation timing for the next-smallest-from-optimal array, with $numC = 3$ and $numR = 3$. The resulting maximum duration at the specified threshold is 3.07e-05 seconds, which does not satisfy the constraint.

The algorithm has identified the optimal array geometry even though fewer gen-

erations and a smaller population size were used in the constraint analysis. The composite waveform generated by optimum detonation timing schemes for the optimal configuration and the next-smallest configuration are shown in Figure 6.5. Although it seems that the smaller array may be capable of meeting the constraint (the optimal waveform falls short of the required duration by only a small amount), it is difficult to speculate on the feasibility of the smaller array due to strong coalescence physics that are in effect. It is noteworthy that the lengthy optimization used for the smaller configuration was not able to find a feasible optimum. If anything, the larger configuration solution is certainly more robust.

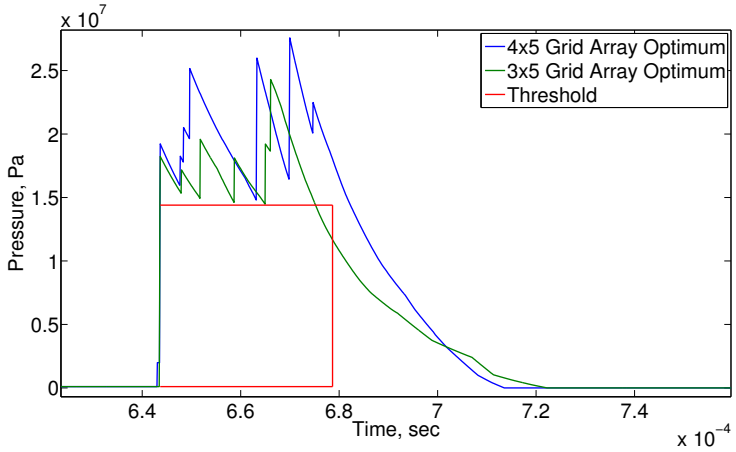

Figure 6.5: Optimum vs. Suboptimal Grid Array Pressure History Comparison

The use of 1 g charges throughout the development of the physics-based, reduced-order model and the creation of the two-tiered optimization framework has provided a testbed where analytical results can easily be compared to numerical models. The real target range of interest lies beyond the reach of these relatively small charges. The following section introduces the optimization of a 1 lb charge array, which projects energy to depths in the water where actual threats may reside.

6.3 Grid Array with 1 lb Sources

Optimization analysis has been conducted for a grid array of 1 lb sources. The optimization statement for this case is stated as follows:

Minimize: *Total number of charges*

with respect to: *numC, numR*

subject to: $P > 3.45\times10^{6}$ *Pa for* 3.5×10^{-4} *s @ 15 m depth,*

$2 < numC < 5,\ 2 < numR < 5,$

$0 < t_{di} < 2 * r_i/c_o$

The analysis was completed in approximately 4 hours on eight processors. With resulting values of $numC = 4$ and $numR = 3$, shown in Figure 6.6. Three generations of four configurations each were used for the top-level optimization, and five generations of fifteen timing schemes were employed for the constraint-level optimization. Admittedly, the search of the timing design space is not as rigorous as best practices within genetic algorithm-based optimization would dictate. To ensure that the optimum identified by the two-tiered optimization framework was indeed the best design, rigorous timing scheme optimizations were conducted for both an array with $numC = 3$ and $numR = 3$ and an array with $numC = 4$ and $numR = 2$. Ten generations of 100 timing schemes each were used to probe the timing design space thoroughly for the two smaller arrays. The optimal waveform produced by the first configuration achieved a duration of 3.18×10^{-4} s at the threshold pressure, which does not satisfy the constraint. The second configuration yields a maximum duration of 3.12×10^{-4} s for its optimal detonation timing case.

Due to the thorough analyses that were conducted to attain the maximum duration of each of the two smaller designs, it is concluded that the configuration determined by the two-tiered optimization framework is the true optimum design for the

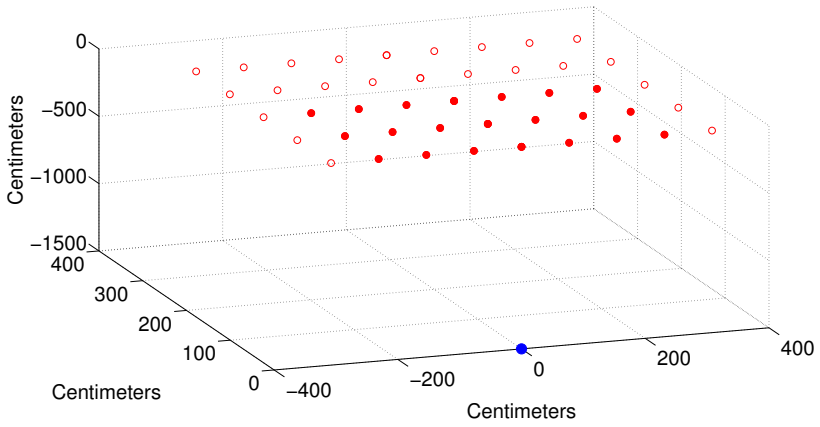

Figure 6.6: Grid Array Test Case, 1 lb Sources - Optimal Configuration

required pressure threshold at the specified standoff of 15 m. The optimal design is shown within the maximum size constraint in Figure 6.6, with the solid circles representing the optimum design and the hollow spheres indicating the maximum size constraint.

6.4 Application of the Optimization Framework to Design

The optimization framework and analytical model developed in this thesis can be applied to two stages of array design. The first stage concerns array geometry. Optimizations similar to those above should ensue, with the most challenging objective functions (deepest standoffs, longest durations, etc.) used to evaluate candidate designs. Once the array configuration has been specified, timing scheme optimization can commence. It is assumed that the deployed array will not be centered perfectly over the target during every usage; therefore, it is logical that several different target locations will be encountered, each corresponding to a unique optimal timing scheme. Given that the timing optimization analyses require hours to execute, it would be impractical to perform them in real-time while the array hovers over the target. It is suggested that the potential target range be identified and discretized, with optimization analyses conducted for each discrete element, so that when the array is deployed

and a target is identified, an optimum timing scheme for that location in the fluid has been previously identified. In this manner, the array could be used to defeat several threats without the bottleneck of real-time detonation timing scheme optimization.

6.5 Chapter Summary

The results presented in this chapter are the culmination of the efforts to construct a physics-based, reduced-order model and an optimization framework for explosive array design. The optimization framework is divided into two levels: a configuration level that seeks to optimize array geometry, and a sub-level optimization which seeks to identify optimal source detonation timing schemes for given geometries. The timing scheme optimization, which operates as a constraint function in the framework, has been validated using a five charge line array with 1 g sources. The optimum detonation timing outperforms the simultaneous detonation case at a pressure threshold where simultaneous timing yields a relatively broad waveform. The analytical model results for the optimal timing case are compared with CFD results for the same array using the optimum timing scheme. Good agreement is observed between the two predictions, validating the reduced-order model as a viable surrogate for the CFD code in an optimization loop.

After the quality of the timing scheme sub-level optimization had been established, arrays with sources arranged in a rectangular grid were optimized for both 1 g and 1 lb charges. The optima identified by the optimization framework were validated by examining array configurations that were slightly smaller than the configurations identified by the optimization algorithm. The optima determined by the optimization framework were validated for both source sizes, despite the fact that the timing scheme optimization in the optimization framework was much less rigorous than those used to validate the results by optimizing smaller arrays. Therefore, the algorithm successfully achieved the task of identifying the array capable of imparting

the prescribed pressure threshold for the specified duration with the fewest sources.

CHAPTER VII

Conclusion

The multiple-source explosive array design problem requires understanding of spherical shock waves, shock-bubble collisions, and the interactions between shock and rarefaction waves. The physics governing these phenomena have been distilled into a reduced-order model. Several conclusions can be made from this exercise. Array configurations that have been identified through optimization analysis provide further insight.

7.1 Conclusions

At the outset of the present research effort, transcending project objectives superseded the identification of any specific array design. Questions on the source size and source spacing necessary to impart a desired pressure for the desired duration at some target existed in the absence of means to answer such questions. The detonation timing precision required to strategically coordinate the arrival of multiple waves at the target was also unknown. The multiple-source explosive array concept was conceived in an effort to pragmatically explore these questions in an integrated environment with a real-world application.

The design space for multiple-source arrays was largely unprobed. Most analytical models deal exclusively with the characterization of a single shock wave. Existing

empirical methods capture single shocks to engineering accuracy and have been widely used. Propagation speed of a single shock wave is largely neglected because the arrival time of a single shock wave is immaterial. Until now, attempts to excite certain frequencies in marine structures were confined to manipulating the oscillation period of explosive gas bubbles. The shock waves produced by bubble collapse are relatively weak, however, and may not contain enough energy to sufficiently disturb a structure depending on its standoff from the bubble.

The multiple-source explosive array introduces the ability to create sustained pressures at specified thresholds and has been optimized to perform this task. The optimization algorithm is modular in that many other objective functions could be substituted. For instance, the multiple-source array adeptly projects individual shock waves into the fluid. The target arrival time of each wave could be tuned just as bubble oscillation has been tuned in the past. The marked advantage of the multiple-source array being that each shock that reaches the structure could be of similar magnitude. With this strategy, much more energy would be imparted to the structure compared to the impulse caused by a leading explosive shock and following bubble collapse shock waves.

Quantifying the behavior of shock waves emitted by a multiple source array using existing numerical tools is difficult. Although they are sufficiently sophisticated to capture multiple shock interaction phenomena, numerical tools face significant computational obstacles when simulating a three-dimensional domain. Although the CFD solver has been widely validated and the accuracy of the results it generates is not in question, the computational time and effort, as well as the data storage, necessary to conduct multiple-source array analyses is significant and limits both the array sizes and the target depths that can be simulated. Although such restrictions will be relaxed as hardware technology advances in the future, it is difficult to imagine a CFD code that approaches the speed of the analytical model.

Given the limitations of existing analytical and numerical models, reduced-order modeling offers the best opportunity to explore multiple-source array designs and to optimize variables such as array geometry and detonation timing. The analytical model described herein addresses the most important physical phenomena present in the flow field produced by the multiple-source explosive array: shock wave magnitude and propagation, rarefaction wave inception, and shock-rarefaction interactions. Prior to this effort, very few studies had explored the latter two topics in a liquid domain and closed-form solutions for these phenomena were nonexistent. The physics based reduced-order model, therefore, represents a substantial step forward in the realm of analytical shock modeling, both for single sources and multiple-source arrays of grid and line type.

Reduced-order modeling requires strategic implementation of simplifying assumptions. For example, the magnitude of the energy terms in the Tillotson equation of state are small when compared with the magnitude of the pressure and density terms (approximately 0.01%). As a result, the internal energy jump across a shock is ignored in the analytical model. Other simplifications, however, relied on more heuristic assumptions. The centerline model, for instance, incorporates the assumption that tracking shock propagation and interaction along a single computational line is sufficient to model the entire fluid domain. As with any heuristic method, validation is the only recourse to confirm that modeling simplifications accurately represent the system. To this end, the analytical model for the multiple-source explosive array has been tested against numerical simulations for five and twenty source line arrays with 1 g sources, a five source line array with 1 lb sources, and a two-by-three grid array with 1 g sources. This selection of test problems represents the span of array configurations that can be modeled with CFD given existing computational resources.

Conclusions can be drawn from comparisons with numerical results and optimization analysis. First, there is a minimum source spacing that should be used for spher-

ical explosive sources. When charges are placed closer than this minimum spacing, deleterious near-field interaction effects negate a significant portion of the cumulative impulse that is available according to superposition of the charges. Secondly, the detonation timing precision required to produce optimal composite waveforms is very high, often on the order of microseconds. It may not be feasible to control the detonation of each charge with this precision. In that case, simultaneous or near simultaneous detonation, especially for smaller arrays, may be the best option for deployment of the system.

The applicability of the piecewise-analytical model should be noted. Although the analytical model has been validated using a single CFD code, the model is not calibrated to the CFD code exclusively. The new value for the parameter β used in the propagation speed calculation is pertinent to results generated using any inviscid Euler solver that employs the Tillotson equation of state. Given initial near-field pressure and particle velocity histories from any other CFD code, the piecewise-analytical model should replicate the results generated by the other CFD code with the same accuracy as that which has been demonstrated in this thesis. The weak shock assumptions will still hold and the physics present will continue to be sufficiently captured by the models presented herein.

7.2 Future Research

A reduced-order model can always be improved. The physics based-reduced-order model contains two specific components that deserve further inspection. The structure of the centerline model itself implies certain assumptions. First, arrival time of each wave to the top of the computational line occurs in either a vacuum for shocks, or in the wake of a single shock for rarefaction waves. Chapter IV demonstrates that these assumptions are adequate for relatively small arrays. If a particular application favored using a larger array with small sources (versus a smaller array with larger

sources), the second assumption may begin to unravel. Without the ability to numerically simulate broad arrays, the sufficiency of the arrival time assumption will be difficult to test.

The centerline model also includes the notion that the entire fluid domain can be represented by wave propagation and interaction along a single computational line. It seems to be a fantastic assumption given the complexity of the flow field generated by the multiple-source explosive array. Without the ability to test the model against numerical results, this theory may have been dismissed. However, validated CFD tools existed to benchmark the reduced-order model. The question remains whether more complicated array geometries, such as circular or pentagon-shaped grids, can be modeled as simply.

The final component of the analytical model that deserves further review is the shock-rarefaction interaction model. The concept of shock waves overtaking rarefaction waves is not new; in fact, interactions in gas-filled shock tubes have been studied extensively (*Courant and Friedrichs*, 1948; *Moses*, 1948; *Bremner et al.*, 1960; *Sod*, 1978). In each of these studies, the result of the interaction of any kind of one-dimensional wave, whether one overtakes the other or they collide head-on, is that two waves are created and they propagate away from one another. Unfortunately this behavior is simply not seen in the numerical simulations of the multiple-source explosive array. The closed-form solutions for the interaction of shock and rarefaction waves, therefore, are only rough approximations of the actual effect for spherical waves. The physics governing two and three-dimensional interactions should be explored in order to incorporate a better interaction module in the analytical model.

APPENDICES

APPENDIX A

Intermediate 1 g Charge Array Results

Intermediate standoff pressure histories produced by CFD and the analytical model for the five charge line array and six charge grid array with 1 g sources are depicted below.

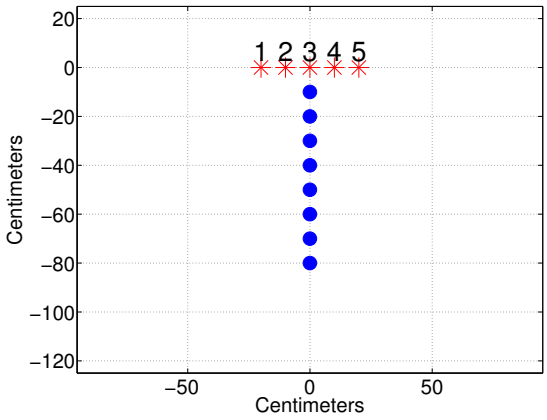

Figure A.1: Five 1 g Charge Line Array Setup

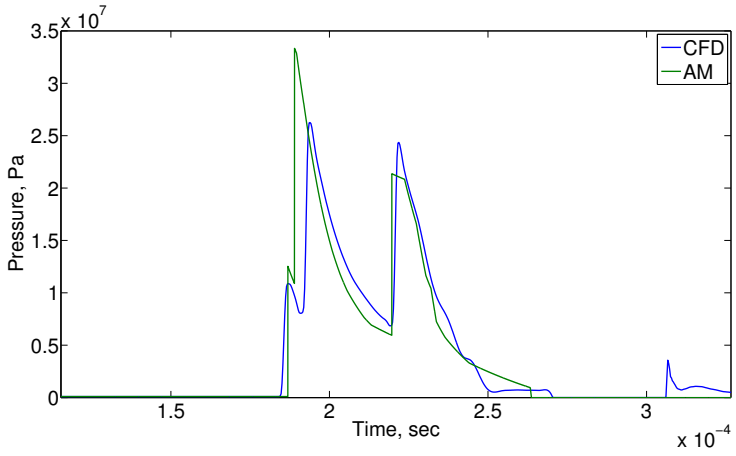

Figure A.2: Five 1 g Charge Line Array Centerline Pressure History, 10 cm Charge Spacing, 30 cm Standoff

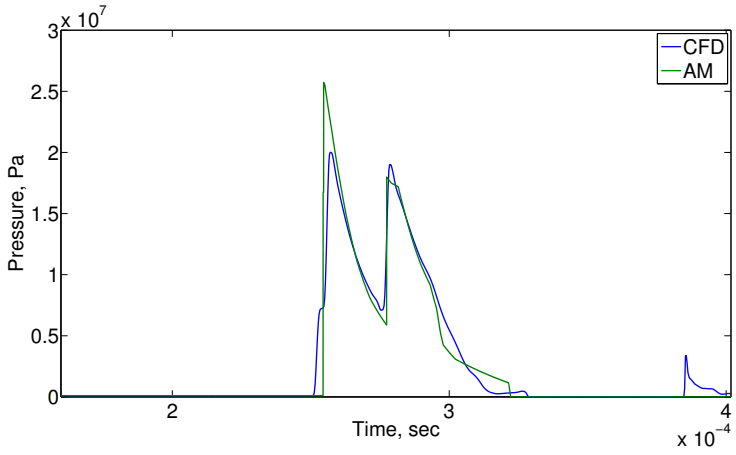

Figure A.3: Five 1 g Charge Line Array Centerline Pressure History 10 cm Charge Spacing, 40 cm Standoff

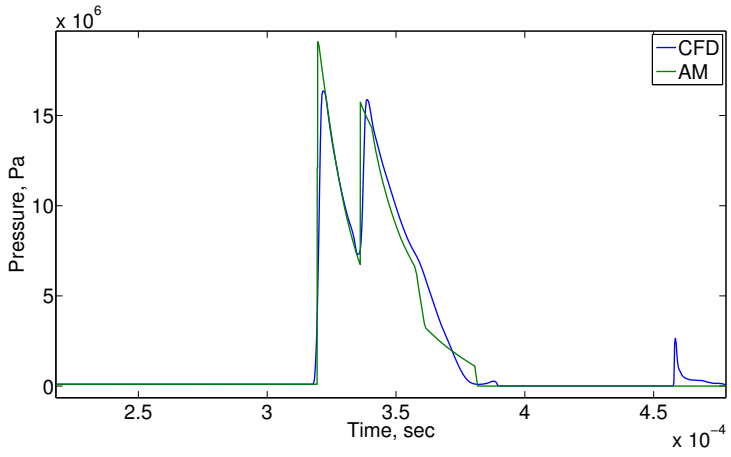

Figure A.4: Five 1 g Charge Line Array Centerline Pressure History, 10 cm Charge Spacing, 50 cm Standoff

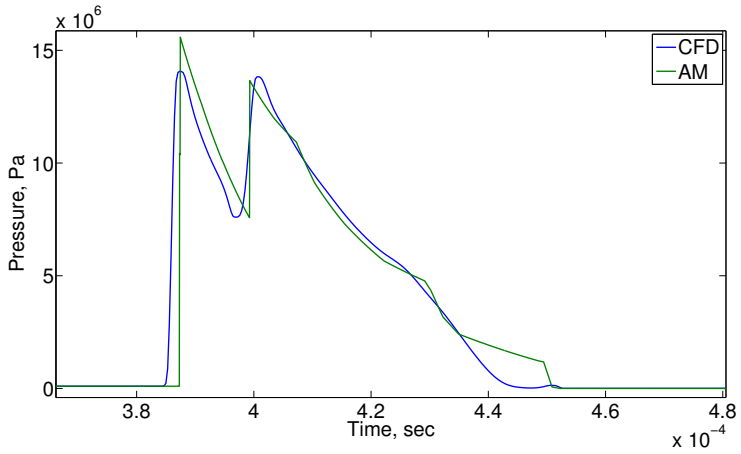

Figure A.5: Five 1 g Charge Line Array Centerline Pressure History, 10 cm Charge Spacing, 60 cm Standoff

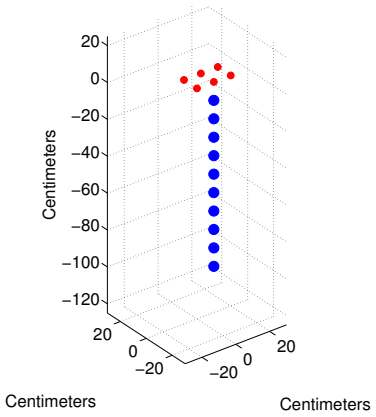

Figure A.6: Six 1 g Charge Grid Array Setup

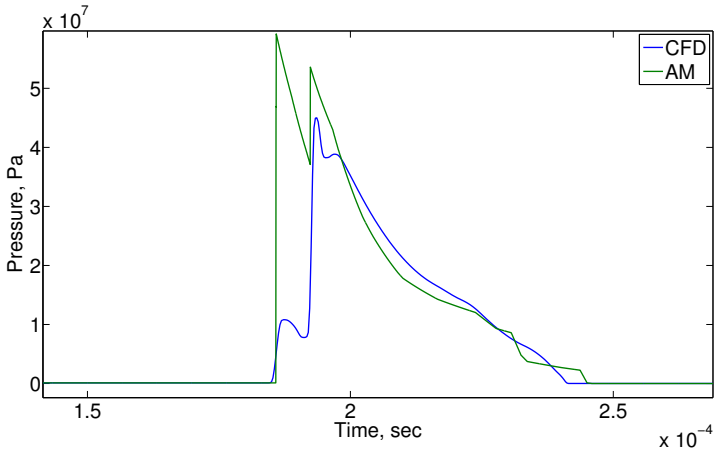

Figure A.7: Six 1 g Charge Grid Array Pressure History, 30 cm Standoff

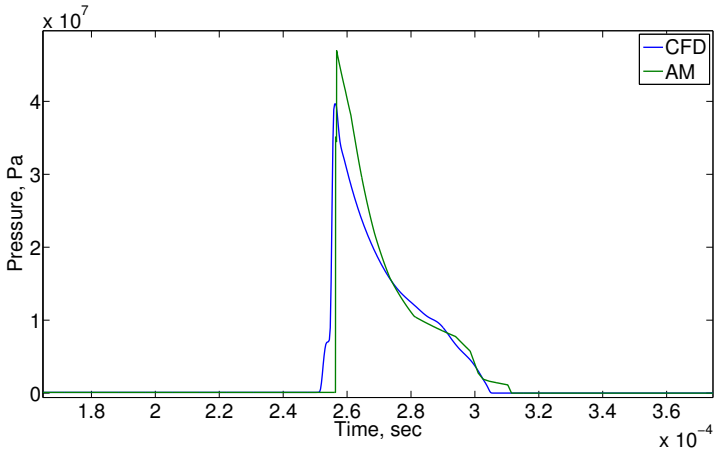

Figure A.8: Six 1 g Charge Grid Array Pressure History, 40 cm Standoff

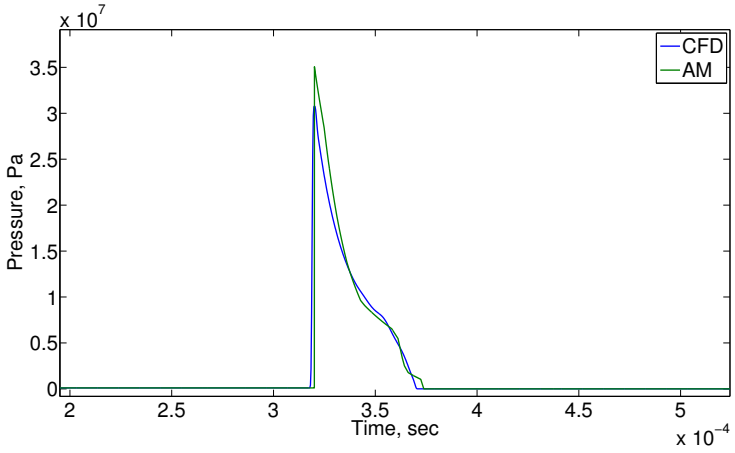

Figure A.9: Six 1 g Charge Grid Array Pressure History, 50 cm Standoff

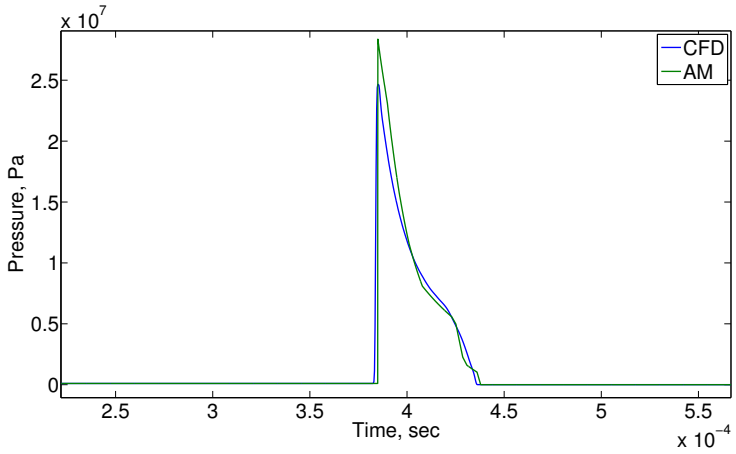

Figure A.10: Six 1 g Charge Grid Array Pressure History, 60 cm Standoff

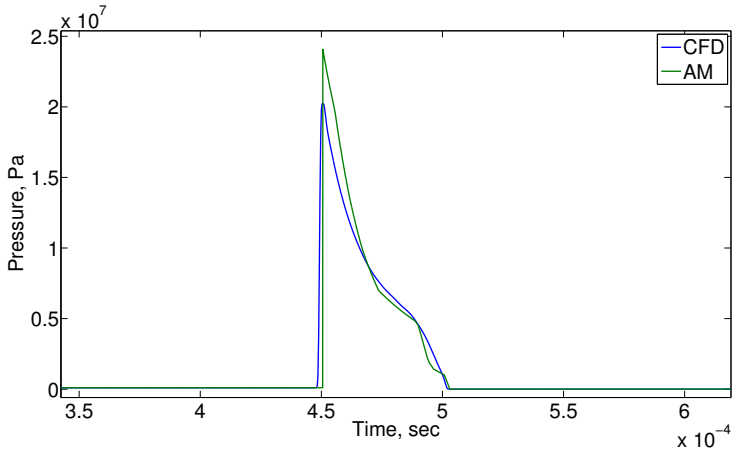

Figure A.11: Six 1 g Charge Grid Array Pressure History, 70 cm Standoff

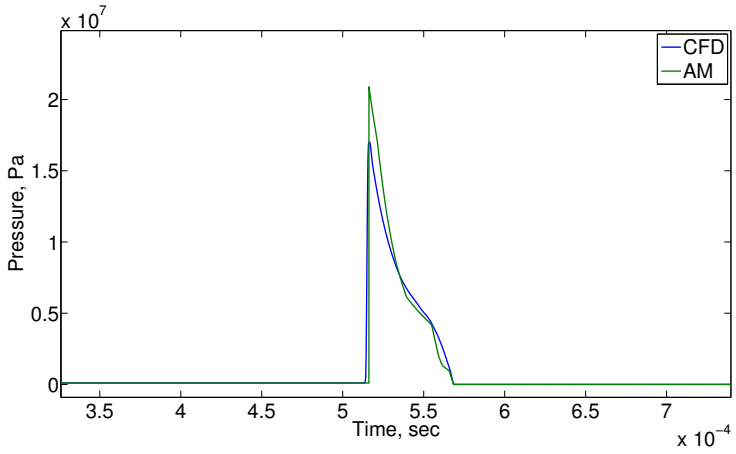

Figure A.12: Six 1 g Charge Grid Array Pressure History 80 cm Standoff

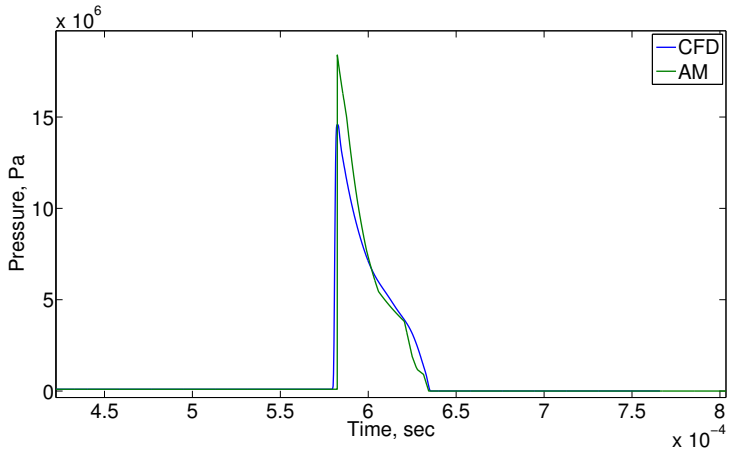

Figure A.13: Six 1 g Charge Grid Array Pressure History, 90 cm Standoff

APPENDIX B

Intermediate 1 lb Charge Array Results

Intermediate standoff pressure histories produced by CFD and the analytical model for the five charge line array with 1 lb sources are depicted below. Centerline results are shown first, followed by edge results.

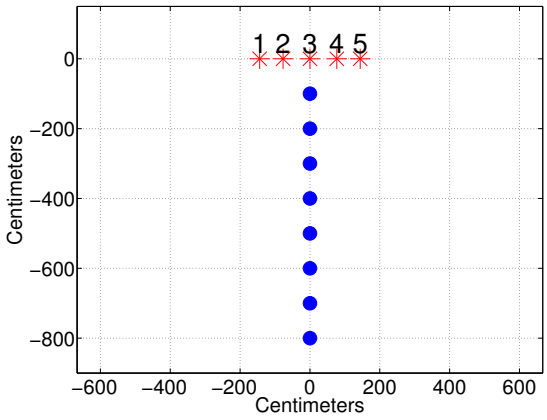

Figure B.1: Five 1 lb Charge Line Array Setup

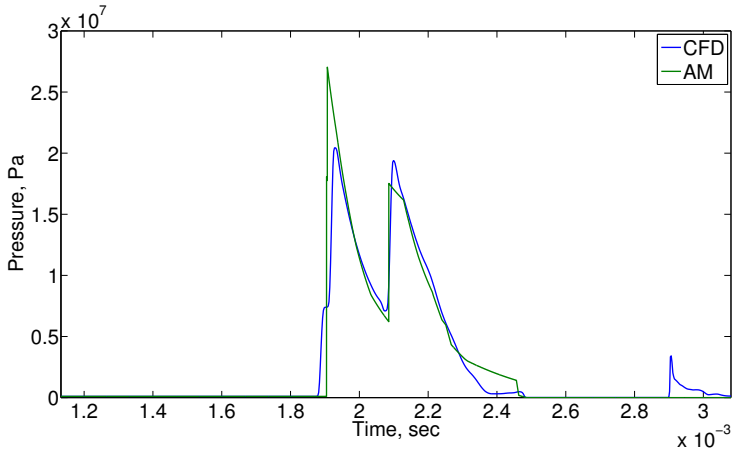

Figure B.2: Five 1 lb Charge Line Array Centerline Pressure History, 77 cm Charge Spacing, 300 cm Standoff

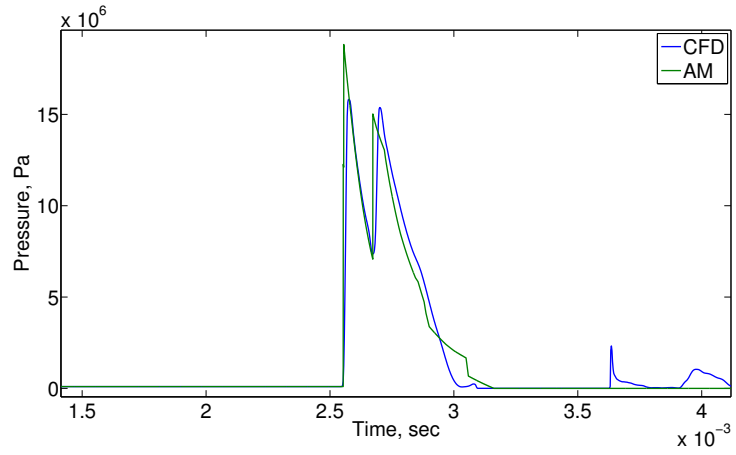

Figure B.3: Five 1 lb Charge Line Array Centerline Pressure History, 77 cm Charge Spacing, 400 cm Standoff

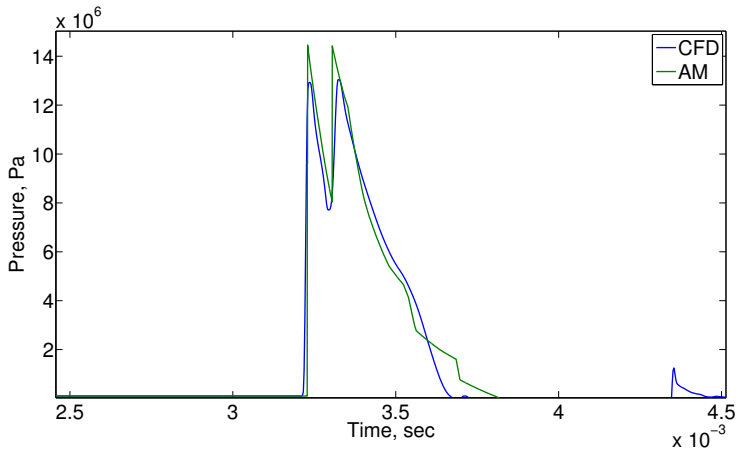

Figure B.4: Five 1 lb Charge Line Array Centerline Pressure History, 77 cm Charge Spacing, 500 cm Standoff

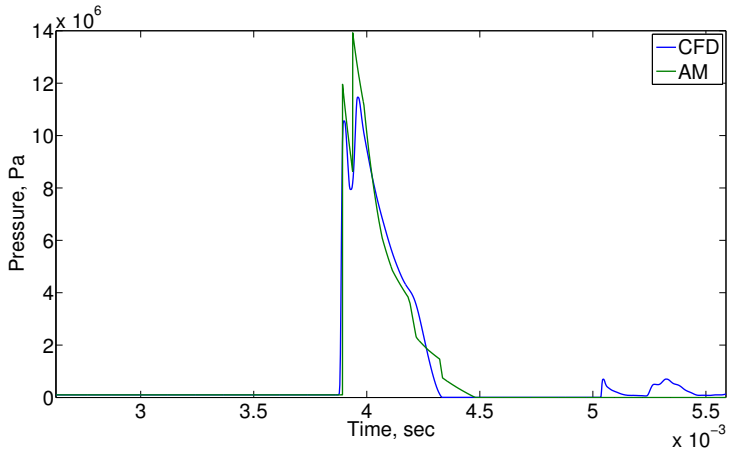

Figure B.5: Five 1 lb Charge Line Array Centerline Pressure History, 77 cm Charge Spacing, 600 cm Standoff

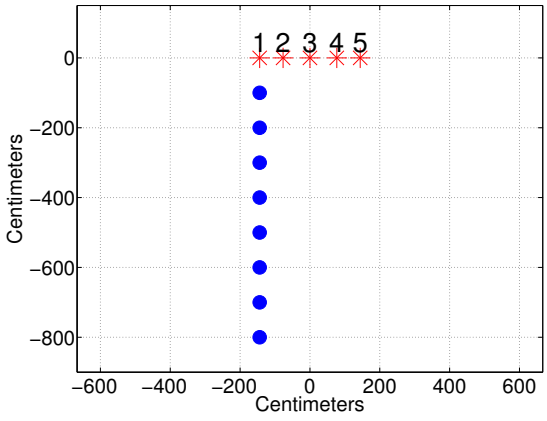

Figure B.6: Five 1 lb Charge Line Array Setup, Edge Standoffs

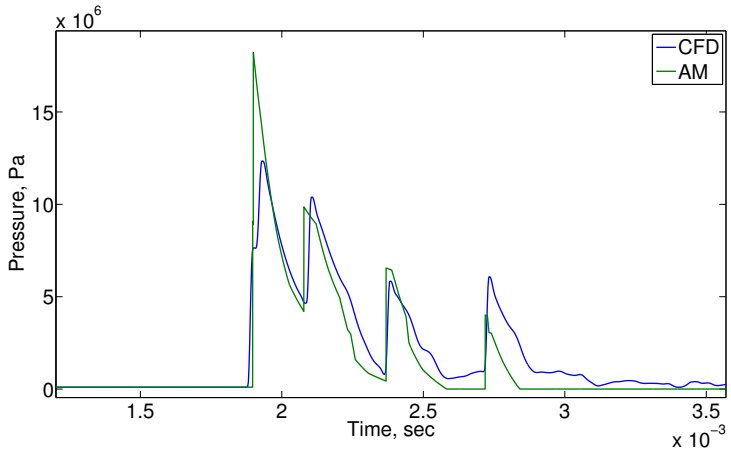

Figure B.7: Five 1 lb Charge Line Array Pressure History, 77 cm Charge Spacing, 300 cm Edge Standoff

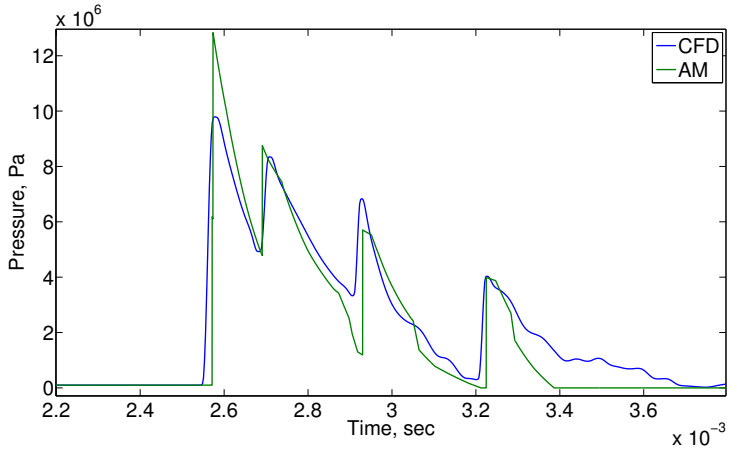

Figure B.8: Five 1 lb Charge Line Array Pressure History, 77 cm Charge Spacing, 400 cm Edge Standoff

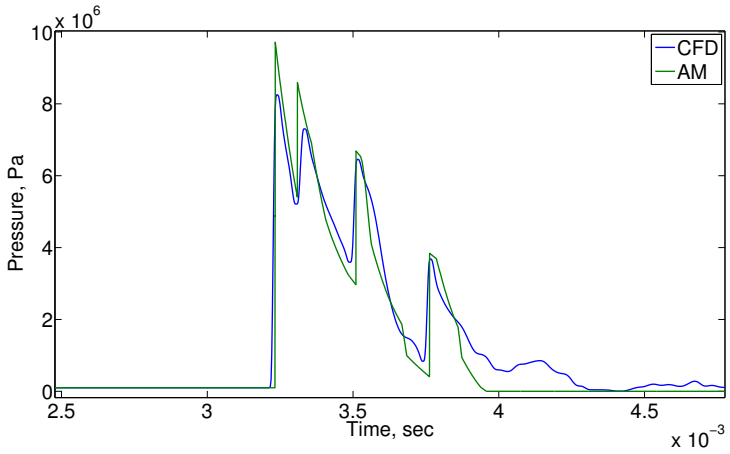

Figure B.9: Five 1 lb Charge Line Array Pressure History, 77 cm Charge Spacing, 500 cm Edge Standoff

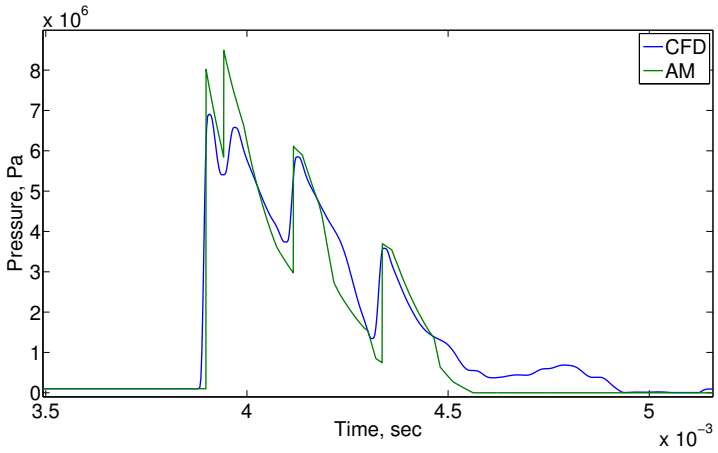

Figure B.10: Five 1 lb Charge Line Array Pressure History, 77 cm Charge Spacing, 600 cm Edge Standoff

BIBLIOGRAPHY

BIBLIOGRAPHY

Arons, A. B. (1953), Underwater explosion shock wave parameters at large distances from the charge, *J. Acoust. Soc. Am.*, *26*(3), 343–346.

Beyer, H. G., B. Lange, and H.-P. Waldl (1996), Modelling tools for wind farm upgrading, in *Proceedings of the European Union Wind Energy Conference EUWEC, Göteburg, Sweden*, pp. 1069–1073.

Bhatia, A. K., and S. K. Basu (2003), Tackling 0/1 knapsack problem with gene induction, *Soft Computing*, *8*(1), 1–9.

Blackstock, D. T. (1966), Connection between the fay and fubini solutions for plane sound waves of finite amplitude, *J. Acoust. Soc. Am.*, *39*(6), 1019–1026.

Bremner, G. F., J. K. Dukowicz, and I. I. Glass (1960), On the one-dimensional overtaking of a rarefaction wave by a shock wave, *Tech. Rep. Technical Note No. 33*, University of Toronto Institute of Aerophysics.

Chen, T. J., and C. Cooke (1994), On the riemann problem for liquid or gas-liquid media, *International Journal for Numerical Methods in Fluids*, *18*, 529–541.

Chipperfield, A., and P. Fleming (1995), The matlab genetic algorithm toolbox, in *Applied Control Techniques Using MATLAB, IEE Colloquium on*, pp. 10–1, IET.

Chowdhury, S., J. Zhang, A. Messac, and L. Castillo (2012), Unrestricted wind farm layout optimization (uwflo): Investigating key factors influencing the maximum power generation, *Renewable Energy*, *38*(1), 16 – 30.

Christian, E. A. (1973), The effects of underwater explosions on swimbladder fish, *Tech. Rep. NOLTR 73-103*, Naval Ordnance Laboratory, White Oak, Silver Spring, MD, USA.

Cole, R. H. (1948), *Underwater Explosions*, Princeton University Press, New Jersey, USA.

Coles, J. S., E. Christian, J. Slifko, C. Niffennegger, and M. Rogers (1946), Shock-wave parameters from spherical TNT charges detonated under water, *Underwater Explosion Research: Compendium of British and American Reports, 1950*, *I (The Shock Wave)*(5), 1085–1105.

Cooper, P. W. (1996), *Explosives Engineering*, VCH, New York, USA.

Courant, R., and K. O. Friedrichs (1948), *Supersonic Flow and Shock Waves*, Interscience Publishers, New York, USA.

Cudahy, E., and S. Parvin (2001), The effects of underwater blast on divers, *Tech. Rep. 82-488*, Naval Submarine Medical Research Laboratory, Groton, CT.

Folchi, R., and H. Wallin (2012), Deep water excavation with shaped charges: a case history in Lake Mead, Bolder City, Nevada, USA, in *Proceedings of the Thirty-Eight Annual Conference on Explosives and Blasting Technique*, pp. 23–30.

Haupt, R. L. (1995), An introduction to genetic algorithms for electromagnetics, *Antennas and Propagation Magazine, IEEE*, *37*(2), 7–15.

Haupt, R. L., and S. E. Haupt (2004), *The Binary Genetic Algorithm*, 27–50 pp., John Wiley and Sons, Inc.

Higashino, F., L. . F. Henderson, and F. Shimizu (1991), Experiments on the interaction of a pair of cylindrical weak blast waves in air, *Shock Waves*, *1*(1), 275–284.

Holl, R. (1982), Wellenfokussierung in fluiden, Ph.D. thesis, Technishen Hochschule Aachen.

Hunter, K. S., and T. L. Geers (2003), Pressure and velocity fields produced by an underwater explosion, *J. Acoust. Soc. Am.*, *115*(4), 1483–1496.

Kandula, M., and R. Freeman (2008), On the interaction and coalescence of spherical blast waves, *Shock Waves*, *18*(1), 21–33.

Lamb, H. (1923), The early stages of a submarine explosion, *Philosophical Magazine*, *45*(6), 257–265.

Landsberg, A., A. Dare, and A. Kee (2003), Three-dimensional modeling and simulation of weapons effects for obstacle clearance, in *Proceedings of the 2003 User Group Conference DoD_UGC-03*.

Liddiard, T., and J. W. Forbes (1983), Shockwaves in fresh water generated by the detonation of pentolite spheres, *Tech. Rep. 1218*, Naval Surface Weapons Center, Dahlgren, VA.

Malone, P. E. (2000), Surface ship shock modeling and simulation: extended investigation, Master's thesis, Naval Postgraduate School.

Medwin, H., and C. Clay (1997), *Fundamentals of Acoustical Oceanography*, Elsevier Science.

Moses, H. E. (1948), The Head-On Collision of a Shock Wave and a Rarefaction Wave in One Dimension, *Journal of Applied Physics*, *19*, 383–387.

Murata, K., K. Takahashi, and Y. Kato (1999), Precise measurements of underwater explosion phenomena by pressure sensor using fluoropolymer, *Journal of Materials Processing Technology*, *85*(13), 39 – 42.

Papalambros, P., and D. Wilde (2000), *Principles of Optimal Design: Modeling and Computation*, Cambridge University Press.

Penney, W. G. (1940), Pressure-time curves for underwater explosions, *Underwater Explosion Research*, *1*(1), 273–287.

Rice, M. H., and J. M. Walsh (1956), Equation of state of water to 250 kilo bars, *Journal of Chemical Physics*, *26*(4), 824–830.

Richardson, W., C. G. Jr., C. Malme, and D. Thompson (1995), *Marine mammals and noise*, Academic Press, San Diego, USA.

Rogers, P. H. (1977), Weak-shock solution for underwater explosive shock waves, *J. Acoust. Soc. Am*, *62*(6), 1412–1419.

Shin, Y. S. (2004), Ship shock modeling and simulation for far-field underwater explosion, *Computers and Structures*, *82*(2326), 2211 – 2219.

Singh, V. P., and M. S. Bola (1974), A note on explosive shock in homogeneous water, *Tech. rep.*, Terminal Ballistics Research Laboratory, Sector 30, Chandigarh.

Slifko, J. P., and T. E. Farley (1959), Underwater shockwave parameters for TNT, *Tech. Rep. NAVORD Report 6634*, U.S. Naval Ordnance Laboratory, White Oak, MD.

Smoller, J. (1983), *Shock Waves and Reaction-Diffusion Equations*, Springer-Verlag, New York, USA.

Sod, G. A. (1978), A survey of several finite difference methods for systems of nonlinear hyperbolic conservation laws, *Journal of Computational Physics*, *27*(1), 1–31.

Stowe, N. A., and N. Vlahopoulos (2012), On energy focusing with multiple sources in an inviscid field, *Shock Waves*, *22*(5), 451–463.

Swisdak, M. M. (1978), Explosion effects and properties: Part II: Explosion effects in water, *Tech. Rep. 76-116*, Naval Surface Warfare Center Report.

Thomas, T. Y. (1957), On the propagation and decay of spherical blast waves, *Journal of Mathematics and Mechanics*, *6*(5), 607–619.

Vernon, T. A. (1986), Whipping response of ship hulls from underwater explosion bubble loading, *Tech. Rep. Technical Memorandum 85/225*, National Defense, Research and Development Branch, Canada.

Wardlaw, A., W. Fourney, and U. Leiste (2010), Target loading from a submerged explosion, *Shock and Vibration*, *17*, 317–328.

Whitham, G. B. (1974), *Linear and Nonlinear Waves*, John Wiley and Sons, New York, USA.

Zong, Z., Y. Zhao, F. Ye, H. Li, and G. Chen (2012), Parallel computing of the underwater explosion cavitation effects on full-scale ship structures, *Journal of Marine Science and Application*, *11*(4), 469–477.